Development of Soft Actuation Systems for Use in Human-Centered Applications

Submitted in partial fulfillment of the requirements for

the degree of

Doctor of Philosophy

in

Mechanical Engineering

Jackson O. Wirekoh

B.S., Mechanical Engineering, Massachusetts Institute of Technology
M.S., Mechanical Engineering, Carnegie Mellon University

Carnegie Mellon University
Pittsburgh, PA

December, 2017

Dissertation Committee

Professor Yong-Lae Park, Chair, *Carnegie Mellon University*, *Seoul National University*

Professor Stelian Coros, *Carnegie Mellon University*, *Eidgenössische Technische Hochschule Zürich*

Professor Carmel Majidi, *Carnegie Mellon University*

Professor Cameron Riviere, *Carnegie Mellon University*

Acknowledgements

First, I would like to thank you Professor Park for giving me the opportunity to work alongside you as a member of the Soft Robotics and Bionics Lab at CMU. You have been pivotal in both my development as a researcher and an individual over the last few years. Thanks for your valuable insights, willingness to talk through tough topics, and overall cheerful disposition which helped to make my experience both rewarding and enjoyable.

Thank you to Professor's Coros, Majidi, and Riviere for joining my thesis committee and imparting upon me the wisdom each of you has gained throughout your years of experience working along the intersecting lines of academic and industrial research.

Thank you Hee-Sup, Celeste, Yiwei, Luis, Kevin, Tess, JB, Rick, Preston, Samson, Mitch, Edgar, Matt, Nitish, Nick, Sung-Hwan, and all the other members of the Soft Robotics and Bionics Lab for your support and friendship. You are all amazing, and I wish you all the best in your future endeavors!

Thank you Chris Hertz and Professor Higgs III, without whom I would not be where I am today. Thank you Ed, Jim, and John for your technical prowess, assistance, and overall hilarity during my machine shop visits. Thanks to the entire staff and members of the CMU Mechanical Engineering Department for their diligence and hard work to ensure that we are all on track to achieve our goals.

Thanks to Steven, Katie, Avinash, Stuart, Tom, Nathan, Luke, Vince, Justin, and all the friends I have made during my time at CMU. Thank you Bee, Thomas, ShanShan, Eddie, Matt, Ray, Cam, Tim, Minh, John, Jason, Ben, Jackie, Jordan, Michelle, Preethi, Veronica, Sam, John, Beatriz, Matt, Lili, Sheldon, Carrington, Yida, and the many friendships formed throughout my time at MIT. Thanks Robert, Devin, Abu, Mariya, Ransford, James, and John for being there for me since we were just school kids running around in the park. You all mean the world to me.

Special thanks to God and my family for their continued support and encouragement that has provided me the strength to reach my goals. Thank you Evans, Nana, Olivia and Elise, Sam, Ernest, Julie, William, Sampson, Eric, Moses, Preston, Mavis, Kjell, Tanja, Jerome, Joelle, Uncle Kwasi, Mom, and Dad. I am who I am because of you, and I thank you for being there for me through the good and the bad. I hope that I can make you proud.

Finally, thanks to my wonderful wife Chantal. You are my rock, and I could not have done any of this without your love, support, and amazing artistic skills. You inspire me to be the best that I can be. I love you so much and am blessed that you are part of my life.

Abstract

In recent years, soft materials have seen increased prevalence in the design of robotic systems and wearables capable of addressing the needs of individuals living with disabilities. In particular, pneumatic artificial muscles (PAMs) have readily been employed in place of electromagnetic actuators due to their ability to produce large forces and motions, while still remaining lightweight, compact, and flexible. Due to the inherent nonlinearity of PAMs however, additional external or embedded sensors must be utilized in order to effectively control the overall system. In the case of external sensors, the bulkiness of the overall system is increased, which places limits on the system's design. Meanwhile, the traditional cylindrical form factor of PAMs limits their ability to remain compact and results in overly complex fabrication processes when embedded fibers and/or sensing elements are required to provide efficient actuation and control.

In order to overcome these limitations, this thesis proposed the design of flat pneumatic artificial muscles (FPAMs) capable of being fabricated using a simple layered manufacturing process, in which water-soluble masks were utilized to create collapsed air chambers. Furthermore, hyperelastic deformation models were developed to approximate the mechanical performance of the FPAMs and were verified through experimental characterization. The feasibility of these design techniques to meet the requirements of human centered applications, including the suppression of hand tremors and catheter ablation procedures, was explored and the potential for these soft actuation systems to act as solutions in other real world applications was demonstrated. We expect the design, fabrication, and modeling techniques developed in this thesis to aid in the development of future wearable devices and motivate new methods for researchers to employ soft pneumatic systems as solutions in human-centered applications.

Table of Contents

List of Tables

Table of Figures

1 Introduction

1.1 Motivation

The United States is home to over 37 million people with reported cases of disabilities [1]. Of this population over 7 million suffer from amputation, with countless others suffering from neuromuscular disabilities caused by various conditions including stroke, heart disease, illness, or physical accidents [1, 2]. In response to these statistics, researchers have dedicated a great deal of effort towards the design of assistive wearable devices, such as prosthetics and exoskeletons, to improve the livelihoods of those who suffer from these ailments [3, 4]. In most cases these systems rely on rigid architectures, and include passive assistive devices, as well as active devices that are mechanically actuated by electromagnetic motors. However, there are many issues with wearable devices designed in this manner. Firstly, these rigid designs are inherently dangerous due to having a higher stiffness than that of organic tissue. Oftentimes, situations arise in which the rigid system inadvertently collides with the user's body, resulting in various degrees of physical damage. Secondly, in order to increase the functionality of these devices, additional electromechanical actuators must be introduced, increasing the overall size and weight of the system. Furthermore, the additional bulkiness and weight of the developed systems, especially in cases where electromagnetic motors are employed with gear trains, limit the maneuverability of the user and cause severe discomfort over extend use.

Fortunately, the advent of soft matter technologies and soft robotic solutions has begun to change the technological landscape. Utilization of soft polymers and the discovery of non-toxic conductive fluids [5, 6], has led to the creation of lightweight, flexible, and compliant actuators and sensors which can be integrated into human scale wearable devices, both large and small,

improving functionality without over taxing the user. These technologies include, conductive polymeric sensors [7], dielectric elastomer actuators (DEA) [8, 9] and shape memory alloys (SMA) [10, 11] which operate using electricity and heat respectively. In addition to these devices, pneumatic artificial muscles (PAM) [12, 13, 14] and conductive microfluidic sensors [15, 16, 17, 18] serve as a key component of the soft robotics toolkit.

PAMs specifically standout amongst this group of soft actuators due to their ability to produce human scale forces and displacements through the simple application of pressure gradients to induce inflation or deflation [12, 13, 14]. In addition, PAMs can be employed in a multitude of applications due to their operational versatility. Researchers and designers can combine soft polymeric substrates and flexible yet inextensible materials in different configurations to induce bending, twisting, extension, contraction, fortification, or any combination of these actions [12, 19, 20, 21]. These properties make PAMs a favorable alternative to the traditional electromechanical devices, and a particularly interesting platform on which to experiment. Thus this thesis focuses on addressing the aforementioned challenges researchers face in the development of effective designs for wearable devices. Specifically, soft pneumatic and hydraulic actuation systems, both with and without microfluidic sensing, were developed to address existing limitations.

1.2 Scope: Developing Novel Soft Pneumatic Actuation Systems

PAMs are powerful, lightweight, and compliant devices capable of generating a variety of forces, torques, and motions. However, these soft actuation systems exhibit nonlinear behavior due to their incorporation of hyperelastic polymers, such as thermoplastic elastomer gels (TPEGs), polydimethylsiloxane (PDMS), or silicone rubber. This nonlinearity not only makes it difficult to

develop accurate theoretical models to predict their performance, but also complicates the deployment of these actuators in real world systems. In order to overcome these issues, researchers have employed both external and internal sensors [7, 22, 23, 24, 25] to improve the controllability of these devices. However, in the case of external sensors, the overall bulkiness of the system must be increased, which limits the specific designs that can be employed. On the other hand, fabrication of PAMs with embedded sensing becomes particularly tricky. Due to the cylindrical form factor of traditional PAMs [12, 13, 26], as well as the more complex shapes of pleated PAMs [27] and polylobe PAMs [14], embedded sensors can be very difficult to incorporate in a straightforward fabrication process. Furthermore, manufacturing processes become increasingly more complex when multimodal sensing is desired. In addition, because traditional actuators have a cylindrical form factor, their radii while at rest must increase in order to able to generate larger forces or moments. This ensures that the actuators become increasingly less compact, which prevents the design of streamlined wearable devices [28, 29]. In order to address these limitations, we sought to develop and characterize a novel PAM design capable of being fabricated through a simple manufacturing process.

1.2.1 Design and Fabrication

In order to be able to produce a robust wearable device that is lightweight, compact, and capable of providing users with significant functionality without limiting maneuverability, a powerful compact soft actuation system with integrated sensing had to be designed. Thus, development of a thin, compact, multifunctional design for a novel PAM, which can be fabricated in a simple manufacturing process was the key tenet of this thesis. Existing PAM designs and their fabrication methods, including McKibben type actuators [12, 13, 26] , fiber embedded PAMs [22, 30], pleated PAMs [27], polylobe PAMs [14], and collapsed pneumatic actuators were [31]

examined. Ultimately, we settled on the design of the novel PAMs by combining and improving upon techniques associated with the design of fiber embedded PAMs, chosen due to their lower hysteresis when compared to McKibben Muscle type PAMs and their ability to be fabricated through molding [14], as well as pneumatic actuators fabricated with collapsed air chambers, due to their ability to remain very thin and compact in their rest states.

The PAM created by innovating upon these design techniques was a thin 2-Dimensional rectangular actuator with embedded fibers. We called this novel actuator a flat pneumatic artificial muscle (FPAM). The flat rectangular form factor allowed the actuator to be fabricated using a simple layered fabrication process. In addition, we introduced the use of a water-soluble mask to the fabrication process to allow for the creation of the collapsed air volume. This mask acts as a superior alternative to the mold release that is typically used in today's pneumatic actuators created with collapsed air chambers, by allowing the core of the actuator to be fabricated from a single cure, as opposed to having two thin procured layers bonded together. This capability significantly reduces the chances of unexpected delamination failures at low pressure inputs. Additionally, the mask can be quickly laser-cut to allow for a variety of interesting air volume designs and shapes. The properties of the fabrication process for this initial FPAM, coupled with its flat form factor, allowed the design to be easily scaled up or down. Furthermore, through the introduction of laser-cut plastic sheets in addition to, or as substitutions for the embedded fibers, multi-unit series FPAMs, sensorized FPAMs fabricated with embedded multimodal sensing, and fiber-reinforced bending FPAMs were able to be designed and fabricated. With the establishment of these novel designs, which will be described in greater detail I later sections, we needed to establish a means of predicting their performance in order to provide researchers and designs with flexibility in the creation of future actuation systems.

1.2.2 Hyperelastic Modeling and Validation

Theoretical models for the deformation of the FPAMs developed in this thesis have not previously been presented due to the novelty of the actuator's form factor. Thus we set out to develop accurate models capable of allowing researchers to approximate the performance of potential designs for desired use. Due to the rectangular form factor of the FPAM, we began by examining formulations developed for the large deformation of plates [32, 33, 34]. Initially, these formulations were solved for the desired boundary conditions through the minimization of the system's potential energy, assuming elastic behavior of the actuators. Subsequently, we utilized these solutions as a basis to introduce hyperelastic deformation terms. Analytical hyperelastic deformation models were then able to be developed for these developed PAMs. Furthermore, experimental characterization of the mechanical performance of the PAMs was conducted in order to validate the accuracy of the developed models. Various experimental setups were developed to measure the static, dynamic, and electrical performance of the developed actuators. The developed analytical models compared favorably with the experimental results, which can be seen in later sections.

1.2.3 Application and Inspiration

The initial FPAM developed was designed to fit seamlessly into a wearable device, such as an orthotic or prosthetic, in order to provide the user with a lightweight but powerful means of rehabilitation and/or assistance. Subsequently, the FPAM was modified to incorporate embedded sensors. In this manner, a bioinspired sensorized FPAM (sFPAM) was created with the capability to detect its own contraction length and force generation without external sensors. This behavior is similar to the manner in which human muscle employs muscle spindles and Golgi Tendon organs to detect its own stretch and force. Ultimately this design would allow the sFPAM to be employed

as a self-contained sensor-actuator system for controlled operation to a desired set point without the need for external sensors, which would greatly reduce the overall form factor of a wearable device.

The techniques and skills learned throughout the initial FPAM and sensorized FPAM research, were then applied to human centered applications including the suppression of hand tremors and the improvement of the efficacy of cardiac ablation treatments. Initially, the analytic hyperelastic model was adapted for the creation of a fiber-reinforced bending FPAM to be used in the treatment of hand tremors. This FPAM was designed with a series of geometric constraints in order to ensure controlled repeatable bending. The fiber-reinforced bending FPAM was experimentally characterized and demonstrated the feasibility to suppress hand tremors associated with Parkinson's disease and essential tremor. Lastly, a more traditional FPAM, in the sense of employing a cylindrical form factor, was designed as a solution to issues faced in cardiac ablation. A fiber-reinforced thick-walled PAM was designed and fabricated to provide required forces and displacements for successful the successful treatment of tachycardia, such as atrial fibrillation, inside the body at the site of treatment. Due to the use of soft materials, a miniaturized functional catheter tip was designed to be able to fit in the millimeter sized catheter sheets used for minimally invasive surgeries, while being able to provide linear actuation and unidirectional force sensing through the use of an embedded microfluidic sensor. These applications, which will be further detailed, demonstrate the feasibility of the developed PAMs to be readily applied to real word human-centered applications.

1.3 Thesis Outline

The remainder of this thesis is organized as follows: Firstly, the initial design of the FPAM is detailed in Chapter 2: Flat Pneumatic Artificial Muscles, Chapter 3: Biologically Inspired

Sensorized Flat Pneumatic Artificial Muscles details the development of the bioinspired sensorized FPAM design, followed by a description of the fiber-reinforced bending FPAM in Chapter 4: Fiber-reinforced FPAM for the Suppression of Hand Tremors, then Chapter 5: Soft Miniaturized Actuation and Sensing Unit for Cardiac Ablation Procedures provides details regarding work completed on the functional catheter tip, and finally Chapter 6: Conclusion summarizes the results and implications of this thesis.

2 Flat Pneumatic Artificial Muscles

Abstract

Pneumatic artificial muscles (PAMs) have gained wide use in the field of robotics due to their ability to generate linear forces and motions with a simple mechanism, while remaining lightweight and compact. However, PAMs are limited by their traditional cylindrical form factors, which must increase radially to improve contraction force generation. Additionally, this form factor results in overly complicated fabrication processes when embedded fibers and sensor elements are required to provide efficient actuation and control of the PAMs while minimizing the bulkiness of the overall robotic system. In order to overcome these limitations, a flat two-dimensional PAM capable of being fabricated using a simple layered manufacturing process was created. Furthermore, a theoretical model was developed using the von Karman formulation for large deformations and the energy method. Experimental characterizations of two different types of PAMs, a single-cell unit and a multi-cell unit, were performed to measure the maximum contraction lengths and forces at input pressures ranging from 0 to 150 kPa. Experimental data were then used to verify the fidelity of the theoretical model.

Keywords: pneumatic artificial muscle (PAM), actuators, soft robotics, design and manufacturing, embedded fibers, strain-stress test

2.1 Introduction

Pneumatic artificial muscles (PAMs) have been widely used in the field of robotics, especially for soft robotic applications, due to their ability to produce linear forces and displacements with a simple mechanism [12, 13, 14]. In most cases, these actuators are composed of elastomeric cylindrical bladders geometrically constrained by flexible yet inextensible

mechanisms such, as meshes [12, 13, 26], nets [35], and embedded fibers [22, 30]. These systems work in unison producing compact, lightweight, and compliant actuators capable of high force generation to weight ratios [12, 13, 14]. In addition, due to the use of compressed air for actuation, soft robotic systems with PAMs have almost no danger when compared with ones that use combustion or fire as a power source [36, 37]. These qualities have made PAMs a growing topic of interest among researchers and industry alike.

Modern research into the design and utilization of PAMs began with a McKibben-type actuator, which was first proposed by atomic physicist Joseph Laws McKibben in the late 1950's [12]. The McKibben actuator, which makes use of a braided mesh and a cylindrical bladder to provide linear force and contraction when stimulated with pressurized air, was originally designed for use in an orthotic device to aid polio patients [12, 14, 27]. In later years, as pneumatic technology improved, companies such as Bridgestone Co. and Festo AG, modified and commercialized the McKibben design for use in robotic systems [12, 14, 27]. The success of the McKibben-type actuators resulted in further innovation and implementation of PAMs.

One such innovation was the Baldwin-type actuator first proposed in 1969, which later served as inspiration to actuators developed by Park et al. [22]. This PAM design was composed of a thin cylindrical substrate with embedded glass filaments (fibers) that generally resulted in mechanical performances with reduced hysteresis when compared to that of McKibben-type actuators [14]. However, radial expansion limited the maximum input pressures to 100 kPa [14]. Another notable design, conceptualized and produced by Daerden and Lefeber in 2001, was the pleated pneumatic artificial muscle (PPAM) [27]. This design was created as a more robust PAM capable of addressing the energy loss and hysteresis typically found in McKibben-type actuators. The PPAM is composed of a high-tensile-modulus cylindrical membrane that is folded in on itself

9

(pleated) like the bellows of an accordion [27]. During operation, instead of wasting energy to radially deform, the PPAM's membrane simply unfurls, allowing the actuator to bulge out radially but shorten axially.

In addition to the aforementioned PAMs, polylobe and prolated designs, such as Robotic Muscle Actuators (ROMACs) [14] and Yarlett-type actuators [14], respectively, have been created to produce linear motions. However, these actuators are uncommon in real world applications due to their complex designs. The McKibben-type actuator, Baldwin actuator, and PPAM, on the other hand, have traditionally seen wider use in both research and industry. However, their effectiveness, particularly relating to their use in wearable devices, is limited by their cylindrical form factors, as shown in a soft ankle orthotic device that used McKibben-type PAMs for actuation [38]. More specifically, due to the scaling of force generation with the radius of traditional PAMs, actuators become increasingly less compact when larger forces are desired. This prevents the design of streamlined wearable devices, which may limit the range of motion of the wearer.

Moreover, the nonlinear response of PAMs to input stimulation (i.e. air pressure) is a critical issue that must be addressed by designers during controlled device operation. In order to ensure effective real-time control of the actuators, while preserving the compactness and compliance of the system, researchers have attempted to integrate sensors directly in the PAMs during fabrication either by embedding conductive elements in the elastomeric air chamber for resistive sensing [7, 22, 23] or by adding braided conductive wires to the outer mesh structure for inductive sensing [24, 25]. However, due to the cylindrical form factor of the PAMs, the fabrication process becomes overly complicated. This complexity increases the difficulty of embedding multiple sensor elements for multi-modal detection (e.g. position and force), which are necessary to effectively control the system.

In order to address the shortcomings of traditional cylindrical PAMs, a two-dimensional (2D) flat pneumatic artificial muscle (FPAM) was proposed. This study focuses on the design and theoretical modeling of the FPAMs. Furthermore, the proposed flat muscle design was realized through a simple layered fabrication method, and the theoretical model was experimentally verified.
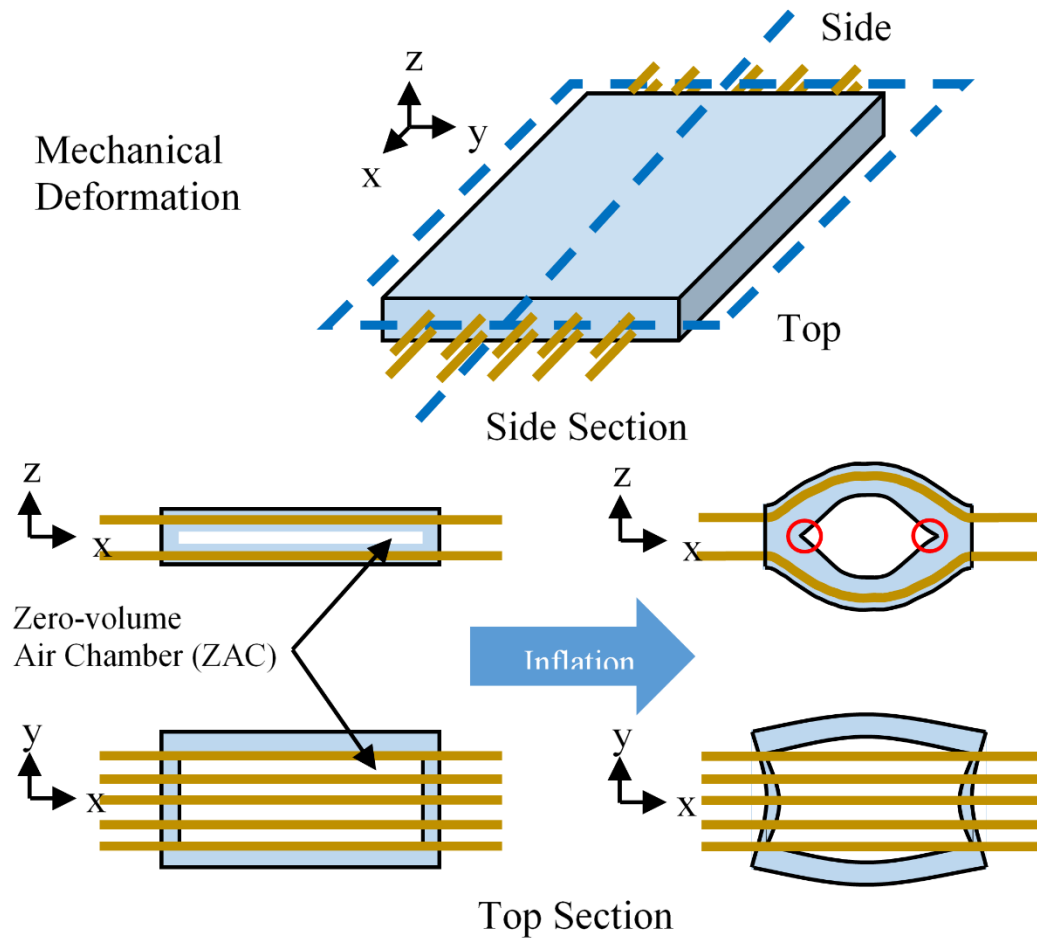
Figure 2.1: Illustration of actuator at rest and sectional views of actuator at rest (**left**) and inflated (**right**). Kevlar fibers are shown in dark orange. Red circles indicate high stress concentrations.

2.2 Design and Fabrication

A 2D FPAM, shown in Figures 2.1 and 2.2, was designed to remain compact and easily predisposed to the addition of multiple embedded sensor layers, which is very difficult to achieve

when employing the cylindrical shape of traditional PAMs. This unusual form factor allows for the introduction of a concept described as the "zero-volume air chamber" or ZAC [31], which manifests itself as a very thin ($\leq$ 0.1 mm) rectangular air volume encased by two flat elastomeric sheets. This design effectively reduces the overall thickness of the actuator by removing the necessity of having a designated air void in the center of the relaxed actuator as seen in typical PAMs. Furthermore, the flat configuration of the actuator makes it possible to easily resize and reconfigure each individual muscle array [31], which can be seen in Figure 2.2. These features of the proposed 2D form factor will make it particularly easy to hide and/or incorporate the flat muscle into clothing-like wearable devices. In these applications, the 2D form factor becomes increasingly more important, particularly when larger forces are required despite the need to maintain the compactness of the system. Whereas for traditional cylindrical PAMs, in which the radius must be increased to generate larger forces (volumetric increase), the FPAM must only be designed with a wider air volume (area increase), which is tantamount to adding actuators in parallel. Therefore, in situations in which covering a wider surface area is allowable, the FPAM offers minimal volumetric change while providing desired forces. These features will ultimately allow for wearables that look like elastic suits which are capable of naturally deforming with the human body while providing active assistance to body motions.

The FPAM proposed in this study is made of a silicone substrate that contains embedded Kevlar fibers. The stretchability of the substrate and the flexible yet inextensible nature of the fibers work in unison to produce axial contraction when the FPAM is pressurized and radially inflated, as shown in Figure 2.1. However, the inflated actuator is subject to high stress concentrations along the sides of the bladder, which previously resulted in a prominent

delamination failure mode along the edges [31]. To overcome this issue, a new fabrication process was proposed.
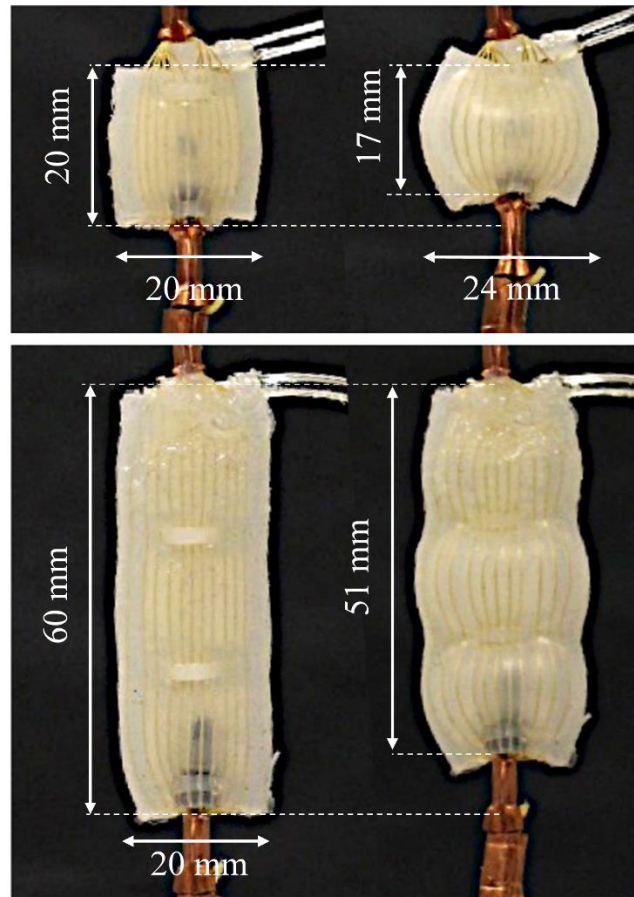
Figure 2.2: Prototypes of single cell unit at rest and contracted (**top**) and multi-cell unit (3 × 1 series) at rest and contracted (**bottom**). Prototypes experienced maximum thickness (out of plane) changes of 8 mm during contraction.

Illustrated in Figures 2.3 and 2.4, the fabrication process makes use of uncured liquid silicone (Dragon Skin10, Smooth-On) and 3D printed molds to create two thin silicone sheets and a core (central substrate containing the ZAC) with an embedded water-soluble mask made of a water-soluble fabric stabilizer (Paper Solvy, Sulky). After curing, the silicone layers are stacked and adhered together to form the base actuator in the following order: bottom layer, aligned Kevlar fibers, core, aligned Kevlar fibers, and top layer. Finally, the mask is removed by water and tube fittings and securements for the Kevlar fibers are added to complete the actuator. Prototypes of the

single cell unit (SCU) as well as a 3×1 multi-cell unit (MCU) are shown in Figure 2.2. The SCU is 20 mm $\times$ 20 mm $\times$ 4 mm thick, while the MCU is 60 mm $\times$ 20 mm $\times$ 4 mm thick. Both actuators have ZAC dimensions of 14 mm $\times$ 14mm $\times$ 0.1mm thick.
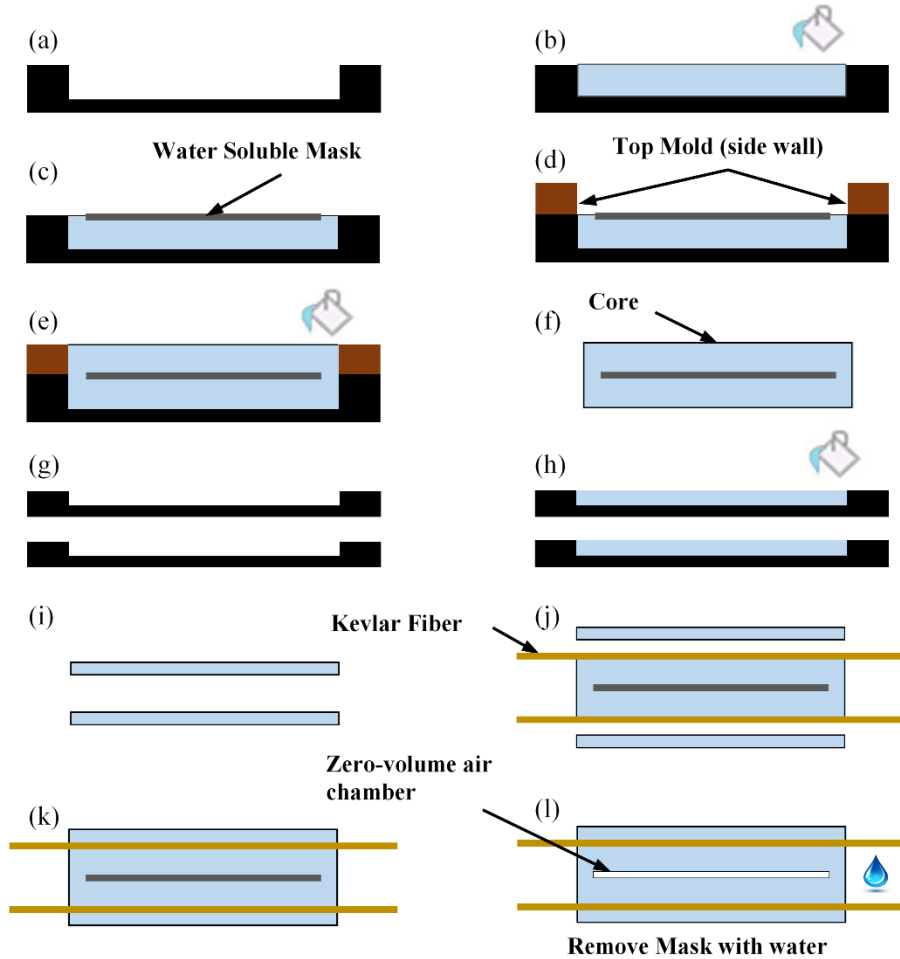
Figure 2.3: Fabrication process of FPAM using water-soluble mask: (**a**) prepare bottom core mold, (**b**) pour liquid elastomer for bottom half of core, (**c**) place water-soluble mask, (**d**) place top mold, (**e**) pour liquid elastomer for top half of core, (**f**) remove core after curing, (**g**) prepare thin layer molds, (**h**) pour liquid elastomer to create thin outer layers, (**i**) remove thin outer layers after curing, (**j**) align Kevlar, outer layers, and core, (**k**) bond using liquid elastomer, and (**l**) remove mask using water.
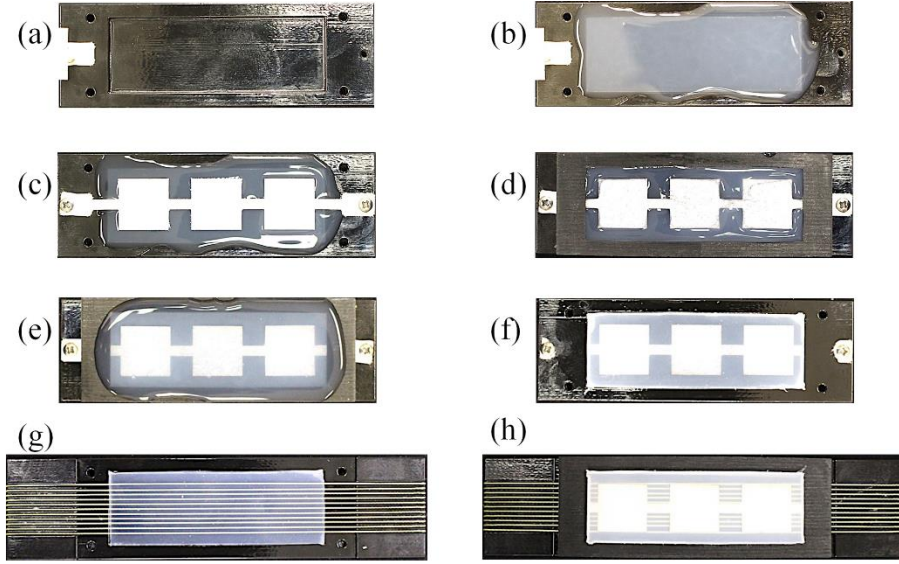
Figure 2.4: Photos of actual fabrication steps for 3 x 1 multi-cell FPAM: (**a**) bottom core mold (Figure 2.3-a), (**b**) liquid silicone in bottom core mold (Figure2. 3-b), (**c**) water-soluble mask on liquid silicone (Figure 2.3-c), (**d**) top mold added (Figure 2.3-d), (**e**) liquid silicone on mask (Figure 2.3-e), (**f**) cured core (Figure 2.3-f), (**g**) Kevlar fibers on cured bottom outer layer (Figures 2.3-i and 2.3-j), and (**h**) core bonded to Kevlar fibers and bottom outer layer (Figures 2.3-j and 2.3-k). (**g**) and (**h**) are repeated to complete prototype with top outer layer and Kevlar fibers.

2.3 Elastic Large Deformation Model

A theoretical model was developed to approximate the properties of the proposed FPAM by assuming the actuator is composed of two flat rectangular composite sheets that are simply supported along the edges. Through this convention, modeling techniques for the large deformation of membranes (thickness small in comparison to length and width) [32, 33, 34] could be utilized.
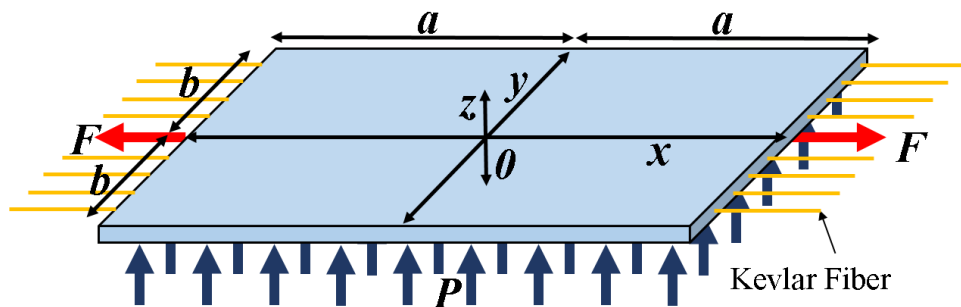
Figure 2.5: Approximation of top half of actuator as flat sheet under external force F and pressure P.

Figure 2.5 depicts the top half of the actuator with dimensions of $2a$ and $2b$, which are equal to the length and width of the air volume respectively. The membranes are subjected to an axial force F (required force to counteract contractive force of FPAM) in the x-coordinate direction at the loaded edges $x = \pm a$ and a uniformly applied lateral pressure P in the z-coordinate direction. In addition, the following assumptions are made regarding the deformation of the membranes:

1. Stress in the z-axis direction is considered negligible in comparison to x- and y- axes $[\sigma_x, \sigma_y$ only],

2. The normal to midplane is normal after deformation $[\gamma_{xy}$ only],

3. Deformation occurs in elastic range [Hooke's Law],

4. Bending strains are negligible in elastic range,

5. There is no delamination between fibers and elastic substrate, and

6. z-axis deflection is $w(x, y) = w_0 \cos\frac{\pi x}{2a} \cos\frac{\pi y}{2b}$ as postulated by Timoshenko [32, 33]

These assumptions were then applied to Von Karman's formulation for large deformations, provided in Equations (2.1) and (2.2) as follows:

$$\nabla^4 \phi = E \left[\left(\frac{\delta^2 w}{\delta x \delta y} \right)^2 - \frac{\delta^2 w}{\delta x^2} \frac{\delta^2 w}{\delta y^2} \right], \tag{2.1}$$

$$\nabla^4 w = \frac{h}{D} \left[\frac{P}{h} + \frac{\delta^2 \phi}{\delta y^2} \frac{\delta^2 w}{\delta x^2} + \frac{\delta^2 \phi}{\delta x^2} \frac{\delta^2 w}{\delta y} - 2 \frac{\delta^2 \phi}{\delta x \delta y} \frac{\delta^2 w}{\delta x \delta y} \right], \tag{2.2}$$

where $\nabla^4 = \frac{\delta^4}{\delta x^4} + 2 \frac{\delta^4}{\delta x^2 \delta y^2} + \frac{\delta^4}{\delta y^4}$, h is the thickness of the membrane, E is the Young's modulus, D is the structural rigidity, and Φ is the stress function defined by:

$$\sigma_x = \frac{\delta^2 \phi}{\delta y^2}, \tag{2.3a}$$

$$\sigma_y = \frac{\delta^2 \phi}{\delta x^2}, \tag{2.3b}$$

$$\tau_{xy} = -\frac{\delta^2 \phi}{\delta x \delta y}. \tag{2.3c}$$

Due to the difficulty in analytically solving Equation (2.2), application of the energy methods [17–19], which will be detailed later, was used to solve for the unknown quantity w_0. Once solved, these formulations determined solutions for the x-axis and y-axis displacements $u(x,y)$ and $v(x,y)$. However, due to the nature of the membrane as an anisotropic composite, the directional dependence of the material properties had to be incorporated into the formulations. This is achieved through a reformulation of Equation (2.1). Initially, the stress-strain relationship of the membrane was examined using Hooke's Law. This elastic (linear) relationship further simplifies these complex equations, while providing a powerful means for the development of solutions in both the plastic and hyperelastic (nonlinear) regime of deformations through the use of Ilyushin's iterative elastic solutions method [19], which is further expanded later in this section. Through this formulation, with the applied assumptions, the stress-strain relationships were defined as the following:

$$\varepsilon_x = \frac{1}{E_x}(\sigma_x - v_{xy}\sigma_y), \tag{2.4a}$$

$$\varepsilon_y = \frac{1}{E_y}(\sigma_y - v_{yx}\sigma_x), \tag{2.4b}$$

$$\gamma_{xy} = \frac{1}{G_{xy}}\tau_{xy}, \tag{2.4c}$$

where ε_x, ε_y, and γ_{xy} are the normal strains and the shear strain, respectively, σ_x, σ_y, and τ_{xy} are the normal stresses and the shear stress, respectively, E_x and E_y are the elastic moduli in the x- and y-axis directions, respectively, G_{xy} is the shear modulus, v_{xy} is the Poisson's ratio representing the

effects of y-axis stress on the x-axis deformation, and v_{yx} is the Poisson's ratio representing the effects of x-axis stress on the y-axis deformation. Approximations for the aforementioned material properties were defined by [39, 40] through the use of iso-stress and iso-strain formulations for the characterization of fiber-reinforced composites. The resulting formulations are:

$$E_x = V_f E_f + V_s E_s , \tag{2.5a}$$

$$E_y = \frac{E_f E_s}{V_s E_f + v_f E_s} , \tag{2.5b}$$

$$G_{xy} = \frac{G_f G_s}{V_s G_f + V_f G_s} , \tag{2.5c}$$

$$v_{xy} = V_f v_f + V_s v_s , \tag{2.5d}$$

$$v_{yx} = v_{xy} \frac{E_y}{E_x} , \tag{2.5e}$$

where V_f, E_f, G_f, and v_f are the volumetric fraction, elastic modulus, shear modulus, and Poisson's ratio of the embedded fibers, respectively, and V_s, E_s, G_s, and v_s represent the same quantities for the elastic substrate. It is important to note that these approximations represent upper or lower bounds and should be experimentally verified when possible by [39, 40].

In addition to knowledge of Equations (2.4a) – (2.4c) and Equations (2.5a) – (2.5e), formulation of the strain-displacement relationship must be established. Through examination of the elongation of a small element of the displaced membrane, as seen in Figure 2.6 (top) , the strain of the system in the x direction, and similarly in the y direction, due to lateral loads can be defined. Furthermore, by taking two linear elements as seen in Figure 2.6(bottom), the shear strain can additionally be defined as follows:

$$\epsilon_x = \frac{\delta u}{\delta x} + \frac{1}{2}\left(\frac{\delta w}{\delta x}\right)^2 , \tag{2.6a}$$

$$\epsilon_y = \frac{\delta v}{\delta y} + \frac{1}{2}\left(\frac{\delta w}{\delta y}\right)^2, \tag{2.6b}$$

$$\gamma_{xy} = \frac{\delta u}{\delta y} + \frac{\delta v}{\delta x} + \frac{\delta w}{\delta x}\frac{\delta w}{\delta y}. \tag{2.6c}$$

Equations (2.6a) – (2.6c) can then be used to define the compatibility condition:
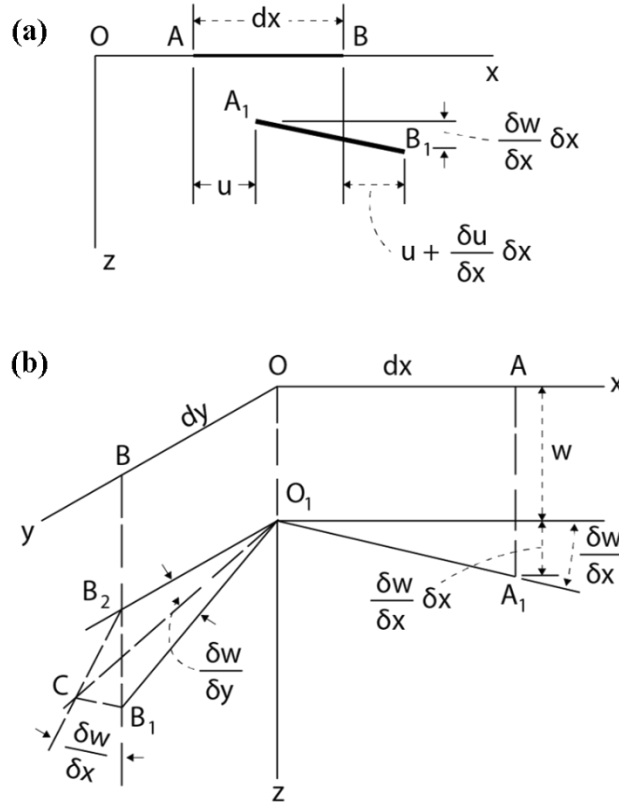
Figure 2.6: Depiction of axial strain ϵ_x due to displacement (**a**) and depiction of shear strain γ_{xy} due to displacement (**b**) (recreated from Timoshenko et al [32]).

$$\frac{\delta^2\epsilon_x}{\delta y^2} + \frac{\delta^2\epsilon_y}{\delta x^2} - \frac{\delta^2\gamma_{xy}}{\delta x\delta y} = \left(\frac{\delta^2 w}{\delta x\delta y}\right) - \frac{\delta^2 w}{\delta x^2}\frac{\delta^2 w}{\delta y^2}. \tag{2.7}$$

Substitution of Equations (3a) – (3c) and Equations (a) – (c) into Equation (5) then yields the reformulated Von Karman's Equation (1) for a fiber-reinforced composite material as:

$$\frac{1}{E_y}\frac{\delta^4\phi}{\delta x^4} + \frac{1}{E_x}\frac{\delta^4\phi}{\delta y^4} + \left(\frac{1}{G_{xy}} - \frac{\nu_{xy}}{E_x} - \frac{\nu_{yx}}{E_y}\right)\frac{\delta^4\phi}{\delta x^4} = \left[\left(\frac{\delta^2 w}{\delta x\delta y}\right)^2 - \frac{\delta^2 w}{\delta x^2}\frac{\delta^2 w}{\delta y^2}\right], \tag{2.8}$$

where the right-hand-side of the equation is:

$$\left[\left(\frac{\delta^2 w}{\delta x \delta y}\right)^2 - \frac{\delta^2 w}{\delta x^2}\frac{\delta^2 w}{\delta y^2}\right] = -\frac{\pi^4 w_0^2}{32a^2 b^2}\left[\cos\left(\frac{\pi x}{a}\right) + \cos\left(\frac{\pi y}{b}\right)\right] \tag{2.9}$$

With the establishment of Equation (2.8), the PDE can then be solved as a boundary value problem

in order to determine the stress function $\Phi(x,y)$. The boundary conditions, defined by the condition

of simply supported edges on rollers, were specified as the following:

1. $u(\pm a, y) = \pm\frac{1}{2}u_0$,

2. $v(x, \pm b) = \pm\frac{1}{2}v_0$,

3. $\tau_{xy}(\pm a, y) = 0$, and

4. $\tau_{yx}(x, \pm b) = 0$,

where u_0 and v_0 are the maximum displacements in the x and y directions, respectively. Due to the

constant boundary conditions of (1) and (2), as well as the relationship between the shear stress

and the derivatives $\frac{\delta u}{\delta y}$ and $\frac{\delta v}{\delta y}$ as seen in Equation (2.6c), the boundary conditions (3) and (4) result

in the following two equivalent conditions as specified in [32]:

5. $\frac{\delta v}{\delta x}(\pm a, y) = 0$,

6. $\frac{\delta u}{\delta y}(x, \pm b) = 0$.

In order to solve for the stress function $\Phi(x,y)$, particular and homogenous equations are solved

for by assuming the following forms:

$$\phi_p(x, y) = c_1 \cos\left(\frac{\pi x}{a}\right) + c_2 \cos\left(\frac{\pi y}{b}\right), \tag{2.10a}$$

$$\phi_h(x, y) = c_3 x^2 + c_4 y^2. \tag{2.10b}$$

The particular solution, $\Phi_p(x,y)$, is solved for by substitution of Equation (2.10a) into Equation

(2.8) and solving for the unknown coefficients c_1 and c_2. This yields:

$$c_1 = -\frac{E_y a^2 w_0^2}{32b^2} \qquad\qquad c_2 = -\frac{E_x b^2 w_0^2}{32a^2} \qquad\qquad (2.1\text{l})$$

The particular solution is then used to solve for the homogenous solution through the application

of the boundary conditions. Using Equations (2.4) – (2.6) and Equations (2.3a) – (2.3c). The

derivatives $\frac{\delta u}{\delta x}$ and $\frac{\delta v}{\delta y}$ can be expressed in terms of the stress function:

$$\frac{\delta u}{\delta x} = \frac{1}{Ex}\left(\frac{\delta^2 \phi}{\delta y^2} - v_{xy}\frac{\delta^2 \phi}{\delta x^2}\right) - \frac{1}{2}\left(\frac{\delta w}{\delta x}\right)^2, \qquad\qquad (2.12\text{a})$$

$$\frac{\delta v}{\delta y} = \frac{1}{Ey}\left(\frac{\delta^2 \phi}{\delta x^2} - v_{yx}\frac{\delta^2 \phi}{\delta y^2}\right) - \frac{1}{2}\left(\frac{\delta w}{\delta y}\right)^2. \qquad\qquad (2.12\text{b})$$

Integration of Equation (2.12a) and (2.12b), with respect to x and y, respectively, and subsequent

differentiation, with respect to y and x, respectively, allows for the application of the boundary

conditions. Additionally, through the use of the particular solution, the unknown coefficients c_3

and c_4 are solved as:

$$c_3 = \frac{-1}{64a^2 b^2 (v_{xy}v_{yx} - 1)}\left[E_y(\pi^2 a^2 w_0^2 + 16v_0 a^2 b)\right.$$

$$\left. + E_x v_{yx}(\pi^2 b^2 w_0^2 + 16u_0 ab^2)\right], \qquad\qquad (2.13)$$

$$c_4 = \frac{-1}{64a^2 b^2 (v_{xy}v_{yx} - 1)}\left[E_y v_{xy}(\pi^2 a^2 w_0^2 + 16v_0 a^2 b)\right.$$

$$\left. + E_x(\pi^2 b^2 w_0^2 + 16u_0 ab^2)\right].$$

The complete stress function can then be formulated as:

$$\phi_p(x,y) = -\left[\frac{E_y a^2 w_0^2}{32b^2}\cos\left(\frac{\pi x}{a}\right) + \frac{E_x b^2 w_0^2}{32a^2}\cos\left(\frac{\pi y}{b}\right) + \right. \qquad (2.14)$$

$$x^2\left(\frac{E_y(\pi^2 a^2 w_0^2 + 16v_0 a^2 b) + E_x v_{yx}(\pi^2 b^2 w_0^2 + 16u_0 ab^2)}{64a^2 b^2 (v_{xy}v_{yx} - 1)}\right) +$$

$$\left. y^2\left(\frac{E_y v_{xy}(\pi^2 a^2 w_0^2 + 16v_0 a^2 b) + E_x(\pi^2 b^2 w_0^2 + 16u_0 ab^2)}{64a^2 b^2 (v_{xy}v_{yx} - 1)}\right)\right].$$

The displacement functions $u(x,y)$ and $v(x,y)$ are then determined from the stress function as:

$$u(x,y) = \frac{u_0 x}{2a} + \frac{\pi w_0^2}{32a}\left[1 + \cos\left(\frac{\pi y}{b}\right) + \frac{v_{xy}E_y a^2}{E_x b^2}\right]\sin\left(\frac{\pi x}{a}\right), \tag{2.15}$$

$$v(x,y) = \frac{v_0 y}{2b} + \frac{\pi w_0^2}{32b}\left[1 + \cos\left(\frac{\pi x}{a}\right) + \frac{v_{yx}E_x b^2}{E_y a^2}\right]\sin\left(\frac{\pi y}{b}\right), \tag{2.16}$$

forming the complete formulation of the membrane deformation with displacement $w(x,y)$:

$$w(x,y) = w_0 \cos\frac{\pi x}{2a}\cos\frac{\pi y}{2b}. \tag{2.17}$$

With the establishment of the x-axis and y-axis displacements, the minimization of the mechanical potential energy within the membrane, also known as the energy methods [32, 33], is used to determine the overall deformation of the FPAM. The energy of the membrane is composed of three components. These components are the work done by the applied pressure W_P, the work done by the applied force at the edges of the membrane W_F, and the change in strain energy V of the membrane due to the application of this pressure. Taking into account that the actuator is composed of 2 flat sheets, the potential energy of the system can then be written as:

$$\Pi = 2\left[V - W_p - W_F\right]. \tag{2.18}$$

The strain energy of the system is defined as,

$$V = \frac{1}{2}\iiint \left[\sigma_x \epsilon_x + \sigma_y \epsilon_y + \tau_{xy}\gamma_{xy}\right]dxdydz, \tag{2.19}$$

where the stresses σ_x, σ_y, and τ_{xy} are calculated by substitution Equation (2.14) into Equations (2.3a) – (2.3c), the strains ε_x, ε_y, and γ_{xy} are calculated by substitution of Equations (2.15) – (2.17) into Equations (2.6a) – (2.6c), and the integration is taken over the dimensions of a single sheet. The work done by the pressure is defined as:

$$W_P = \iint [Pw(x,y)]dxdy \iint \left[P\, w_0 \cos\frac{\pi x}{2a}\cos\frac{\pi y}{2b}\right]dxdy, \tag{2.20}$$

where once again, integration is taken over the dimensions of a single sheet. Lastly, the work done

by the applied force at the loaded edges $x = \pm a$ is:

$$W_F = \iiint [\sigma_F \epsilon_x] dx dy dz = F \left[\frac{\pi^2 w_0^2}{32a} + \frac{F u_0}{2} \right] \tag{2.21}$$

where σ_F is the stress caused by the force F at the loaded edges.

Utilizing the energy components defined in (2.19) – (2.21) and Equation (2.18), the potential energy can then be minimized with respect to the unknowns w_0, u_0 and v_0 as follows.

$$\frac{\delta \Pi}{\delta u_0} = 0, \tag{2.22a}$$

$$\frac{\delta \Pi}{\delta v_0} = 0, \tag{2.22b}$$

$$\frac{\delta \Pi}{\delta w_0} = 0. \tag{2.22c}$$

Equations (2.22a) – (2.22c) could then be solved to define the input pressure P as a function of contraction u_0 and force generation F. However, an adjustment had to be made in order to reflect the real world deformation of the actuator. The energy method predicts contraction in both the x- and y-axis directions due to input pressure, establishing the following relationship when the actuator has reached equilibrium (zero force generation),

$$v_0 = \frac{a}{b} u_0. \tag{2.23}$$

However, in actuality the actuator expands in the y-axis direction when pressurized. In order to account for this, the opposite of the relationship established in Equation (2.23) $\left(v_0 = -\frac{a}{b} u_0. \right)$ was substituted into Equation (2.18) resulting in a potential energy formulation with only the unknowns w_0 and u_0. The corrected energy formulation is then minimized with respect to w_0 and u_0 to establish a relationship between the input pressure P, the contraction u_0, and the force generated by the actuator F. In the elastic range, an analytic formula can be found to relate the input pressure,

force, and contraction of the actuator. However, this is impossible to achieve in the nonlinear regime. Therefore, as previously mentioned, the elastic solutions method is used to determine the performance of the actuator. This is accomplished through the use of numerical software to approximate the maximum force and contraction of the actuator at various inputs pressures through an iterative process. The differential potential energy Equations (2.22a),(2.22c) in the elastic range are used as a first approximation. Subsequently, a nonlinear model, $E_x(\varepsilon_x)$ for the Young's Modulus in the x-axis direction is substituted for E_x. Utilizing the average strain in the x-axis direction as the input to the nonlinear model, an iterative approximation of the maximum actuator contraction and force generation of the FPAM is found.

2.4 Experimental Validation

An experimental apparatus was created to measure the mechanical performance of the FPAM (SCU & MCU). As seen in Figure 2.7, the experimental setup is composed of a motorized test stand (ESM301, Mark-10) capable of providing single-axis distance measures, a single-axis load cell (STL-50, AmCells), a pressure gauge and regulator, a data acquisition unit (USB-6000, National Instruments), and a LabVIEW program designed to collect force and time data.

Prior to experimentation, the FPAMs were cyclically loaded, Figure 2.12, to "train" the actuators. The training consisted of each FPAM being pretensioned to 0.5 N (chosen to minimize slack in embedded fibers, while also reducing effects on actuator performance), pressurized to 103 kPa (chosen to avoid failure), and then manually contracted and extended over the FPAM's max displacement (14.3%) at 103 kPa using the Mark-10 at a speed of 30mm/min. This procedure was to ensure repeatable behavior by overcoming initial adhesive forces between the substrates and fibers (leftover from fabrication) in addition to providing some level of constant plastic deformation to the substrates and fibers. Subsequently, the experimental setup was used to conduct

three separate procedures.
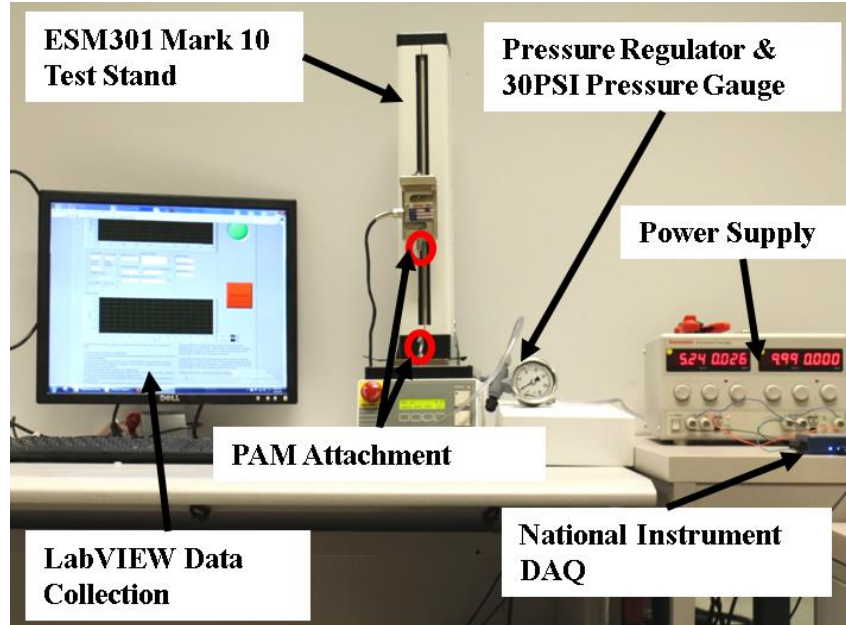
Figure 2.7: Diagram of Experimental apparatus used to conduct force and contraction experiments

In the first procedure, Figure 2.11, the FPAMs were held fixed at their rest length (contraction = 0), while the air chamber was pressurized from 0-151 kPa in increments of 6.89 kPa. At the start of this procedure the FPAMs were manually pretensioned to 0.5 N by the Mark-10. The LabVIEW data collection program and Mark-10 were then zeroed. Pressurization was then systematically applied in the aforementioned increments, allowing for the generated force of the actuators to reach a steady state value (5-10 seconds after pressurization) before the data was recorded. This process was then repeated to collect additional data points at each input pressure. In this manner, the maximum force generation of the actuator due solely to pressurization could be properly recorded.

In the second procedure, Figure 2.10, the FPAMs were pressurized at no load (applied force = 0), and allowed to freely contract while the air chamber was pressurized from 151-0 kPa in increments 6.89 kPa. At the start of the procedure the FPAMs were placed on the Mark-10. The LabVIEW data collection program and Mark-10 were then zeroed. Subsequently, the Mark-10 was

lowered to allow the actuators space to contract. Pressurization was then systematically applied in the aforementioned increments. At each increment, the test stand was raised until the LabVIEW program showed a minor increase in the force reading generated by the actuator. At this point, the Mark-10's displacement was recorded to provide values for the contraction of the actuators. In addition, calipers were used to provide secondary verification of the contraction readings. This process was then repeated to collect additional data points at each input pressure. In this manner, the maximum contraction of the FPAMs due solely to pressurization could be properly recorded.

In the final procedure, Figure 2.9, the FPAMs were pressurized at their rest lengths (contraction = 0) then manually contracted to no load conditions (applied force = 0). At the start of this procedure, the FPAMs were preloaded to 0.5 N by the Mark 10. The LabVIEW program and the Mark-10 were then zeroed. Subsequently the FPAMs were pressurized and allowed to reach steady state values (5-10 secs after pressurization) prior to being contracted at a speed of 10 mm/min. This procedure was conducted at pressures ranging from 0-151 kPa (FPAMs failed at 151 kPa) in increments of 17 kPa, in order to provide an example of the traditional unloading curve (force vs contraction at various pressure) for pneumatic actuators.

These three experimental procedures were conducted, in order to provide an accurate measure of the characteristic force generation and the maximum contraction within the pressure range. In addition, tensile tests were conducted to determine the effective tensile modulus E_x in the x-axis direction (Figure 2.8). At the start of this test, the actuators were pretensioned to 0.5 N to minimize slack. The LabVIEW program and Mark-10 were zeroed. Subsequently the actuator was stretched at a rate of 10 mm/min from its initial pretensioned conditions. The tensile modulus was found to be linear up to about 5% strain, at which point the modulus increases until failure. The measured tensile modulus, when converted to a flexural composite modulus, was found to be

around 340 kPa, which is much lower than the 1.71 GPa calculated using just the rule of mixtures found in Equation (2.5a). We believe this is due to how the fibers are oriented in the completed actuator. The Kevlar fibers were clamped at a single point at each end, which unevenly distributed stress along the fiber direction, and resulted in the occurrence of some slack. In addition, slippage between the Kevlar fibers and the silicone substrate during actuation also contributed to the smaller modulus. As such, the experimental tensile modulus was used to approximate the values for E_y, G_{xy}, v_{xy}, and v_{yx}, which were substituted into the model.

2.5 Results and Discussion
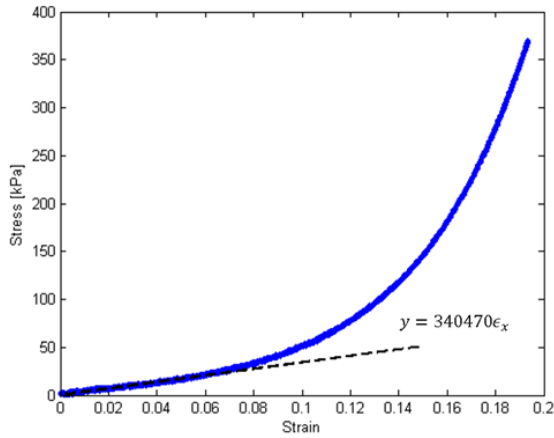
Figure 2.8: Experimental stress-strain relationship of FPAM up to 20% strain.
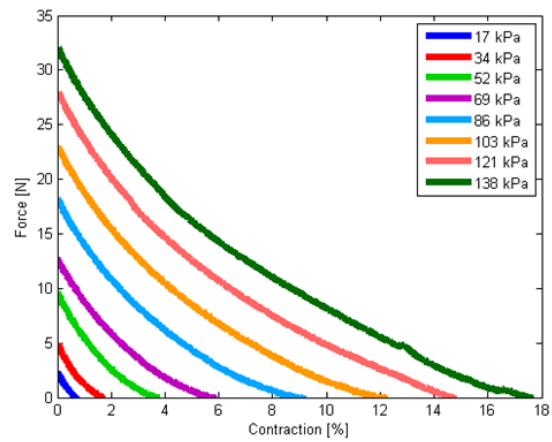
Figure 2.9: FPAM force-contraction relationship at pressures ranging from 0 to 138 kPa.

Characterization of the FPAM's mechanical performance can be found in Figure 2.9, which provides an example of the resulting force-contraction relationship of the SCU PAM up to 138 kPa (chosen to ensure actuators were not pushed to failure). Ultimately, through experimentation the SCU and MCU, the FPAMs were observed to fail at pressures around 150 kPa and 138 kPa, respectively. However, the failure mechanism that occurs is due to crack propagation, at high pressures, as the Kevlar fibers shear through the substrate, as opposed to delamination failure modes along the edges, which occurred more often and erratically in the previous design [31]. This is an improvement, as the observed failure mode can be accounted for in design and operation by

setting a safety margin for input pressures. It is important to note that both the SCU and MCU have similar mechanical performances although the MCU failed more quickly than the SCU, as shown in Figures 2.10 and 2.11. Additionally, an example of the repeatability of the results can be found in Figure 2.12, where the PAM reached a near constant force generation after 3 to 4 cycles at 103 kPa.

The SCU generated a maximum force of 35.7 ± 1 N and a maximum contraction of 20.5% ± 0.1% (2.87 mm ± 0.09 mm), while the MCU generated a maximum force of 38.1 ± 1 N and a maximum contraction of 22.4% ± 0.3% (9.42 mm ± 0.13 mm). The MCU, which is equivalent to three SCUs in series, was within 6.7% of the maximum force generation of the SCU and within 9.4% of thrice the maximum contraction of the SCU. The results are close to what would be expected in the ideal case despite the absence of inlet tubing between the three air volumes of the MCU design. This variation essentially adds an additional 12 mm to the deformable air volume, which may have affected the overall mechanical performance of the MCU. In addition, the larger form factor also affects the modulus of the MCU, when compared to that of the SCU, due to the increased interaction (contact forces) of the fibers and substrate between the fixed ends of the actuator. These issues, which will be addressed in future work through improved fabrication techniques, could be incorporated into the theoretical model for improved accuracy. This can be achieved by providing a new experimental modulus, as well as incorporating the additional 12 mm of deformable area as two additional air volumes of even size.

These experimental results were then compared to the theoretical model developed in this study. Both a linear and a nonlinear elastic moduli were utilized to numerically evaluate the theoretical model, due to our insight into the nature of the experimental procedures. During the contractile experiments, the deformation of the actuator remained in the elastic range as it was

allowed to reach an equilibrium position, which resulted in near zero *x*-directional strain. However, during the force experiments, despite the fact that the actuator length was held fixed, the PAM still deformed in the *y*- and *z*-axis directions as a result of input pressure. These deformations resulted in *x*-directional strains, which incited a strain-hardening effect within the PAM. Ultimately, the strain-hardening effect lead to an increase in the force generated by the PAM. In order to incorporate this behavior into the model, an 8th order Ogden model (hyperplastic material model)
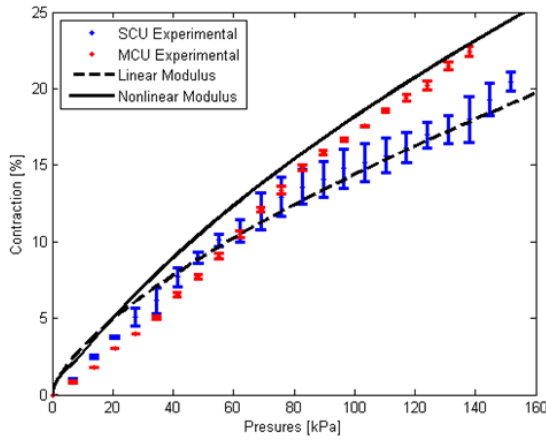
Figure 2.10: Maximum % contraction of FPAMs at pressures in the range of 0 – 157 kPa.
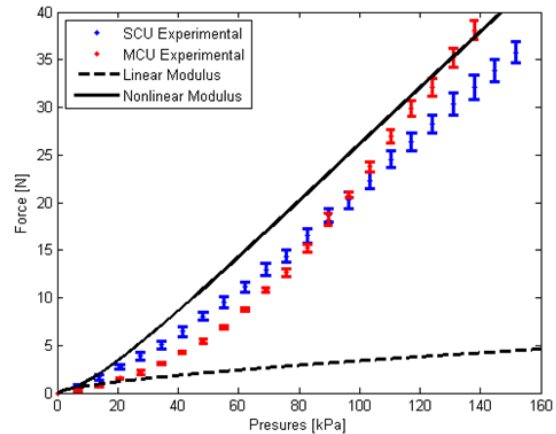
Figure 2.11: Maximum force of FPAM at pressures in the range of 0 – 157 kPa.

was fit to the data in Figure 2.8, and substituted into the model.

As can be seen in Figure 2.10, both the linear and nonlinear modulus approximations performed admirably in predicting the contraction of the SCU to within ± 0.67% and ± 2.55% contraction, respectively. Both modulus approximations accurately capture the trajectory of the contraction response to pressure. Although the linear model seems to predict the behavior of the SCU slightly better in this case, it is due to the underperformance of the SCU caused by the rigid components, such as the inlet and the plug, which contributed to the prevention of full muscle contraction more in the SCU than in the MCU. In regards to the force response to pressure, shown in Figure 2.11, only the nonlinear modulus was able to accurately predict both numerical values and trajectory of the experimental results. The theoretical model developed with the nonlinear

modulus approximated the force generation of the SCU to within ± 3.5 N, while the linear modulus predicted to within ± 13.3 N. This error with the linear approximation was associated with the nonlinear behavior seen in the stress-strain relationship of the FPAM (Figure 2.8). Overall, the development of the theoretical model with a nonlinear hyperelastic tensile modulus demonstrated high fidelity in approximating the performance of the actuators.

Further considerations for future work include the improvement of the mechanical performance of the presented actuator. The FPAM's maximum performance values, which are similar to that of other PAMs designed with embedded fibers [22, 31], are lower than those of traditional McKibben actuators [12, 13, 26, 35, 41] in general. However, this actuator is able to reach over 20% contraction with pressure inputs of 151 kPa, which is 2.5-5 times lower than the pressure inputs seen in the aforementioned McKibben actuators. As such, the FPAM is ideal for low pressure and low force applications, and will need to be customized through material selection for desired user tasks. For example, an increase in the *x*-directional modulus of the composite material will serve to increase the maximum force generated at the tested pressure ranges, while decreasing overall contraction and vice versa. Furthermore, the choice of base substrate can be chosen to reduce or increase the required pressure input for actuator deformation. Additionally, the slack within the fibers due to being clamped at a single point on both ends would need to be addressed. This design flaw served to reduce the overall force generated by the actuator within this study's experimental pressure range due to uneven stress distribution along the fiber strands. However, the fibers should be oriented and clamped in such a way as to evenly distribute the stress, reducing the ability of the fibers to slip through the substrate and allowing the material properties of the fibers and substrate to drive the FPAM's mechanical performance. In this manner, the fibers can be chosen with either higher or lower elastic moduli which would result in higher max forces

and lower max contractions or lower max forces and higher max contractions in the applied pressure range respectively. Ultimately, the FPAM will be optimized for increased maximum contraction and force generation at similar pressure ranges used within this study.
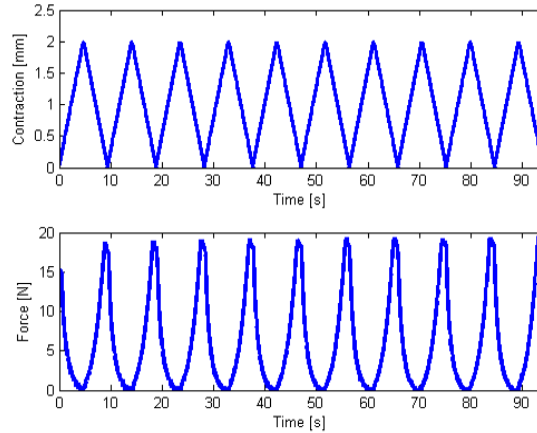
Figure 2.12: Cyclic loading of SCU at 103 kPa over a distance of 2 mm

In addition, the FPAM will be redesigned to incorporate embedded sensors. Due to the layered manufacturing process described, sensing capabilities can be easily added by altering the mold design to incorporate microchannels to be filled with a liquid conductor, such as eutectic Gallium-Indium (EGaIn) [5, 6], or by embedding a conductive soft polymer in an additional layer [7]. Subsequent experimentation with various microfluidic sensing designs such as those in [15, 16, 17, 18] will need to be conducted in order to optimize actuator performance and sensing capability. However, the added advantage of embedded multi-modal sensing in the proposed 2-D form factor will improve the FPAM's controllability, and thus the overall effectiveness of the FPAM. In addition, system identification to determine damping and spring coefficients at various pressures will need to be conducted. This will provide important information to improve the control of the FPAM, which is essential if it is to be used in a wearable orthotic or prosthetic device.

2.6 Conclusions

A simple fabrication technique was developed and employed to produce a two-dimensional flat PAM. A theoretical model was developed to numerically predict the overall contraction and force generation of the actuator through the use of Von Karman's formulation for large deformations and the energy methods. Additionally, experimental analysis of the maximum force generation and contraction at various input pressures was used to characterize the mechanical performance of the flat PAM. and to verify the fidelity of the theoretical model. In addition, a theoretical model was developed and demonstrated accurate approximation of the mechanical properties of the PAMs to within 2.55% contraction and ±3.5N force.

Acknowledgements

3 Biologically Inspired Sensorized Flat Pneumatic Artificial Muscles

Abstract

In recent years, soft components, such as pneumatic artificial muscles (PAMs), have been increasingly employed in order to design safer wearable devices. Despite the inherent compliance of the materials used to fabricate PAMs, the actuators are able to produce relatively large forces and work when compared to their weight. However, effective operation of these systems has traditionally required bulky external force and position sensors, which limit the maneuverability of users. In order to overcome these issues, inspiration was taken from organic muscle, which incorporates embedded sensors, such as Golgi tendon organs and muscle spindles, to provide real time positon and force sensing for the muscles. As such, a sensorized flat pneumatic artificial muscle (sFPAM) with embedded force and position sensors was designed and fabricated. In addition, a hyperelastic model was developed and verified through comparison with the experimentally characterized mechanical and electrical performance of the sFPAM. Furthermore, a sliding mode controller was implemented to demonstrate the feasibility of the embedded sensors to provide feedback during operation. Ultimately, a lightweight compact actuation system was designed with the ability to be seamlessly incorporated into a future wearable device.

Keywords: pneumatic artificial muscle (PAM), flat, actuators, soft robotics, design and manufacturing.

3.1 Introduction

Technological advances in robotic systems have led to the development of cheaper, more robust designs that are increasingly becoming everyday aspects of modern society. These systems encompass a plethora of applications including: autonomous vehicles, teleoperated medical devices, toys for children, personal robots, and wearable devices. An important consideration for researchers in this field centers on human-robot interactions which seek to foster safe and efficient working relationships and environments [42, 43, 44, 45]. This is particularly important in the design of wearable robotic devices, due to the higher risks involved with linking the mechanics of the human body to an external system. Thus researchers have sought to produce safe efficient systems through the implementation of complex control algorithms and innovative system designs [44, 45, 46].

One such innovation, which is particularly important to this study, can be found in the use of pneumatic artificial muscles, or PAMs, in the design of wearable devices [29, 31, 38, 47, 48]. PAMs, which are traditionally composed of soft elastomeric bladders constrained by flexible inextensible mechanisms, have increasingly been used in the field of robotics due to their favorable characteristics [12, 13, 14]. PAMs are composed of soft materials, which typically have elastic moduli and stiffnesses in the ranges of those of organic tissue, making them inherently safe when interacting with humans. These materials allow PAMs to remain lightweight and compliant, while being able to generate large forces when compared to that of their own masses. In addition, when pressurized, PAMs generate linear displacements and forces which can be utilized to produce desired movements. Despite the aforementioned properties of PAMs, operation of these actuators is complicated due to their nonlinear response to input pressure.

In order to overcome this caveat, designers have employed various external and internal sensors to detect the current state of the actuators during operation. However, current designs fall short of ensuring effective real-time control of compliant and compact designs. External sensors, including linear force gauges and strain sensors, increase the bulkiness and add undesirable rigidity to the overall system. Meanwhile, internal sensors, such as embedded conductive elements in the elastomeric air chamber for resistive sensing [7, 22, 23] or integrated braided conductive wires to the outer mesh structure for inductive sensing [24, 25], have not allowed for multimodal sensing due to difficulties arising from complex fabrication processes. A solution to this issue however, can be found in biological muscle systems, which operate similarly to PAMs.

Biological muscle, an organic soft tissue, is lightweight, compact, and capable of generating linear forces and displacements when stimulated by electricity. Muscles, which are typically found in antagonistic pairs throughout the human body, are composed of millions of contractile micro units known as sarcomeres, which are connected in series and in parallel to provide human-scale contractile forces and displacements. Although muscle contractions may be voluntary (consciously controlled) or involuntary (subconsciously controlled), both neurological control schemes employ embedded organic sensors to detect the current state of the muscle. These sensors, known as proprioceptors, detect the stretch, length, and tension of the muscle fibers, without increasing the muscle's overall form factor. The primary muscular sensory receptors are the muscle spindles and Golgi tendon organs [49, 50]. The muscle spindles are located along the muscle fibers (contractile region of the muscles) and serve to detect the overall length of the muscle, while the Golgi tendon organs are located in the muscle tendons (terminals of muscle) and detect the muscles' generated stress (Figure 3.1). These sensors work in unison to provide the

human body with a continuous stream of sensory data that is used to provide effective motor control of the muscle systems.

In seeking to replicate the properties of biological muscles and their sensors, this study focuses on the design, control, and experimental characterization of a biologically inspired integrated sensing and actuation system composed of a PAM with embedded sensors (Figure 3.1). The proposed design utilized a modified version of the flat pneumatic artificial muscle design (FPAM) proposed by [51] due to the simple layered fabrication method employed, as well as the ease in which multimodal sensing could be incorporated [31, 51].
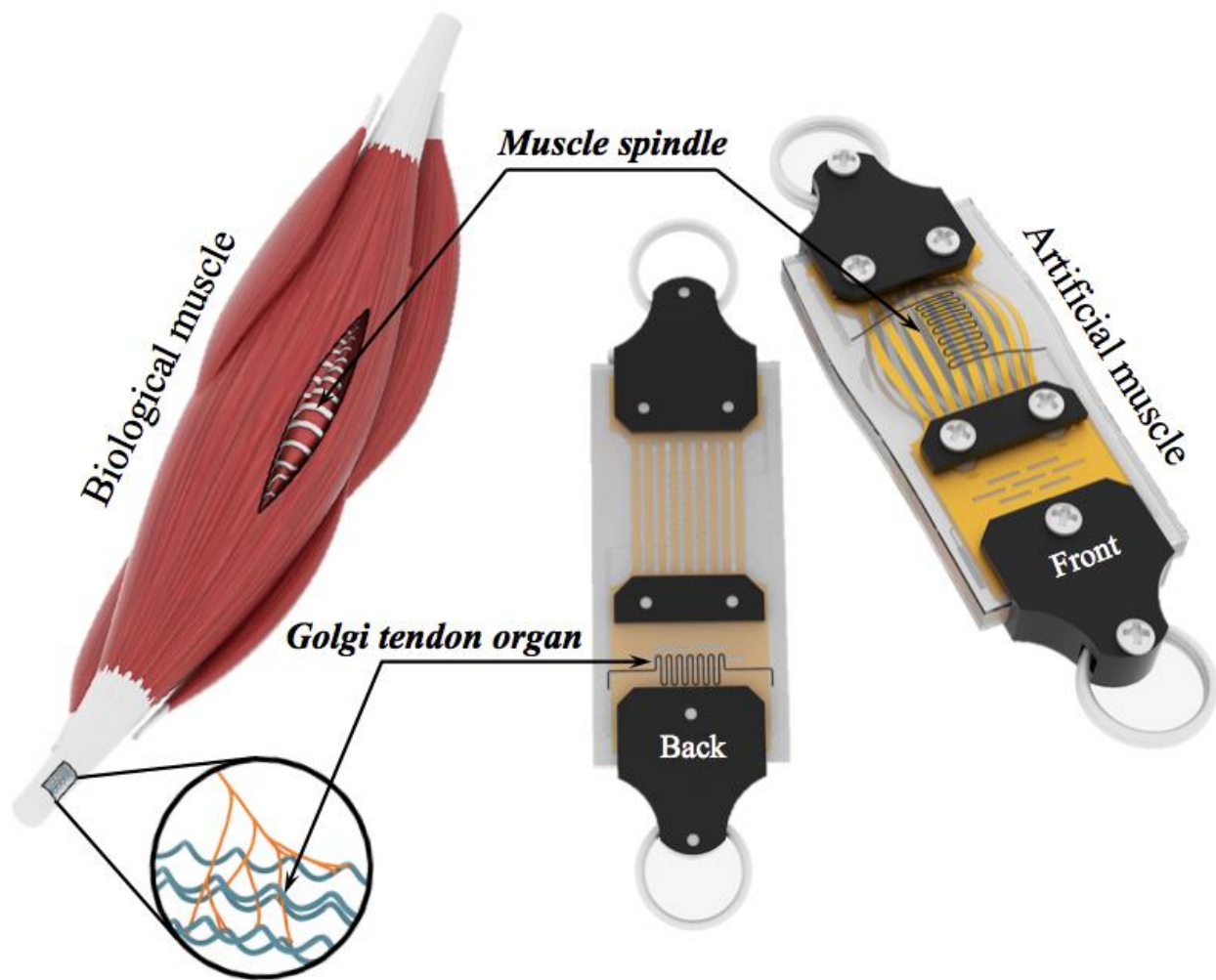
Figure 3.1: Schematic comparison of sensorized FPAM with biological muscle.

3.2 Design and Fabrication
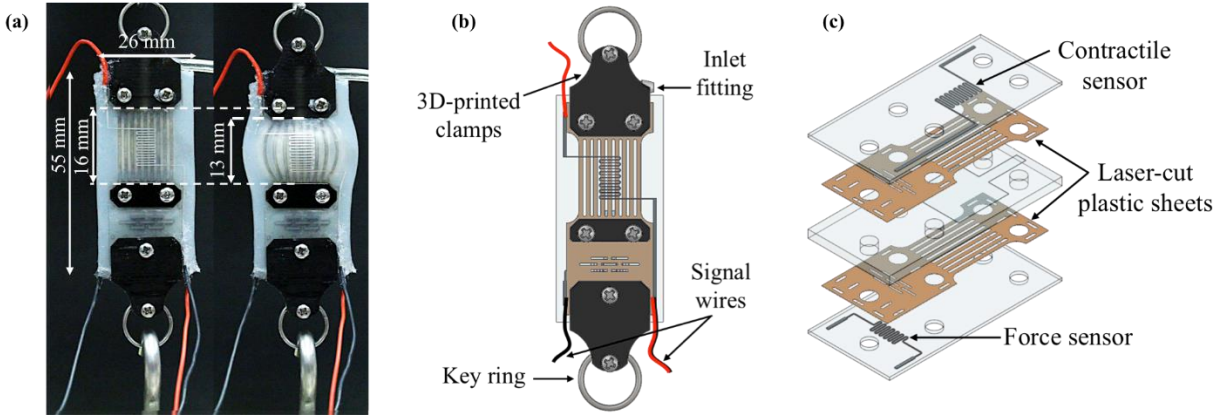
Figure 3.2: (**a**) Prototypes of the sensorized flat pneumatic artificial muscle 1) at rest and 2) inflated to 82.8 kPa. (**b**) Illustration of the completed actuator at rest with labels designating key components. (**c**) Exploded view provides clear visualization of the contraction and pressure sensors.

The previous FPAM design proposed by [51], was a thin rectangular actuator composed of a liquid cure silicone rubber substrate (Dragon Skin 10, Smooth On) that contained embedded Kevlar fibers (Kevlar 69 thread, McMaster Carr) [51]. The effects of the elastic substrate being constrained by the flexible inextensible fibers during pressurization of the PAM's zero-volume air chamber (ZAC) resulted in the generation of linear forcers and contractions [31, 51]. This study further improved on the effectiveness of the previous design through modifications to incorporate embedded multimodal sensing and to improve the repeatability of the fabrication process. This was accomplished through the substitution of the Kevlar fibers for a laser-cut flexible plastic sheet (PEI Ultem, McMaster Carr), the addition of a non-inflatable terminal to the actuator design, and the incorporation of microchannel negatives into the layer molds for both force and contractile sensing.

Core Fabrication

(1)   (2)   (3)   (4)

(5)   (6)

💧 Remove mask with water

Layer Fabrication

(7)   (8)   (9)   (10) Inject eGaIn

Remove air

Inject eGaIn

Seal microchannels with spin coater

Remove air
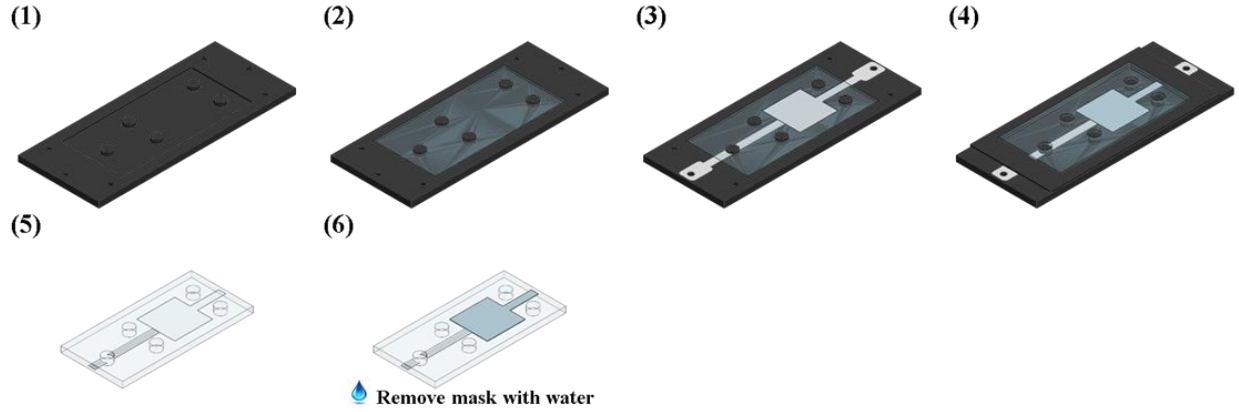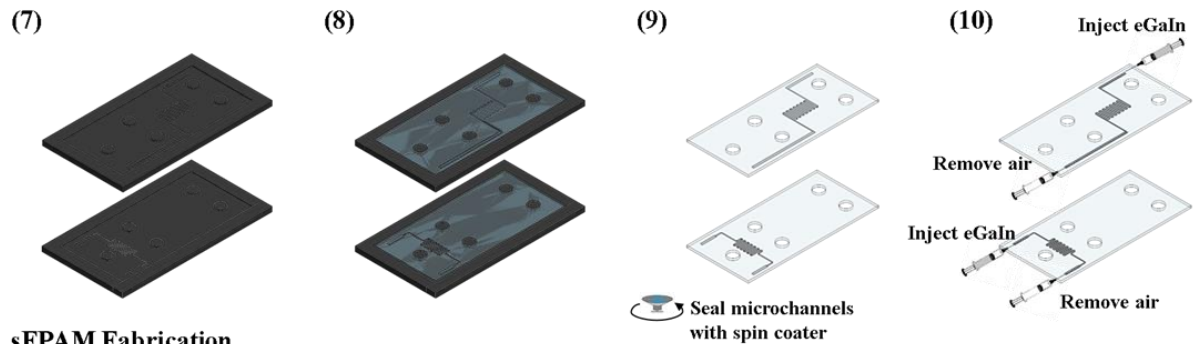
sFPAM Fabrication

(11)   (12)   (13)
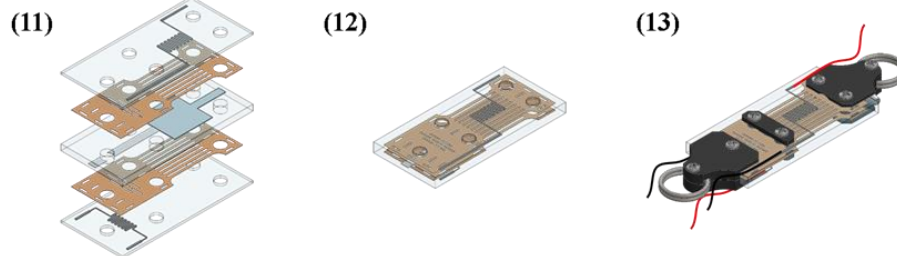
Figure 3.3: Fabrication process of sFPAM using water-soluble mask: (**1**) prepare bottom core mold, (**2**) pour liquid elastomer for bottom half of core, (**3**) place water-soluble mask, (**4**) place top mold and pour liquid elastomer for top half of core, (**5**) remove core after curing, (**6**) remove water-soluble mask with water, (**7**) prepare thin layer molds, (**8**) pour liquid elastomer to create thin outer layers, (**9**) remove thin outer layers after curing and seal microchannels by spin-coating thin layer on top, (**10**) Inject liquid metal into microchannels, (**11**) align plastic sheet, outer layers, and core, (**12**) then bond together using uncured elastomer, (**13**) finally 3D printed clamps are added and electrical wires are inserted into microchannels.

These alterations allowed for the design of the sFPAM with a constant stiffness tendon and deformable muscle, Figure 3.2, which contained a bioinspired Golgi tendon organ and muscle spindle fabricated using eutectic Gallium Indium (eGaIn), an extensively studied conductive liquid metal [5, 6] that has been embedded as a resistive sensor in various soft robotic systems [15, 16,

17, 18]. In particular, the laser-cut flexible sheet was integral to the current actuator design. The substitution of the sheet for the Kevlar fibers minimized misalignment issues that led to slack, and allowed for more rapid manufacturing of the desired sheet design. Additionally, a kirigami design patterned into the terminal tendon section of the sheet provided minor stretchability, which allowed the force sensor to change values during operation.

The proposed sFPAM was fabricated using a simple layered manufacturing process. The fabrication process, Figure 3.3, makes use of liquid silicone rubber and photopolymer (VeroBlack, Stratasys) molds, which were made using a 3D printer (Objet 30, Stratasys) in order to create two layers (thin silicone sheets) and a core (central substrate containing the ZAC) with an embedded water-soluble mask (Water Soluble Stabilizer, Paper Solvy). The mask is removed using water in order to create the ZAC. The layers were fabricated with embedded microchannels that were filled with eGaIn purchased from Alfa Aesar, in order to act as resistive liquid metal contractile and force sensors. Afterwards, the layers and core were stacked and bonded together to form the base actuator in the following order: silicone layer (force sensor), laser-cut plastic sheet (PEI Ultem, McMaster Carr), core, laser-cut plastic sheet (PEI Ultem, McMaster Carr), silicone layer (contractile sensor). Finally, an inlet fitting (5463K41, McMaster), flexible wiring (9564T3, McMaster), and 3D-printed clamps were then added to complete the actuator. A prototype of the PAM can be found in Figure 3.2(a). The base single cell actuator was made using Dragon Skin 10 silicone rubber (Smooth-On Inc) and had dimensions of 55 mm $\times$ 26 mm $\times$ 5.5 mm thick, with ZAC dimensions of 16 mm $\times$ 16mm $\times$ 0.1mm thick, and weighed about 17 grams. The microchannels (sensors) had cross sectional dimensions of 0.2 mm $\times$ 0.2 mm thick.

3.3 Hyperelastic Contraction Model
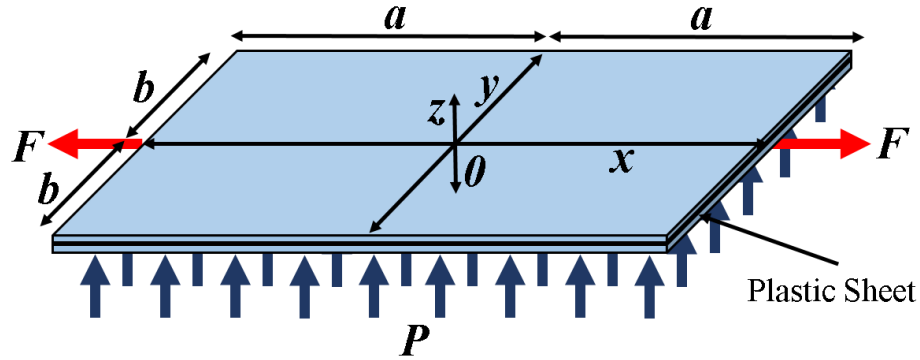
Figure 3.4: Diagram of top half of sFPAM depicted as a flat sheet under external force F and pressure P.

A theoretical model was previously developed using a modified von Karman's formulation for the large deformation of membranes and the energy method [32, 33, 34], by [51] in order to approximate the mechanical performance of the FPAM. In this study, the model was further built upon through the introduction of hyperelastic strain energy density formulations and geometric constraints. Initially, the sFPAM was modeled as two flat elastic rectangular composite sheets simply supported along their edges, Figure 3.4. The z-axis deflection

$$w(x,y) = w_0 \cos\frac{\pi x}{2a}\cos\frac{\pi y}{2b}, \tag{3.1}$$

theorized by Timoshenko [32, 33] for the elastic deformation of a simply supported membrane under uniform pressure, was utilized. Here x and y are the position from the center of the composite sheet parallel and perpendicular to the fiber direction respectively, and *2a* and *2b* are the dimensions of the sheet in the x-axis and y-axis directions, respectively. The modified von Karman formulation for a composite was calculated as,

$$\frac{1}{E_y}\frac{\delta^4\phi}{\delta x^4} + \frac{1}{E_x}\frac{\delta^4\phi}{\delta y^4} + \left(\frac{1}{G_{xy}} - \frac{v_{xy}}{E_x} - \frac{v_{yx}}{E_y}\right)\frac{\delta^4\phi}{\delta x^4} = \left[\left(\frac{\delta^2 w}{\delta x \delta y}\right)^2 - \frac{\delta^2 w}{\delta x^2}\frac{\delta^2 w}{\delta y^2}\right], \tag{3.2}$$

where E_x and E_y are the elastic moduli in the x- and y-axis directions, respectively, G_{xy} is the shear

modulus, v_{xy} is the Poisson's ratio due to the effects of y-axis stress on the x-axis deformation, v_{yx} is the Poisson's ratio due to the effects of x-axis stress on the y-axis deformation, and $\Phi(x,y)$ is the stress function defined as

$$\sigma_x = \frac{\delta^2\phi}{\delta y^2}, \tag{3.3a}$$

$$\sigma_y = \frac{\delta^2\phi}{\delta x^2}, \tag{3.3b}$$

$$\tau_{xy} = -\frac{\delta^2\phi}{\delta x \delta y}. \tag{3.3c}$$

The particular and homogenous solutions for the stress function Φ, were then solved for the boundary conditions of a simply supported plate, resulting in the complete stress function

$$\phi(x,y) = -\left[\frac{E_y a^2 w_0^2}{32b^2}\cos\left(\frac{\pi x}{a}\right) + \frac{E_x b^2 w_0^2}{32a^2}\cos\left(\frac{\pi y}{b}\right)\right. \tag{3.4}$$

$$+ x^2\left(\frac{E_y(\pi^2 a^2 w_0^2 + 16v_0 a^2 b) + E_x v_{yx}(\pi^2 b^2 w_0^2 + 16u_0 ab^2)}{64a^2 b^2(v_{xy}v_{yx} - 1)}\right)$$

$$\left.+ y^2\left(\frac{E_y v_{xy}(\pi^2 a^2 w_0^2 + 16v_0 a^2 b) + E_x(\pi^2 b^2 w_0^2 + 16u_0 ab^2)}{64a^2 b^2(v_{xy}v_{yx} - 1)}\right)\right]$$

and the final x-axis and y-axis displacement formulations

$$u(x,y) = \frac{u_0 x}{2a} + \frac{\pi w_0^2}{32a}\left[1 + \cos\left(\frac{\pi y}{b}\right) + \frac{v_{xy}E_y a^2}{E_x b^2}\right]\sin\left(\frac{\pi x}{a}\right) \tag{3.5a}$$

$$v(x,y) = \frac{v_0 y}{2b} + \frac{\pi w_0^2}{32b}\left[1 + \cos\left(\frac{\pi x}{a}\right) + \frac{v_{yx}E_x b^2}{E_y a^2}\right]\sin\left(\frac{\pi y}{b}\right), \tag{3.5b}$$

where w_0 is the maximum displacement in the z-axis direction, u_0 is the maximum displacement in the x-axis direction, and v_0 is the maximum displacement in the y-axis direction. With the formulation of solutions for $u(x,y)$ and $v(x,y)$, in addition to $w(x,y,)$, the displacement of any point in the composite sheet during elastic deformation was determined. Given that hyperelastic

solutions should reduce to the elastic formulations, in their linear regime, it can be assumed that the hyperelastic solutions take on a similar form as the elastic solutions. As such, the hyperelastic displacement formulations were assumed to take on the form

$$u(x, y) = \frac{u_0 x}{2a} + u_1 \sin\left(\frac{\pi x}{a}\right) + u_2 \cos\left(\frac{\pi y}{b}\right) \sin\left(\frac{\pi x}{a}\right),$$ (3.6a)

$$v(x, y) = \frac{v_0 y}{2b} + v_1 \sin\left(\frac{\pi y}{b}\right) + v_2 \cos\left(\frac{\pi x}{a}\right) \sin\left(\frac{\pi y}{b}\right),$$ (3.6b)

$$w(x, y) = w_0 \cos\left(\frac{\pi x}{2a}\right) \cos\left(\frac{\pi y}{2b}\right),$$ (3.6c)

where u_0, u_1, u_2, v_0, v_1, v_2, and w_0 are unknown constants to be solved for through the minimization of the system's potential energy, Π. In order to solve for these unknowns, a nonlinear hyperelastic strain energy density term, W, was incorporated. The composite sheets were assumed to be incompressible Neo-Hookean solids with deformation tensor, B, and right Cauchy-Green deformation tensor, C, defined as

$$B = \begin{bmatrix} \lambda_x & \frac{\varepsilon_{xy}}{2} & 0 \\ \frac{\varepsilon_{xy}}{2} & \lambda_y & 0 \\ 0 & 0 & \lambda_z \end{bmatrix},$$ (3.7a)

$$C = B^T B = \begin{bmatrix} \lambda_x^2 + \frac{\varepsilon_{xy}^2}{4} & \frac{\varepsilon_{xy}}{2}(\lambda_x + \lambda_y) & 0 \\ \frac{\varepsilon_{xy}}{2}(\lambda_x + \lambda_y) & \lambda_y^2 + \frac{\varepsilon_{xy}^2}{4} & 0 \\ 0 & 0 & \lambda_z^2 \end{bmatrix}.$$ (3.7b)

The strain energy density of a Neo-Hookean solid, is defined as the shear modulus multiplied by the first invariant, or trace, of the right Cauchy-Green deformation tensor, which resulted in the strain energy density formulation

$$W = \frac{E}{6}\left(\lambda_x^2 + \lambda_y^2 + \lambda_z^2 + \frac{\varepsilon_{xy}^2}{2} - 3\right),$$ (3.8)

with the resulting volumetric stretch ratio defined as

$$J = \det(B) = \lambda_x \lambda_y \lambda_z - \frac{\varepsilon_{xy}^2}{4} \lambda_z, \tag{3.9}$$

The normal stretches λ_x in the x-axis direction, λ_y in the y-axis direction, and shear strain ε_{xy} were defined as

$$\lambda_x = \frac{\delta u}{\delta x} + \frac{1}{2}\left(\frac{\delta w}{\delta x}\right)^2 - z\frac{\delta^2 w}{\delta x^2} + 1, \tag{3.10a}$$

$$\lambda_y = \frac{\delta v}{\delta y} + \frac{1}{2}\left(\frac{\delta w}{\delta y}\right)^2 - z\frac{\delta^2 w}{\delta y^2} + 1, \tag{3.10b}$$

$$\varepsilon_{xy} = \frac{\delta u}{\delta y} + \frac{\delta v}{\delta y} + \frac{\delta w}{\delta x}\frac{\delta w}{\delta y} - 2z\frac{\delta^2 w}{\delta x \delta y}, \tag{3.10c}$$

while λ_z, the stretch in the z-axis direction, was found from the incompressibility constraint $J = 1$. In addition to the incompressibility constraint, 2 additional constraints were applied to the system due to the nature of the composite sheets. Firstly, due to the presence of the laser-cut plastic sheet, the average x-axis stretch of the composited sheet is constrained. In other words, the length and location of the plastic sheet within the composite dictated the overall deformation of the actuator. This constraint was defined as $\lambda_{x,avg} = 1 + \frac{F}{AE_c}$, where F is the acting x-directional force along the edges $x = \pm a$, A is the area which the force acts on, and E_c is the x-direction Young's modulus of the composite sheet. Here $\frac{F}{AE_c}$ is equivalent to the strain induced by the deformation of the composite sheet by the applied force at the edges. This geometric constraint resulted in the following relationship between w_0 and u_0,

$$w_0 = \frac{1}{\pi^2}\sqrt{16u_0 a + 8\frac{Fa^2}{E_c bh}}. \tag{3.11}$$

Secondly, the deformed volume of the composite sheet had to be equivalent to the initial volume

due to the incompressibility constraint. This was accomplished by defining the x, y, and z positions of the composite sheet as $X = x + u(x, y)$, $Y = y + v(x, y)$, and $Z = z + w(x, y)$, where X, Y, and Z, are the deformed Cartesian coordinates of a point in the composite sheet. The initial volume was then compared to the deformed volume such that $V_0 = \iiint |V| \, dxdydz$, where V, the change in variable between the coordinate systems, is the determinant of the Jacobian of *(X,Y,Z)* with respect to *(x,y,z)*. This volumetric constraint resulted in the following relationship between v_0 and u_0,

$$v_0 = -\frac{2u_0 b}{2a + u_0}. \tag{3.12}$$

Utilizing the relationships found from the applied constraints, the potential energy of the system could then be defined as

$$\Pi = 2 \iiint W \, dV - 2W_p - W_F, \tag{3.13}$$

where $\iiint W \, dV$ is the strain energy of a composite sheet, $W_P = \iint [Pw(x, y)] \, dxdy$ is the work done by the applied pressure on a sheet, and $W_F = Fu_0$ is the applied force at the loaded edges $x = \pm a$. Subsequently, Equations (3.11) and (3.12) were substituted into (3.13). *Π* was then minimized with respect to the unknowns u_0, u_1, u_2, v_1, and v_2 *(i.e.* $\frac{\delta \Pi}{\delta u_0} = 0)$ to establish a relationship between the required input pressure, *P*, and the maximum generated force, *F*, & contraction, u_0. The mathematical solver Maple was used to find an analytic solution $P(u_0, F)$. The theoretical model developed was then compared to experimental data in order to further assess the effectiveness and fidelity of the model to approximate the behavior of the sFPAM.

3.4 Experimental Apparatus
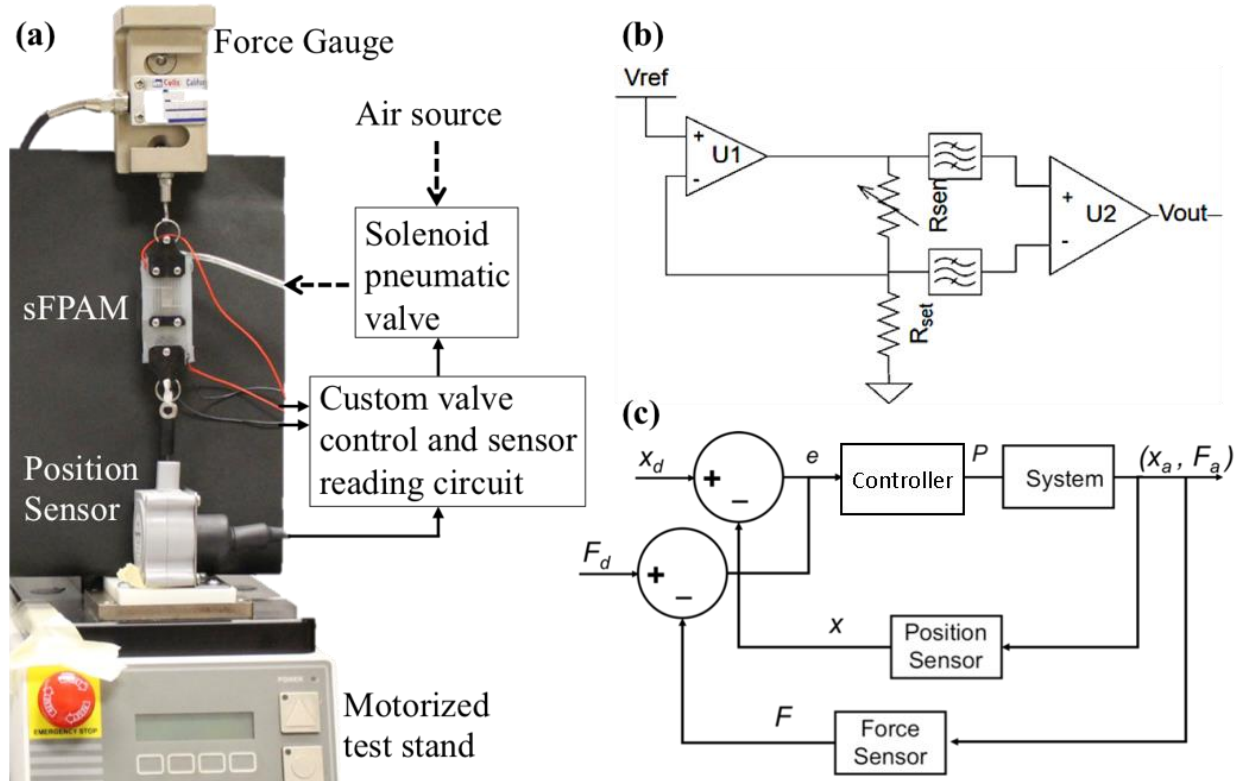
Figure 3.5: (**a**) Diagram of Experimental apparatus used to conduct force and contraction experiments. (**b**) Diagram of sensor amplification circuit. (**c**) Block diagram of controller used to implement force and position control.

The sFPAM was subjected to experimentation in order to characterize its mechanical and electrical performance, as well as demonstrate its feasibility to be controlled. The experimental characterization was conducted using a single-axis motorized test stand (ESM301, Mark-1) equipped with a single-axis load cell (STL-50, AMCells), a National Instruments USM-600 Data Acquisition Unit (DAQ), a 30 psi pressure gauge and regulator (McMaster Carr), a custom amplifying PCB, and a custom LabVIEW program designed to collect experimental data. Using this experimental apparatus, Figure 3.5(a), the sFPAM was subjected to a set of experimental procedures in order to characterize the mechanical performance of the actuator and determine the corresponding sensor data during operation. The actuators were pretensioned to 0.5 N prior to experimentation in order to minimize errors in actuator performance due to slack and/or differing

initial conditions. After the application of the aforementioned pretension, the actuators were subjected to tests in order to characterize the force vs contraction response, determine the maximum force generation and contraction with corresponding sensor data, and identify the real-time effectiveness of the sensors at pressures ranging from 0 to 82.8 kPa (above which failure occurs).

3.4.1 Experimental Characterization

The force vs contraction response characterization was conducted by installing a single sFPAM at rest in the experimental apparatus and holding it fixed (contraction = 0 mm). After the actuator was pretensioned, the LabVIEW program was tared. Subsequently, a constant pressure in the aforementioned pressure range was applied, inducing an increase in the force reading of the program. After the force reached a steady state value, the sFPAM was then manually contracted at a speed of 10mm/min until the LabVIEW program's force reading returned to zero. This procedure was repeated in order to produce the force vs contraction characterization of the sFPAM.

In the procedure to identify the maximum force output of the sFPAMs due solely to pressurization of the air volume, the actuators were placed in the experimental apparatus and held fixed at their rest length (contraction = 0 mm) throughout the experiment. Following the application of the pretension, the program was tared and the actuators were pressurized from 0 to 89.7 kPa in increments of 6.9 kPa. At each increment, the force was allowed to settle to a steady state value, at which point data was recorded for the maximum generated force and resistance change of both the force and contractile sensors.

The maximum contraction of the sFPAMs was identified through the experimentation in no load conditions (applied force = 0). The actuators were placed on the experimental apparatus with one end free to move, but initially maintained physical contact with the base of the Mark-10

test stand. The Mark-10's distance measure was then tared. Subsequently, the actuators were pressurized from0 to 89.7 kPa in increments of 6.9 kPa. At each increment the actuators freely deformed due to the input pressure, contracting along the axial direction. The actuators were then lowered until their free ends once again contacted the base of the test stand. At this point, the maximum contraction and resistance change of both the force and contractile sensors were recorded.

The *x*-axis tensile modulus was also found experimentally. The actuators were pretensioned to 0.5N prior to testing. Subsequently the actuators were stretched to failure. Using the rule of mixtures, the effective fiber modulus was calculated [39, 40]. The results of these experimental procedures were then used to develop a controller for force and position control of the sFPAM.

3.4.2 Force and Position Control

A custom amplifier PCB was used to measure small changes in the resistance of the sFPAM. This PCB drives the sensor with a precise reference current, then measures the voltage across the sensor leads. The sensor resistance can then be calculated using Ohm's law: $R_{sen} = \frac{V_{sens}}{I_{drive}} = \frac{V_{sens}}{V_{ref}/R_{set}}$. In the circuit, Figure 3.5(b), Operational Amplifier U1 (OPA2377, Texas Instruments) is used to drive a constant current set by R_{set} and V_{ref}. The Instrumentation Amplifier U2 (LTC6915, Linear Technology) outputs a voltage proportional to the voltage across the sensor. The gain of U2 is adjusted by on-chip resistors manually configured through digital inputs. An internal 3kHz switched capacitor circuit allows for zero drift. Two single-pole RC low-pass filters between the sensor and U2 are used to limit aliasing. The 12-bit ADC in the USB-600 DAQ records the output voltage. This circuit allows for precise, independent control of drive current and amplifier gain. Drive current is set based on the geometry of the sensor to avoid thermal effects. Next, the maximum amplifier gain is selected that maintains the output voltage within

supply rails for the full working range of the sensor.

This amplification circuit, alongside a microcontroller and two solenoid valves, was then used to implement a sliding mode controller. As seen in Figure 3.5(c), the control scheme used both the force and position as inputs to the controller. The controller developed prioritized position over force, through the choice of system gains. During experimentation, the actuators were subjected to either force or position control tests, in order to determine the viability of the overall system to be controlled. During position control experiments, the actuators were fixed to a stationary mount on one side, and the constant spring force position sensor on the other. The embedded sensor signals were amplified and sent to the microcontroller, after being calibrated, and used to implement the desired position control tests. During force control experimentation, the sFPAMs were fixed the force gauge on one end, and a stationary mount on the other. After being pretensioned, the actuators were then subjected to the designed control algorithm. During both the position and force control experiments, the force gauge and constant spring force position sensor were used to provide base values for comparison of how effectively the embedded sensors performed during real-time operation.

3.5 Results and Discussion
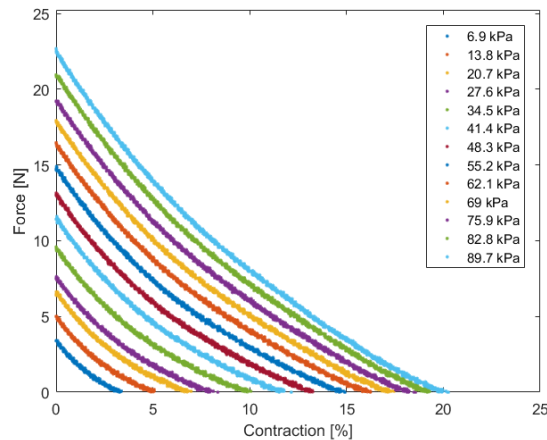
Figure 3.6: sFPAM force-contraction relationship at pressures ranging from 0 to 82.8 kPa.

The experimental data collected for the sFPAM was utilized to characterize the mechanical performance of the actuator. In addition, the resulting resistance changes of the contractile and force sensor were mapped to the mechanical performance in order to provide a relationship to be used for the design and implementation of the controller. Figure 3.6 provides an example of the sFPAMs' force-contractile relationship at pressures ranging from 0 to 89.7 kPa. At pressures above 89.7 kPa, the actuators failed due to the laser-cut plastic sheet shearing during bending. The maximum contractions and generated forces of the sFPAM over the operational pressure range are found in Figures 3.7(a)-3.7(b). In addition, experimental values were compared to the theoretical model developed and showed close agreement.
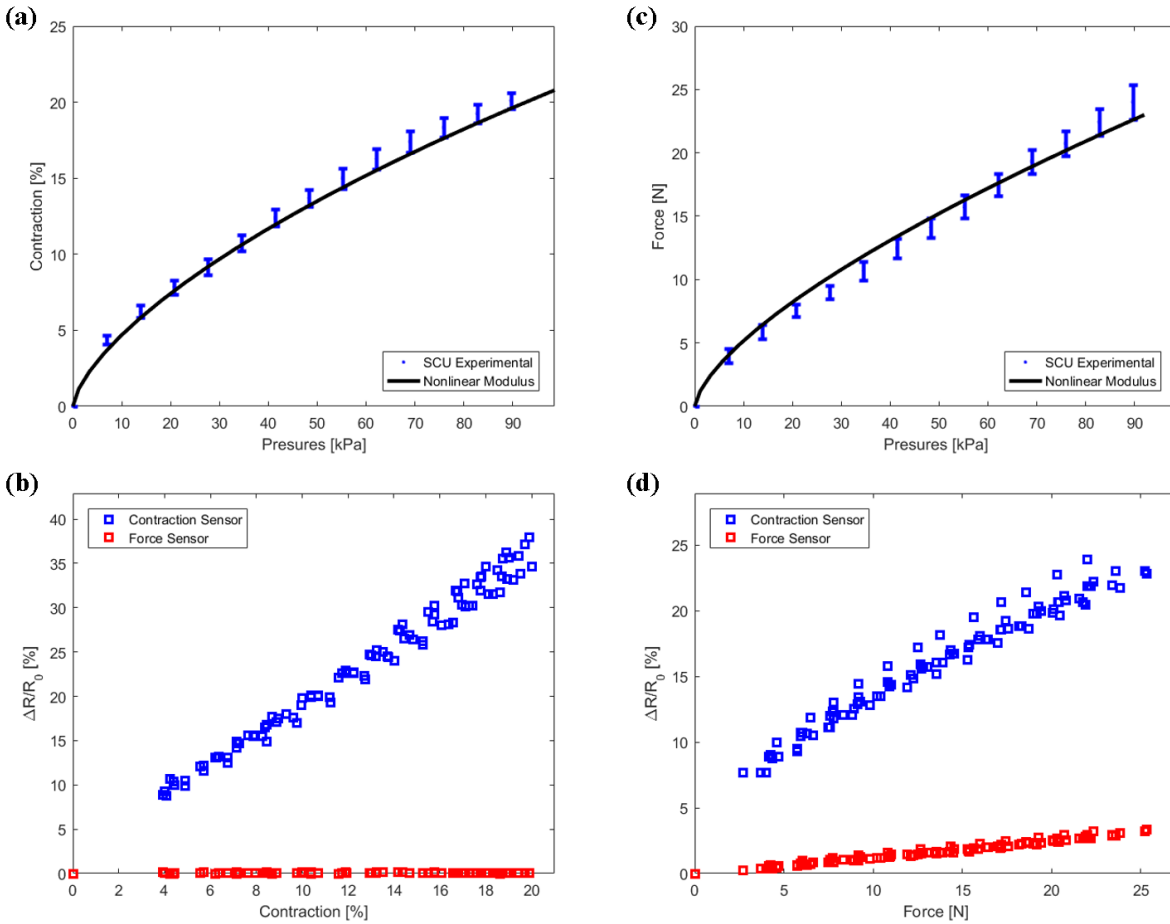
Figure 3.7: (**a**) Maximum % contraction of sFPAMs at pressures in the range of $0 - 89.7$ kPa. (**b**) Maximum force of sFPAM at pressures in the range of $0 - 89.7$ kPa. (**c**) Resistive response of force and contractile sensors due to contraction. (**d**) Resistive response of force and contractile sensors due to force.

Overall the sFPAM produced a maximum contraction of $19.8 \pm 0.2\%$ and maximum force of 24 ± 1.37 N. The theoretical model approximations predicted the contraction of the sFPAM to an average root mean squared error (RMSD) of 0.47% contraction (max RMSE 0.83%) and 0.68N force (max RMSE 1.45 N). Additionally, the model accurately captured the trajectory of both the contractile and force responses to input pressures. The corresponding sensor values can be found in Figures 3.7(c)-3.7(d). The effects of contraction on the sensors specifically, can be found in Figure 3.7(c). As shown, the contractile sensor exhibited a linear response to input pressure when the sFPAM was allowed to freely deform to its maximum contraction. Overall the contractile sensor changed $36.4 \pm 1.2\%$ in resistance, resulting in a resolution of 0.54 percent contraction to percent change in resistance. In addition, the force sensor remained nearly constant maxing at a 0.15% change in resistance which is less than a twentieth of the respective change due to the sFPAM's generated force. This result demonstrated that the force sensor was minimally affected by contraction, and thus could be considered completely decoupled from the effects of contraction, which would be key to implementing effective control of the sFPAM in real world applications.

The effects of force on the sensors is found in Figure 3.7(d). The force sensor changed 3.1 $\pm 0.2\%$ in resistance and resulted in a resolution of 8 N of force to percent change in resistance. However, there was a more significant coupling between the contractile sensor and the force generated by the actuator. Despite the sFPAM being held fixed during max force experiments, the air volume still deforms slightly in the z-axis direction, inducing a change in the resistive sensor that maxed out at $23.2 \pm 0.4\%$ resistance change. The change in the contractile sensor due to force is about two-thirds the respective change due to contraction for the actuator. However, because of the advantageous decoupling of the force sensor from contraction, as previously mentioned, the

contractile sensor coupling could be readily alleviated during development of the control algorithm.
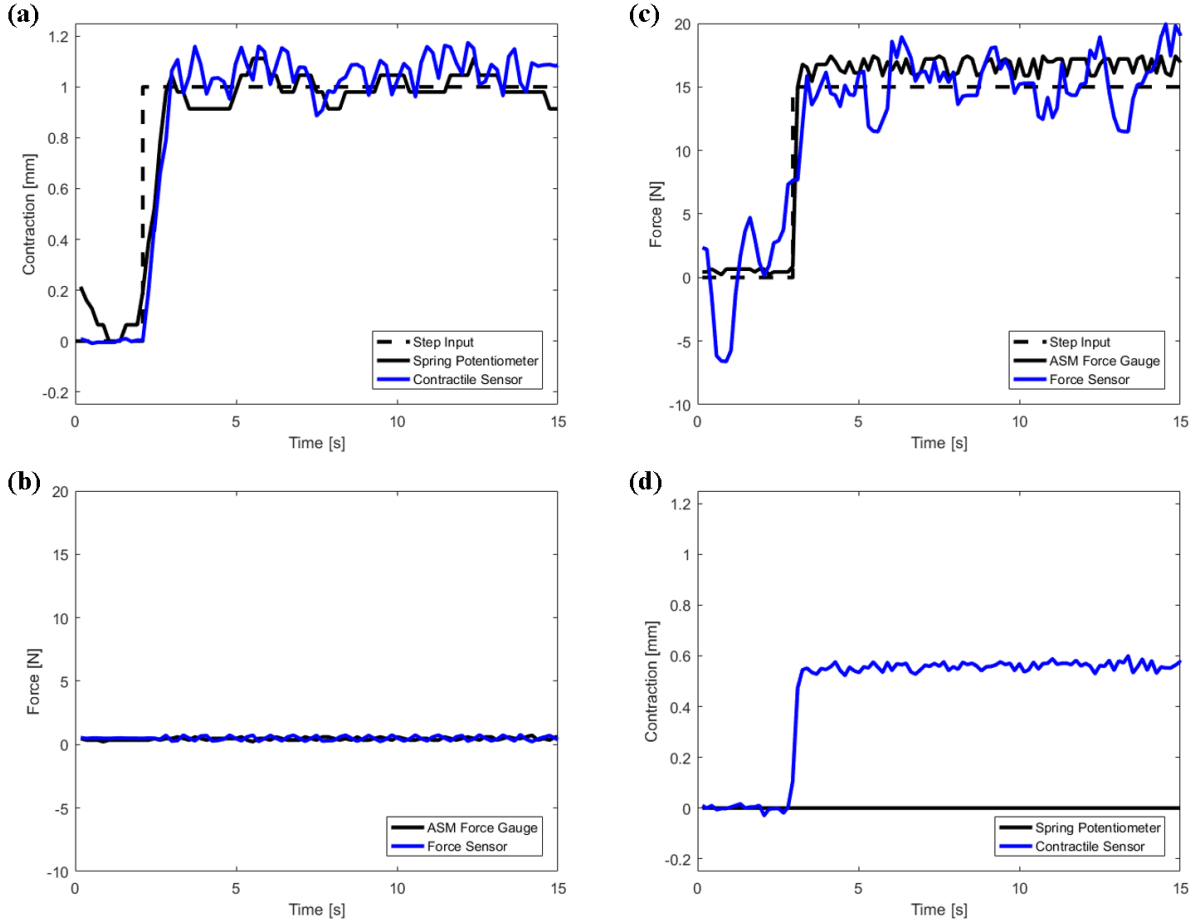
Figure 3.8: (**a**) System response during position control experimentation. (**b**) Corresponding force sensor response during position control experimentation. (**c**) System response during force control experimentation. (**d**) Corresponding contractile sensor response during force control experimentation.

Force and position control experiments were conducted to demonstrate the feasibility of the sFPAM to reach desired set points. For position control experiments, an example of which is provided in Figures 3.8(a)-3.8(b), the actuator was able to reach desired step inputs with a rise time of 0.82 s. Meanwhile, during force control experiments, an example of which is provided in Figure 3.8(c)-3.8(d), the actuator was able to reach desired step inputs with a rise time of 0.28 s and an average error of 1.5 N. The control scheme implemented in both cases relied solely on proportional

3.6 Conclusion

In this study the sFPAM, a novel pneumatic actuator with embedded sensors, was designed and fabricated. A modification to previous fabrication techniques for the manufacture of FPAMs was made through the substitution of a patterned laser-cut plastic sheet, which served an integral role in the design of the overall integrated sensing and actuation unit that is the sFPAM system. In addition, an analytic hyperelastic theoretical model capable of predicating the behavior of the sFPAM was developed. This model provides researchers and designers with a means to effectively select dimensions and materials for the sFPAM in order to produce forces and contractions within specific pressure ranges in order to successfully complete their desired tasks. In addition, due to the use of the plastic sheet, researchers can quickly iterate through sheet patterns in order to optimize the mechanical and electrical performance of the sFPAM.

Ultimately, a sensorized flat pneumatic artificial muscle capable of acting as a compact, readily deployable, standalone system which can easily be incorporated into a wearable device was developed. The sFPAM, which contained embedded force and contractile sensors that mimic the behavior of organic sensors found in human muscles (namely Golgi tendon organs and muscle spindles), was experimentally characterized and demonstrated favorable agreement with the developed hyperelastic model. Additionally, the feasibility of the system to be controlled to desired force and positon set points was displayed. However, additional considerations should be made to further improve the performance of the overall system.

Although controlled operation was successfully demonstrated, sensors should be modified to improve two key defects. Firstly, microchannel location and layout should be optimized to minimize the coupling effects of the contractile sensor. Ultimately the contractile sensor should have minimal change in its signals during purely force based experimentation or operation.

Minimization of the coupling effect should reduce the complexity of control algorithms required for effective real time operation of the sFPAM. Secondly, the sensitivity of the force sensor should be improved. This can be achieved by switching to capacitive sensing, utilizing a soft polymer instead of the liquid resistive sensing, optimizing the Kirigami pattern used on the laser-cut plastic sheet, or utilizing a higher resolution fabrication process for molds to create microchannels for improved resistive sensing. These improvements should ensure higher fidelity in the design of position and force controllers for set point and trajectory tracking inputs with varying loads, similar to what the sFPAM would experience during real world applications.

Acknowledgements

4 Fiber-Reinforced FPAM for the Suppression of Hand Tremor

Abstract

Tremor, including essential tremor (ET) and those associated with Parkinson's disease (PD), is the most common movement disorder affecting humans in modern society. Current solutions involving medication or surgical options can be very expensive, while wearable assistive devices fall short of providing an effective compact design for the suppression of the aforementioned tremor types. In order to overcome these limitations, a prototype flat pneumatic actuator (FPAM) capable of being placed into a custom glove for everyday use was created. A theoretical model was developed to approximate the behavior of the actuator. Furthermore, experimental characterization was conducted to measure maximum deflection angles and bending force generated at the tip of the actuator. Experimental data compared favorably to the theoretical model, which was subsequently used to aid in the development of an open-loop control scheme to simulate active compensation of tremor created by ET and PD on a human index finger. Results demonstrate the feasibility and effectiveness of the prototype FPAM to stabilize tremors within the finger, despite the lightweight, compact design of the system.

Keywords: flat pneumatic artificial muscle (FPAM), PAM, actuators, soft robotics, design and manufacturing, hand tremors, tremors.

4.1 Introduction

The human body is the subject of various movement disorders, the most common of which is known as tremor [52, 53, 54]. Tremor is characterized as an involuntary, rhythmic movement

which manifests at the joints, inducing uncontrolled oscillatory deflections [54, 55, 56, 57]. The most prevalent instances of this disorder may occur naturally, as in the case of physiological tremor (PT), or as part of a medical syndrome, as in the cases of essential tremor (ET) and Parkinson's disease (PD). The causes behind each of these instances vary, resulting in medically distinguishable characteristic behaviors for the aforementioned tremor types. In the case of PT, which affects all individuals, tremors are characterized by 8–12 Hz oscillations, typically of small amplitudes (0°–2.5°), making them invisible to the naked eye [56, 57, 58]. Researchers have identified a mixture of mechanical resonance, synchronization of motor unit firing, and instabilities in the stretch reflex arc as causes of PT [56, 57, 58]. ET and PD however, are characterized by slower easily visible oscillations (amplitudes of 0°–20°) in the range of 4–8 Hz [57, 58, 59]. In the case of ET, abnormal oscillations occur during voluntary movement (action tremor) and are characterized as monosymptomatic neurogenic tremors [54, 57, 60, 61]. Meanwhile, PD is characterized by abnormal oscillations during rest (rest tremor) that are caused by the degradation of the central nervous system leading to the erratic behavior and death of neurons controlling movement [54, 59, 62]. These syndromes become increasingly prevalent with age, significantly impairing afflicted individuals. Although affecting various parts of the body, these symptomatic tremors are particularly severe in the joints of the hands and fingers.

Individuals afflicted with hand tremors induced by ET and/or PD are severely inhibited in their dexterity and ability to manipulate objects, which are essential to completing everyday tasks (e.g. dental hygiene, writing, eating). Unfortunately, there currently are no cures to halt the progression of ET or PD. However, treatments exist to mitigate the effects of tremor through medication or surgical options. Current treatment options are very expensive, which has pushed researchers to search for alternative means of addressing hand tremors [63]. In recent years, there

has been a rise in the development of inexpensive assistive devices designed to suppress tremors in the hands and fingers. These products include passive devices [64, 65, 66] such as the Readi-Steadi Glove and GyroGlove as well as active devices [67, 68, 69, 70] such as the Emma Bracelet. These wearable devices however, have a few drawbacks in their design. The passive systems add inertia to the hand which limits maneuverability and do not sufficiently address tremors in the finger joints. Meanwhile, the active devices are typically bulky, conspicuous, and rigid, inhibiting mobility and drawing unneeded attention to users.
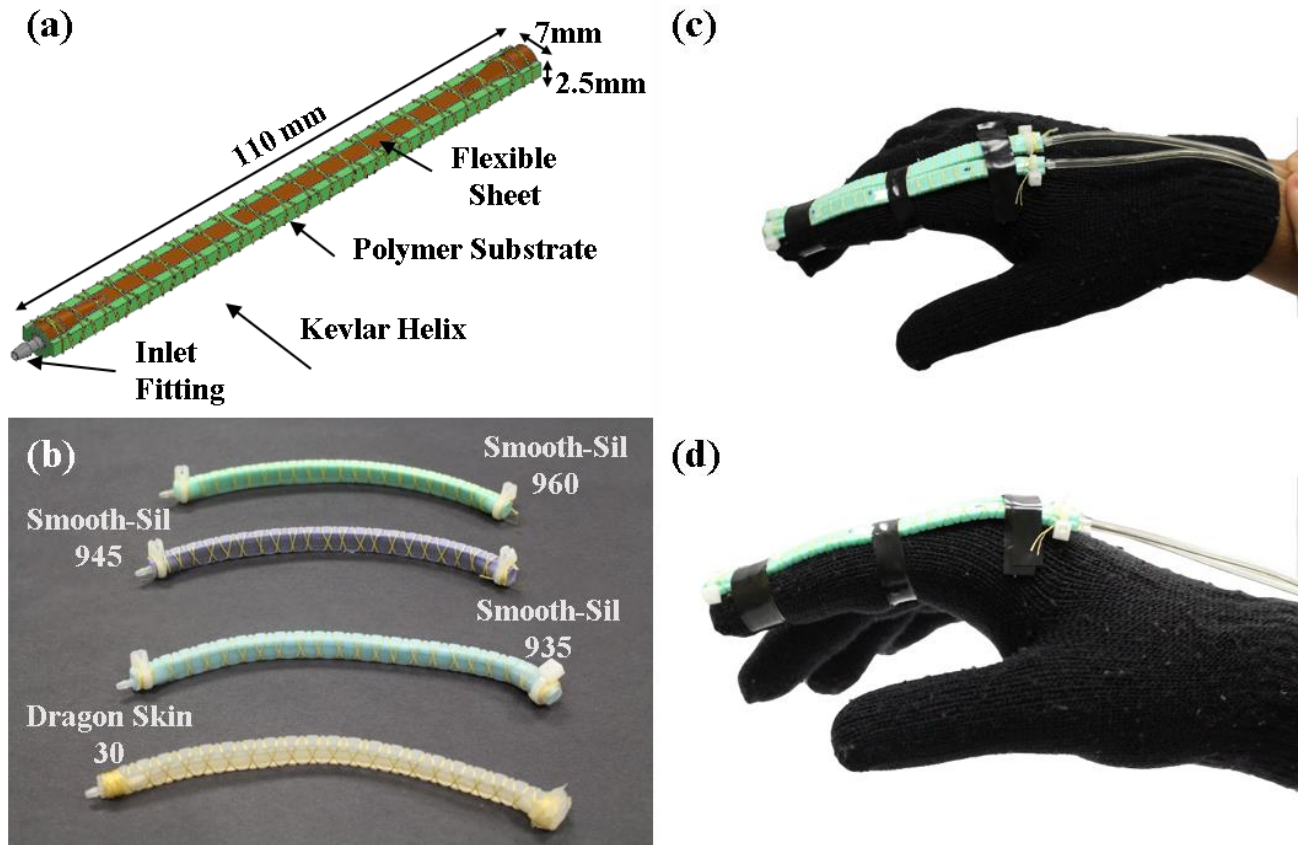
Figure 4.1: (**a**) Solid model of complete FPAM with labels designating key components, (**b**) Fabricated fiber-reinforced FPAMs composed of Smooth-Sil 960 (green), Smooth-Sil 945 (purple), Smooth-Sil 935 (blue), and Dragon Skin 30 (transparent). (**c**) Top view of potential actuator-glove configuration on human hand, **d.**) Side view of potential actuator-glove configuration on human hand.

In order to address these shortcomings, this study focuses on the development of a flat pneumatic artificial muscle (FPAM) capable of providing active suppression of tremors, while remaining lightweight, compliant, and inconspicuous. The FPAM, which was integrated into a

form-fitting single-finger prototype glove, was experimentally characterized and tested for its feasibility and effectiveness in suppressing tremors associated with ET and PD.

4.2 Design & Fabrication

A fiber-reinforced FPAM, shown in Figure 4.1, was designed with inspiration from soft pneumatic actuators previously developed by Wirekoh & Park et al. [31, 51, 71], Bishop-Moser et al. [20, 19], and Polygerinos et al [29, 21]. The FPAM was composed of a thin elastomeric core section, containing a zero-volume air chamber (collapsed air chamber), which was fabricated from a water-soluble mask (Water Soluble Stabilizer, Paper Solvy) and various silicone rubbers from Smooth On Inc., including Dragon Skin 30 (E_{100} = 0.593 MPa), Smooth-Sil 935 (E_{100} = 1.172 MPa), Smooth-Sil 945 (E_{100} = 1.793 MPa), and Smooth-Sil 960 (E_{100} = 1.931 MPa). Here E_{100} is the tensile modulus of the silicone rubber at 100% strain. The thin rectangular form factor of the core was chosen to allow the FPAM to remain compact in its rest state and during operation. The removal of the water-soluble mask by flushing water through the core several times, allowed for the creation of the collapsed air chamber or ZAC. Following this step, an inlet nozzle and stopper are added to the two ends of the FPAM. Subsequently, a single laser-cut plastic sheet (PEI Ultem, McMaster Carr) was secured to the core section by winding Kevlar fibers at alpha and beta helix angles of 75° (Kevlar 69 thread, McMaster Carr) along the outer surfaces. Figure 4.2 provides additional information regarding fabrication of the proposed FPAM. A high volume fraction of Kevlar fibers was utilized in the completed actuator in order to geometrically constrain the deformed form factor of the actuator when inflated with pressurized air.
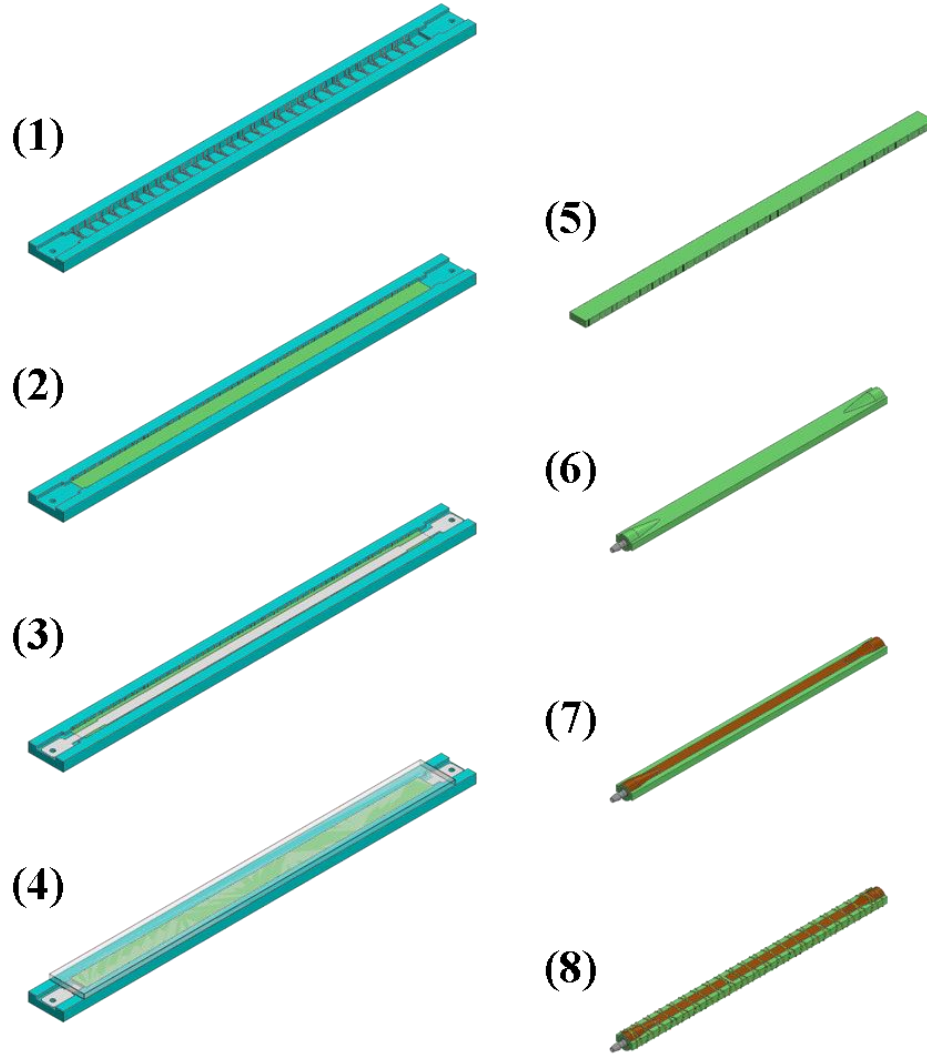
Figure 4.2: Fabrication process of FPAM using water-soluble mask: (**1**) prepare bottom core mold, (**2**) pour liquid elastomer for bottom half of core, (**3**) place water-soluble mask, (**4**) fill top half of mold and place acrylic cap, (**5**) after curing, remove core from mold, and open air volume using water to remove mask, (**6**) cut actuator to length, then insert tube fittings, (**7**) align flexible/inelastic plastic sheet, (**8**) secure the plastic sheet by winding the fibers, followed by cutting the plastic sheet to allow extension at the joints.

In other words, the fibers served to restrict the deformed thickness of the actuator, ensuring the system would remain compact during operation. The plastic sheet provided an additional geometric constraint to the system, which was integral in forcing the actuator to bend when inflated. By attaching the sheet to a single side of the FPAM, the deformed length along that side was constrained to its original length. The opposite side of the actuator however, was free to

elongate along its length. This constraint on the first side coupled with elongation of the opposite

side caused the actuator to bend with increasing pressure input. The actuator was then completed

by utilizing zip-ties to ensure that the tube fittings, plastic sheet, and fibers were firmly secured in

place. The final actuator dimensions of the FPAM were 110 mm × 7 mm × 2.5 mm thick, with

ZAC dimensions of 110 mm × 4 mm × 0.1 mm thick.

4.3 Hyperelastic Bending Model
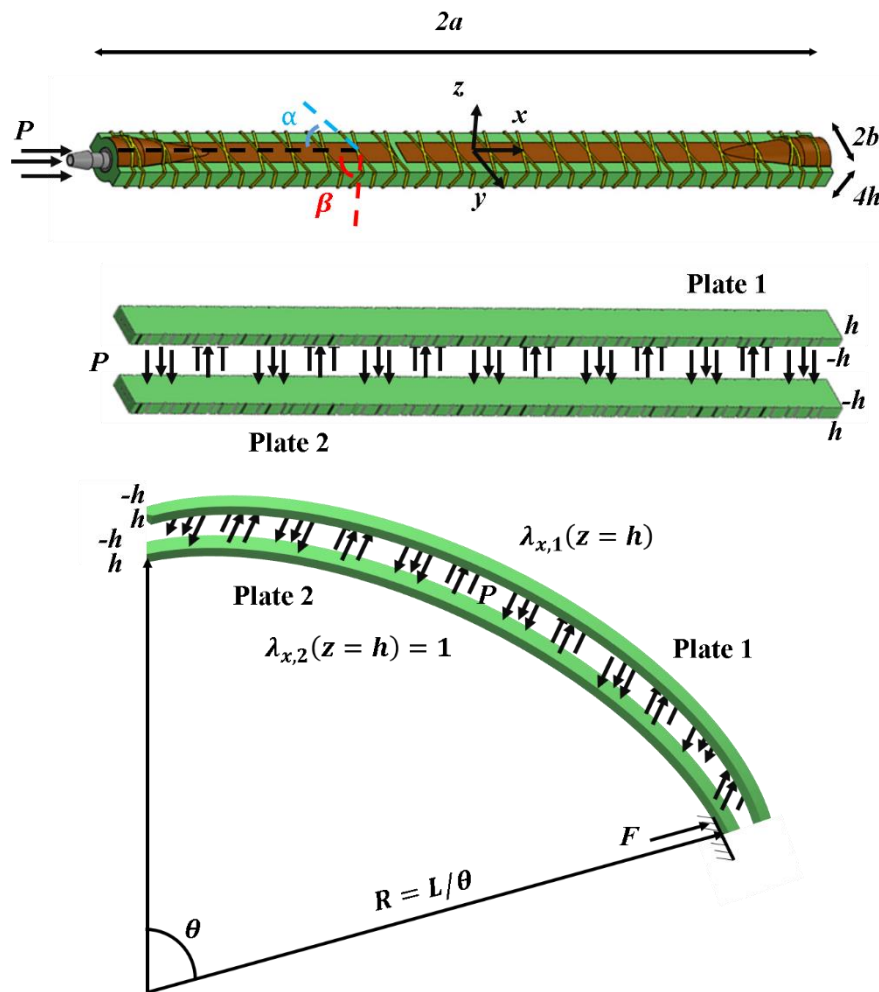
Figure 4.3: Schematic of FPAM depicting coordinate system used to develop the theoretical model.

In order to approximate the behavior of the proposed fiber-reinforced bending FPAM, a

theoretical model was developed. The model incorporates a modified Von Karman formulation

for large deformations [51, 71], utilizing superimposed solutions for simply supported plates and

plates undergoing pure bending. Geometric constraints similar to those imposed in [29, 20, 19, 21] for the design of fiber-reinforced PAMs using helical patterns were also incorporated. Subsequently, the energy method was used to find an analytic solution to the modified von Karman's formulation for the large deformation of plates [32, 33, 34]. The formulation begins with the hyperelastic model developed in [71] in order to approximate the mechanical performance of the FPAM. Assuming an initial z- axis deflection

$$w(x, y) = w_0 \cos \frac{\pi x}{2a} \cos \frac{\pi y}{2b}, \tag{4.1}$$

as postulated by Timoshenko [32, 33], and solving the modified von Karman formulations for a composite plate

$$\frac{1}{E_y} \frac{\delta^4 \phi}{\delta x^4} + \frac{1}{E_x} \frac{\delta^4 \phi}{\delta y^4} + \left(\frac{1}{G_{xy}} - \frac{v_{xy}}{E_x} - \frac{v_{yx}}{E_y} \right) \frac{\delta^4 \phi}{\delta x^4} = \left[\left(\frac{\delta^2 w}{\delta x \delta y} \right)^2 - \frac{\delta^2 w}{\delta x^2} \frac{\delta^2 w}{\delta y^2} \right], \tag{4.2}$$

yielded the following form for the x- and y-axis displacements:

$$u(x, y) = \frac{u_0 x}{2a} + u_1 \sin \left(\frac{\pi x}{a} \right) + u_2 \cos \left(\frac{\pi y}{b} \right) \sin \left(\frac{\pi x}{a} \right), \tag{4.3a}$$

$$v(x, y) = \frac{v_0 y}{2b} + v_1 \sin \left(\frac{\pi y}{b} \right) + v_2 \cos \left(\frac{\pi x}{a} \right) \sin \left(\frac{\pi y}{b} \right). \tag{4.3b}$$

Equations (4.1) and (4.3) provide solutions in the case of pure deformation of the actuator in the plane. In other words, the plates have no z-axis deflection on their edges. In order to model the bending deformation, a bending deflection was devised using a similar form to that postulated by Timoshenko. In this case, where pure bending is being assumed, the z-axis deflection was assumed to take on the form

$$w(x, y) = w_1 \cos \frac{\pi x}{2a}. \tag{4.4}$$

The assumed deflection has no dependence on y, but has z-axis deflection at the maximum x-axis dimensions of the plate ($x=a$). Solving Equation (4.2) using (4) yielded the following x- and y-axis

deflections:

$$u(x,y) = \frac{u_0 x}{2a} + u_1 \sin\left(\frac{\pi x}{a}\right),$$ (4.5a)

$$v(x,y) = \frac{v_0 y}{2b}.$$ (4.5b)

With knowledge that the actuators both bend and deform during operation, a superimposed formulation was used to solve for the deformation of the system. As seen in Figure 4.3, the FPAM was modeled as two flat rectangular composite sheets simply supported along their edges and free to bend with dimensions *2a* x *2b* x *4h*.

The total effects of the deflections of the two plates were specified by combining the displacements of both pure bending and pure deformation such that

$$w(x,y) = w_{deform} + w_{bend},$$ (4.6a)

$$u(x,y) = u_{deform} + u_{bend},$$ (4.6b)

$$v(x,y) = v_{deform} + v_{bend},$$ (4.6c)

$$\lambda_x = \varepsilon_{x,deform} + \varepsilon_{x,bend} + 1,$$ (4.6d)

$$\lambda_y = \varepsilon_{y,deform} + \varepsilon_{y,bend} + 1,$$ (4.6e)

$$\varepsilon_{xy} = \varepsilon_{xy,deform} + \varepsilon_{xy,bend}.$$ (4.6f)

The formulations in Equation 4.6 could then be further specified for each of the plates as,

$$w(x,y) = w_{i0} \cos\frac{\pi x}{2a} \cos\frac{\pi y}{2b} + w_{b,i1} \cos\frac{\pi x}{2a},$$ (4.7a)

$$u(x,y) = \left[\frac{u_{i0} x}{2a} + u_{i1} \sin\left(\frac{\pi x}{a}\right) + u_{i2} \cos\left(\frac{\pi y}{b}\right) \sin\left(\frac{\pi x}{a}\right)\right]$$ (4.7b)

$$+ \left[\frac{u_{b,i0} x}{2a} + u_{b,i1} \sin\left(\frac{\pi x}{a}\right)\right]$$

,

$$v(x,y) = \left[\frac{v_{i0}y}{2b} + v_{i1}\sin\left(\frac{\pi y}{b}\right) + v_{i2}\cos\left(\frac{\pi x}{a}\right)\sin\left(\frac{\pi y}{b}\right)\right] + \left[\frac{v_{b,i0}y}{2b}\right], \tag{4.7c}$$

where i is the index equal to 1 for the top plate or 2 for the bottom plate (Figure 4. 3), and the constants are unknowns to be solved for through the minimization of the system's potential energy. A nonlinear hyperelastic strain energy density, W, with volumetric stretch ratio J, was then incorporated from [71]

$$W_i = \frac{E}{6}\left(\lambda_{xi}^2 + \lambda_{yi}^2 + \lambda_{zi}^2 + \frac{\varepsilon_{xyi}^2}{2} - 3\right), \tag{4.8a}$$

$$J_i = \lambda_{xi}\lambda_{yi}\lambda_{zi} - \frac{\varepsilon_{xyi}^2}{4}\lambda_{zi} \tag{4.8b}$$

for an incompressible Neo-Hookean solid. The normal stretches λ_x in the x-axis direction, λ_y in the y-axis direction, and shear strain ε_{xy} were then defined as,

$$\lambda_{xi} = \left[\frac{\delta u_i}{\delta x} + \frac{1}{2}\left(\frac{\delta w_i}{\delta x}\right)^2 - z\frac{\delta^2 w_i}{\delta x^2}\right] + \left[\frac{\delta u_{b,i}}{\delta x} + \frac{1}{2}\left(\frac{\delta w_{b,i}}{\delta x}\right)^2 - (z+h)\frac{\delta^2 w_{bi}}{\delta x^2}\right] + 1, \tag{4.9a}$$

$$\lambda_{yi} = \left[\frac{\delta v_i}{\delta y} + \frac{1}{2}\left(\frac{\delta w_i}{\delta y}\right)^2 - z\frac{\delta^2 w_i}{\delta y^2}\right] + \left[\frac{\delta v_{b,i}}{\delta y} + \frac{1}{2}\left(\frac{\delta w_{b,i}}{\delta y}\right)^2 - (z+h)\frac{\delta^2 w_{bi}}{\delta y^2}\right] + 1, \tag{4.9b}$$

$$\varepsilon_{xyi} = \left[\frac{\delta u_i}{\delta y} + \frac{\delta v_i}{\delta y} + \frac{\delta w_i}{\delta x}\frac{\delta w_i}{\delta y} - 2z\frac{\delta^2 w_i}{\delta x\delta y}\right] \tag{4.9c}$$

$$- \left[\frac{\delta u_{b,i}}{\delta y} + \frac{\delta v_{b,i}}{\delta y} + \frac{\delta w_{b,i}}{\delta x}\frac{\delta w_{b,i}}{\delta y} - 2(z+h)\frac{\delta^2 w_{bi}}{\delta x\delta y}\right],$$

where w, u, and v are displacement formulations due to pure deformation and w_b, u_b, and v_b are the displacement formulations for pure bending. The bending strains through the thickness of the plates were defined with this form to account for the fact that the two plates must maintain contact at their edges during bending. This edge constraint manifests in the following boundary constraints:

$$w_{21} = -w_{11} \tag{4.10a}$$

(due to coordinate system of plates),

$$u_{20} = u_{10}, \tag{4.10b}$$

$$v_{20} = v_{10}, \tag{4.10c}$$

$$u_{b,20} = u_{b,10}, \tag{4.10d}$$

$$v_{b,20} = v_{b,10}. \tag{4.10e}$$

In addition, two geometric constraints were defined. First, the actuator had to maintain a constant length at $z_2 = h$ due to the location and properties of the plastic sheet. This constraint was formulated using an average stretch

$$1 = \frac{1}{2a * 2b} \int_{-b}^{b} \int_{-a}^{a} \lambda_{x2}(z = -h) dx dy. \tag{4.10f}$$

Secondly, a geometric constraint associated with the fiber windings was incorporated as in [21-24] at $z=h$ for both plates. This constraint was given as

$$\frac{w + \lambda_{yi} 2b}{w + 2b} = \frac{sgn(\beta)\sqrt{1 - \cos(\beta)^2 \lambda_{xi}^2} \cos(\alpha) - sgn(\alpha)\sqrt{1 - \cos(\alpha)^2 \lambda_{xi}^2} \cos(\beta)}{\sin(\alpha - B)}, \tag{4.10g}$$

where w is the distance the fibers wrap around the undeformed sections of the actuator per loop. The incompressibility of the plates resulted in a volumetric constraint caused by the deformation component of the plates' deflection which was defined as

$$v_{i0} = -\frac{2u_{i0}b}{(2a + u_{i0})}. \tag{4.10h}$$

Finally, a constraint was placed on the maximum x-axis and y-axis deflection such that the deformed actuator configuration was realistic. This constraint was defined such that the ends of the actuators would come into contact at a bending angle of 360° and bending would have negligible effects on strain in the y-axis direction as,

$$u_{b,i0} = -\frac{\theta}{\pi}a, \qquad\qquad\qquad (4.10\text{i})$$

$$v_{b,i0} = 0. \qquad\qquad\qquad (4.10\text{j})$$

Utilizing the constraints 4.10(a)-(j), the potential energy of the system could then be defined as

$$\Pi = \iiint W_1 dV_1 + \iiint W_2 dV_2 - W_{P1} - W_{P2} - W_m \qquad\qquad (4.11)$$

,

where $\iiint W_i dV_i$ is the strain energy of each plate, $W_{Pi} = \iint P\left[w_{i0}\cos\frac{\pi x}{2a}\cos\frac{\pi y}{2b} + w_{b,i1}\cos\frac{\pi x}{2a}\right] dxdy$ is the work done by pressure to deform the plates, and $W_m = M\theta$ is the work done by the acting moment, with the maximum moment being defined as $M_{max} = 2a * F$. Π was then minimized with respect to the unknowns u_{11}, u_{12}, v_{11}, v_{12}, u_{21}, u_{22}, v_{21}, v_{22}, $w_{b,11}$ and θ (i.e. $\frac{\delta\Pi}{\delta\theta} = 0$) to establish a relationship between the required input pressure, P, and the desired bending angle θ. The theoretical model developed was then fit to the experimental.

4.4 Experimental Characterization

The fiber-reinforced bending FPAMs were subjected to various experiments in order to characterize their mechanical performance. The experimental apparatus employed (Figure 4.4) was composed of four proportional solenoid valves (MDPRO5VCF8S 11.5 VDC, Parker), two industrial pressure sensors capable of reading up to 150 psi (BangGood), an Arduino Uno microcontroller (Arduino), a force sensor capable of reading up to 10N (FSAGPDXX001RCAB5, Honeywell), a custom microfluidic soft sensor designed to measure bending angle of the actuators, and custom electronics designed to effectively power the system.
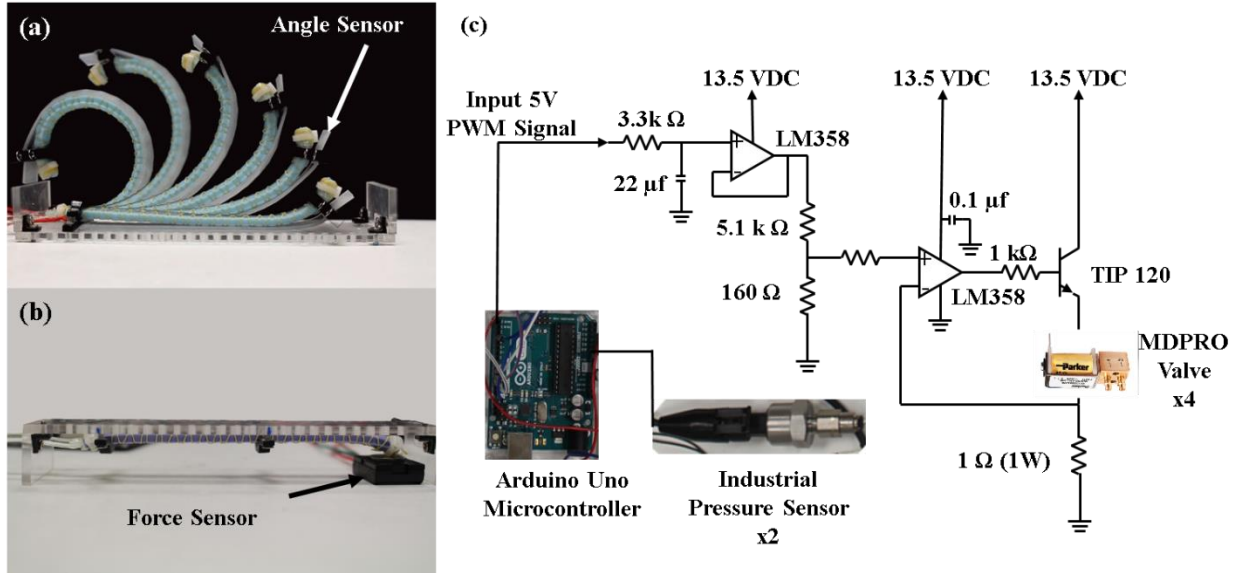
Figure 4.4: Diagram of experimental apparatus used to characterize the prototype fiber-reinforced FPAMs. (**a**) Overlay of the bending deformation of an FPAM during angle characterization experiments. (**b**) FPAM positioning during force control experimentation. (**c**) Schematic of electronic components utilized throughout experimentation

Several tests were conducted to establish how the FPAMs behaved during operation. Initially, the FPAMs' maximum bending angle at various input pressures was examined. During this procedure, the FPAMs were secured to a flat surface, then pressurized with compressed air, as seen in Figure 4.4(a). The actuators were inflated up to a maximum angular deflection of 270° (physical limitation of experimental setup) where possible. The angular deformation was captured by the soft angle sensor and recorded using the Arduino microcontroller.

In the next procedure, the dynamic properties of the FPAMs were examined. The actuators were again fixed to a flat surface at one end. The actuators were then cycled from 0 to their maximum experienced pressure during the angle experiments. This experiment was used to dynamically characterize the activation time, deactivation time, and bandwidth of the actuators. Cycles occurred at frequencies of 0.25-12 Hz, which are frequencies at or below those typically seen in individuals experiencing pathological hand tremor.

Subsequently, experiments were conducted to measure the maximum tip force generated by the FPAMs at input pressure. During this procedure, the actuators were fixed against a flat

surface at three points as seen in Figure 4.4(b). The actuators were then pressurized using the same pressure ranges used for the bending experiments. Weights were used to ensure contact was maintained between the tip of the actuators and the force sensor during experimentation. In the final procedure the FPAMs were secured, in antagonistic pairs, to the index finger of a human hand at rest, in order to evaluate the potential of the actuators to suppress hand tremors. The actuators were subjected to an open loop control algorithm designed to simulate the maximum amplitude and frequencies associated with tremor. The goal was to assess the feasibility of the actuators to generate oscillatory motions and forces that would be required to suppress acting tremor in real life situations.

4.5 Results & Discussion
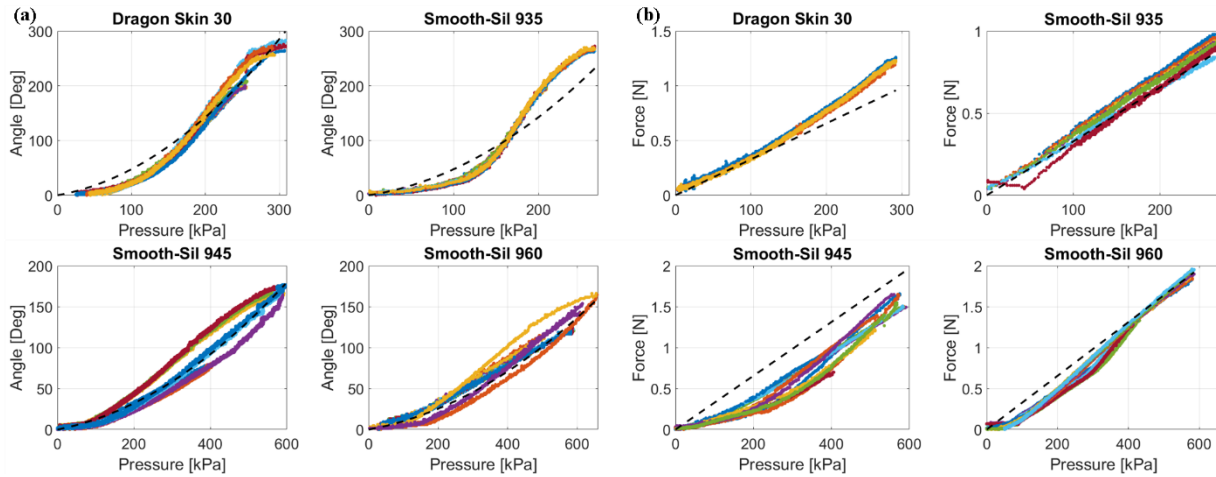
Figure 4.5: Mechanical performance of the four fiber-reinforced FPAMs fabricated. (**a**) Maximum experimental bending angle measured during experimentation. (**b**) Maximum generated bending tip force measured at zero angle deflection.

The four fiber-reinforced FPAMs developed in this study, which were composed of Dragon Skin 30, Smooth-Sil 935, Smooth-Sil 945, and Smooth-Sil 960, were experimentally characterized to determine their maximum bending tip force and bending angle when pressurized. These values were then used to determine effective hyperelastic moduli to be used for fitting the theoretical model to the actuators' mechanical performance. The effective moduli can be found in

table 1. In addition, the maximum bending angles and generated forces can be found in Figure

4.5(a)-(b) respectively, with additional results found in Table 4.1.

Table 4.1: Performance and Theoretical Comparison of FPAMs

Material	Effective Modulus (MPa)	Max Angle (Deg)	Max Force (N)	Theoretical Angle RMSE (Deg)	Theoretical Force RMSE (N)
Dragon Skin 30	3.558	282.9±1	1.26±.05	20.2	0.066
Smooth-Sil 935	3.310	272.3±1.5	.98±.12	26.15	0.055
Smooth-Sil 945	9.308	176.7±2.4	1.65±.22	10.36	0.324
Smooth-Sil 960	10.963	164.6±4.1	1.96±.06	6.43	0.179

As seen in Figure 4.5 and table 4.1, the actuators are able to reach maximum bending angles

far larger than the required 40° range associated with ET and PD. The actuators composed of

Smooth-Sil 945 (SS-945) and Smooth-Sil 960 (SS-960) reached bending angles of 176.7±2.4° and

164.6±4.1° respectively, while those composed of Dragon Skin 30 (DS-30) and Smooth-Sil 935

(SS-935) reached bending angles of 282.9±1° and 272.3±1.5° respectively. The former 2 actuators

could further reach larger bending angles, if not for the constraint of the experimental setup which

limited the maximum deflection of the actuators. In addition, the FPAM's fabricated from DS-30,

SS-935, SS-94, and SS-960, generated maximum overall forces of 1.26±0.05 N, 0.98±0.12 N,

1.65±0.22 N, and 1.96±0.06 N respectively. During experimentation the actuators were found to

fail above 345 kPa for DS-30 and SS-935 and above 655 kPa for SS-945 and SS-960. Typically

these failures were due to the wound fibers shearing through the actuators at the corners or were

pinhole failures occurring around the inlet fittings due to the material being stretched to

accommodate the cylindrical tube fittings.
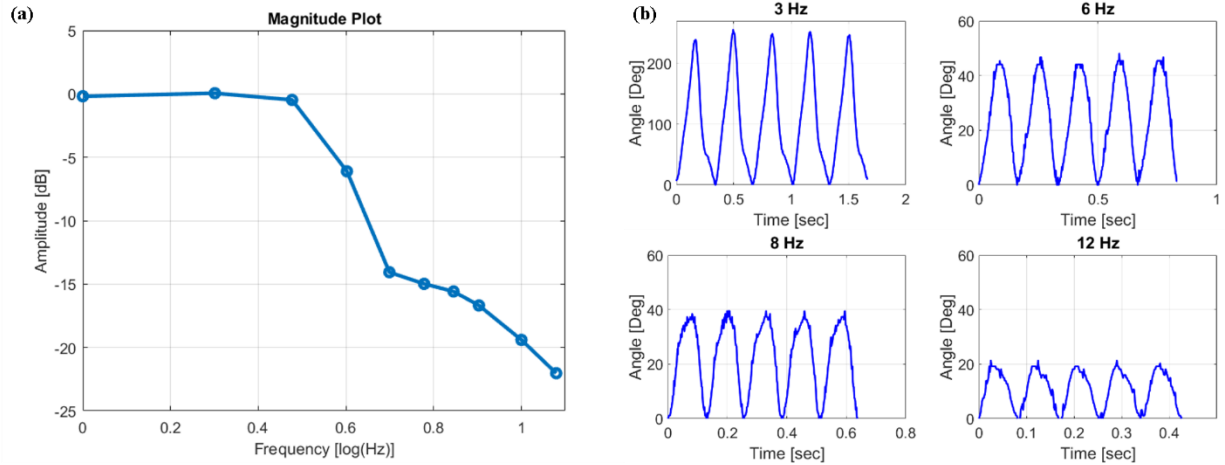
Figure 4.6: Dynamic performance of prototype FPAMs. (**a**) Magnitude response of actuators at frequencies up to 12 Hz. (**b**) Examples of the dynamic response of the actuators at various frequencies. Maximum amplitude of 270° for DS- 30 & SS-935 and maximum amplitude of 180° for SS-945 and SS-960.

The developed theoretical model compares favorably to the mechanical performance of the fiber-reinforced FPAMs measured experimentally. The theoretical model has an average root-mean squared error (RMSE) of 15.8±9° and 0.16±.13 N for its approximation of the bending angle and tip for of the developed actuators. When compared to the maximum overall performance of the actuators, this amounts to an RMSE ratio of 6.7±2% and 9.9±7% for the force and bending angle respectively. This error can partially be attributed to the SS-935 material, which behaves particularly differently than the other silicone rubbers utilized in this study. In addition, poor sealing of the actuators led to air leakage at higher pressure inputs. However, due to model's ability to approximate the trajectory and performance of the FPAM's, researchers should be able to utilize it to predict the performance for future designs.

Examples of the dynamic performance of the actuators are shown in Figure 4.6. The actuators had activation times of 0.159±0.005 seconds and deactivation times of 0.278±0.023 seconds. These times were evaluated as the time required to reach the maximum angular deformation, which was about 180° for the stiffer materials, and 270° for the lighter materials. This results in an average activation and deactivation speed of 1415°/s (40° displacement at 35.4 Hz) and 820°/s (40° at 20.2 Hz) respectively, which is sufficient to address the range and amplitude

of hand tremors. Additionally, the bandwidth of the actuators was calculated as 4 Hz based on the traditional definition of the 3 dB cutoff for maximum amplitude reduction. However, for this specific application, the bandwidth was calculated as the frequency at which the actuators could not reach 40° displacement, (the maximum joint deflection associated with PD and ET), which was around 8 Hz.
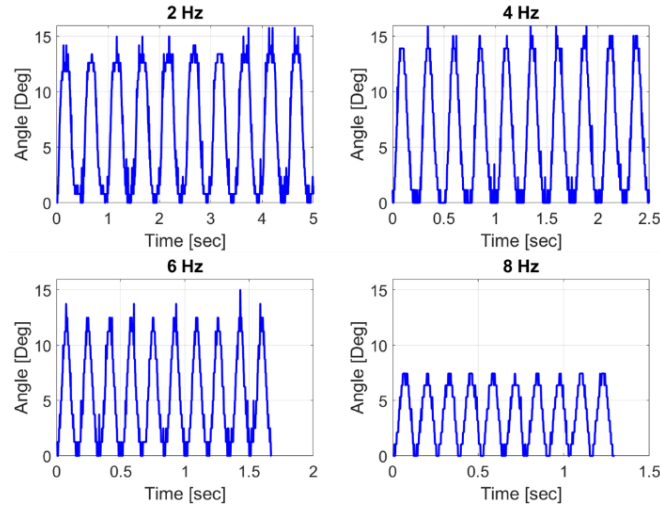
Figure 4.7 Real life bending angle displacement during dynamic experimentation on a human index finger.

The ability of the actuators to produce oscillatory movements on a human finger in vivo, was demonstrated and can be found in Figure 4.7. Although the FPAMs could produce large angular displacements at frequencies between 4 and 8 Hz when unloaded, the added stiffness of the finger significantly reduced the overall displacement of the actuators. When attached to a human finger, the FPAMs were able to generate oscillatory behavior of at a maximum of 7.5° at frequencies up to 8 Hz. However, this range of motion is still significant, and when coupled with the stiffness of the actuators, should be able to significantly reduce the effects of hand tremor along the finger.

4.6 Conclusion

A fiber-reinforced bending flat pneumatic artificial muscle was designed and fabricated to suppress hand tremors including essential tremor and tremors associated with Parkinson's disease. The mechanical performance of the prototyped FPAM was experimentally characterized through both static and dynamic tests with actuators manufactured from a variety of silicone rubbers. In addition, a theoretical model was developed to approximate the bending angle and force generation of the actuator at input pressure and showed close approximation when compared to experimental characterization of the actuator. Ultimately, the actuators were capable of acting in the required frequency range of 4-12 Hz on an actual human finger. However, this is only a first step, and additional improvements should be made in order to more effectively address hand tremors.

Further considerations for future work include the improvement of actuator performance in two key areas. Firstly, the actuators should be fabricated with elliptical edges to minimize the occurrence of failure due to the fibers shearing through the material along the corners of the actuators. Secondly, the bending force generated by the actuators should be improved through a redesign and/or material selection in order to allow greater displacement of the finger at high frequencies. One potential redesign is by fabricating the antagonistic actuator pair as a stacked singular actuator instead. In this way, angular bending and extension can be combined into a single actuator that fits over the back of the finger with the capability to produce larger bending moments due to the increased width of the air volume. In addition, custom tube fittings should be designed to better fit the form factor of the FPAMs. Subsequently, a full glove system should be designed to better house the actuators and provide improved transmission of the actuator force to the fingers during operation.

Acknowledgements

5 Soft Miniaturized Actuation and Sensing Unit for Cardiac Ablation Procedures

Abstract

Recently, researchers have actively sought to improve the efficacy of treatments for atrial fibrillation through the augmentation of catheter systems. These augmentations have included integrated force sensing and external actuation of the overall catheter. However, limited research has been aimed at providing autonomous force control at the site of treatment through the integration of sensing and actuation at the tip of the catheter, which can significantly enhance the success rates of such procedures. This study provides a solution to this demanding challenge by miniaturizing the actuation and sensing components and integrating them into a flexible functional catheter tip. Fabrication strategies are presented for a series of novel soft thick-walled cylindrical actuators with embedded sensing. These actuators have diameters within the range of 2.6-3.6 mm, and can both sense and generate forces in the range of 0-0.4 N (required for the application), with a bandwidth of 1-2 Hz. A hyperelastic deformation model for soft thick-walled cylinders with fiber-reinforcements was developed. Furthermore, an experimental setup was developed for the conduction of static and dynamic characterization tests, which allowed for comparison with the theoretical model. Overall, experimental results demonstrated that the prototype units were able to meet the required design specifications for the treatment of atrial fibrillation through a cardiac ablation procedure.

Keywords: Medical Robotics, soft robotics, atrial fibrillation, fiber-reinforced, PAM, pneumatic artificial muscle.

5.1 Introduction

Soft robotic technology is finding increased visibility in biomedical applications [72] due to the inherent compliance and safety of soft medical devices during intimate interaction with human tissues. Although soft robotic technology has become increasingly prominent in the design of rehabilitative and prosthetic devices [73, 74, 75, 76], difficulty in the miniaturization of soft actuation and sensing has been a limiting factor in the design of integrated compact systems for applications in minimally invasive surgery (MIS) [77, 78, 79, 80]. Minimally invasive surgical treatments [81] are characterized by keyhole surgeries in which a system equipped with a functional tip is inserted through a small incision in the body. Due to the nature of MIS operations, patients experience shorter recovery times and higher success rates [82, 83]. Most MIS procedures are performed for diagnostic purposes, through localized biopsies, or for the localized destruction of abnormal cells, such as in the case of cardiac ablation.

Cardiac ablation [84], which involves localized destruction of abnormal heart tissues, is one of the most-performed MIS procedures with 30,000-35000 being conducted annually for the treatment of atrial fibrillation (AF). Radio frequency ablation (RFA) is one of the main techniques utilized for such cardiac ablation procedures. The traditional medical device for RFA consists of a flexible sheath into which a catheter equipped with a functional tip is inserted. This functional tip, when in contact with heart tissue, destroys the abnormal cells by a transfer of energy through a system of electrodes. The traditional surgical workflow for cardiac ablation begins with the insertion of the sheath through a vein in the groin. The sheath is then moved to the heart. The catheter equipped with its functional tip is then inserted into the sheath, which serves as a guide. The physician steers the catheter along the sheath until it makes contact with the abnormal heart tissue. Subsequently, the physician manually manipulates the position of the catheter tip and

indirectly controls the contact forces between tip and heart tissues by applying force at the proximal end of the catheter. The required amount of energy and the lesion size, in the case of RFA, is determined by the interaction of the contact forces between the tip and the tissue [85]. Unfortunately, manual control of the catheter tip results in large variations in applied force [86, 87], and in some cases complications, such as perforation, arise due to the application of excessive force [88].

Researches have attempted to alleviate this issue through the integration of force sensors in preexisting catheter tips [89, 90]. However, these systems do not provide haptic feedback to the physician, instead relying solely on visual display of the measured contact force, which may not be sufficient to avoid complications due to variations in manual response and reaction time between physicians. Recent studies have sought to provide automatic force control of the catheter tip by externally controlling the catheter handle [91, 92]. With this strategy, however the modeling of the system becomes increasingly complex due to the presence of friction caused by random contacts between the sheath and catheter, and viscous forces caused by the motion between the catheter and the sheath in vivo. In addition, in this workflow, the physician does not retain control over the catheter inside the sheath and the overall procedure. Commercially available catheter sheaths, designed to provide navigation for the catheters to the site of treatment, restrict the external diameter of ablation catheters to 2-5 mm, which makes the integration of actuation and sensing challenging at the catheter tip. Moreover, the catheter tip has to be able to bend and traverse the flexible sheath, which takes the shapes of the veins into which it is inserted.

In order to overcome these limitations, a miniaturized flexible functional catheter tip containing integrated actuation and sensing was designed. The miniaturized catheter tip is

composed of a soft force sensor and a soft fiber-reinforced hydraulic thick-walled cylindrical actuator, which could be embedded at the tip of conventional catheters.

In order to approximate the behavior of the prototype catheter tips, previous research regarding the modeling of both thin-walled cylindrical shells and fiber-reinforced actuators [19, 21, 93] was examined due to the lack of current theory on the modeling of fiber-reinforced thick-walled cylindrical actuators. However, the usual assumptions made for thin-walled cylinders, such as vanishing stress through the radial thickness, do not hold in the case of thick-walled cylinders. In addition, analytic models for thick-walled cylindrical shells established by developing differential equations for the equilibrium condition involving stresses in different directions [94, 95] do not hold when fiber-reinforcement of thick-walled cylindrical shells is considered, which will be further detailed in this study. As such, an exact analytic model for fiber-reinforced thick-walled cylindrical shells was developed.

In order to address these issues, this study includes the design, modeling and experimental evaluation of a miniaturized soft sensing and actuation unit designed to meet the requirements of cardiac ablation procedures. Fabrication of the soft thick-walled cylindrical actuators with embedded soft sensing elements is described. In addition, an exact analytical hyperelastic model for the deformation of fiber-reinforced thick-walled cylindrical actuators is detailed. An experimental setup was developed specially to use hydraulic actuation rather than pneumatics, which more common for soft actuators, to ensure safety in the case of accidental leaks during the procedural application in vivo (saline solution is typically used for hydraulic actuation in medical applications for safety reasons). Through this experimental apparatus, static and dynamic characterization of both the soft sensing and soft actuation elements was conducted to ensure they adhere to the required specifications for the application. The main advantage of this approach lies

in the ability to do in situ actuation of the catheter tip, as opposed to external actuation, which makes the system modeling and force control more transparent. Moreover, such a design keeps the manual control of the catheter in the hands of the physician, which is desirable for safety.

5.2 Design and fabrication

5.2.1 System Requirement Specifications

This subsection details the specifications for the mechanical design, static, and dynamic performance of the developed miniaturized sensing and actuation unit which are derived from the cardiac ablation procedures intended for treatment of AF.

1.) Size: AF treatment begins with placing the catheter sheath inside the blood vessel through which a catheter is later inserted. The size of the blood vessels determines the diameter of the catheter sheaths and in turn of the catheters used for the treatment, which ranges from 6-15 Fr (2-5 mm).

2.) Actuation: Apart from the constraints on the size, the miniaturized actuation must be able to apply a force in the range of 0-0.4 N [87], which is observed during diverse catheter ablation procedures for AF treatment. Since the catheter tip should remain in contact with the heart wall during the procedure, limits on the linear displacement and the linear speed of the actuator should be enough to compensate for the heart wall movement (1–2 mm at 1-2 Hz) due to the beating of the heart and expansion/contractions of the lungs during breathing [96].

3.) Force Sensing: At least one° of freedom (DOF) in the force sensing is required to measure the interaction force between the tip and heart tissue. The force sensor should be able to measure force within the range 0-0.4 N with a resolution of 0.01 N, which the range required for actuation. Moreover, it should have a bandwidth within 1-2 Hz.

5.2.2 Design of Miniaturized Actuation and Sensing Unit
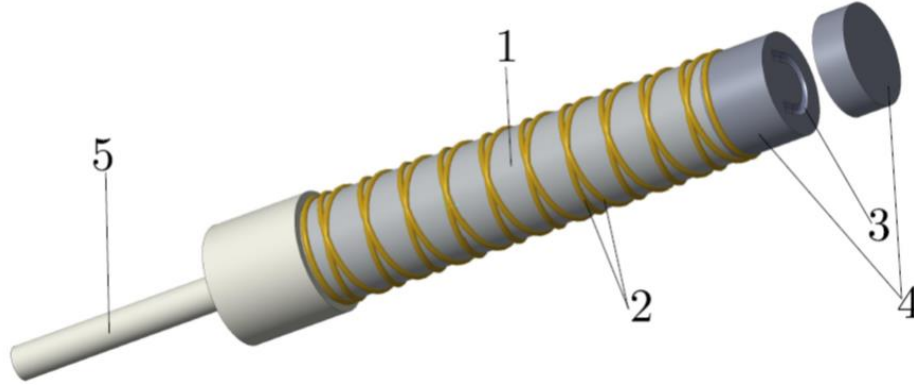
Figure 5.1: Conceptual design of miniaturized soft actuation and sensing unit: (**1**) thick cylindrical shell, (**2**) two sets of wound fibers in opposite directions, (**3**) representative microchannel, (**4**) soft sensing elements, (**5**) pressure inlet tube.

A functional catheter tip, as shown in Figure 5.1, was designed and fabricated to satisfy the system requirements for the treatment of AF through a catheter ablation procedure. More specifically, the prototype device incorporated two major systems, a soft hydraulic actuator and a soft pressure sensor. In order to ensure a compact, compliant, and effective design, soft materials were utilized to produce the embedded actuation and sensing components of the functional catheter tip. The soft actuator was composed of a deformable thick-walled cylindrical shell, composed of silicone rubber (Dragon Skin 30 or Smooth-Sil 935, Smooth-On Inc.), which was geometrically constrained by a double helix of inextensible fibers (Kevlar 69 Thread, McMaster Carr). The two sets of fibers were wrapped at helix angles, $\alpha = 75°$ and $\beta = 75°$. During pressurization with saline solution, chosen for safety reasons, the soft actuator deformed radially and axially. Here, the constraint induced by the fiber-reinforcements played a particularly important role, by minimizing unwanted deformation in the radial direction. This decreased the occurrence of bending due to imperfections in fabrication, while producing repeatable linear displacements in the axial direction of the actuator. The soft pressure sensor was composed of a solid cylindrical

77

section, made from a softer material (Dragon Skin 10, Smooth-On Inc.), which contained embedded microchannels filled with liquid (eGaIn, Alfa Aesar) for resistive sensing. Forces applied to this section cause the microchannels to deform, which in turn caused an increase in the sensor's resistance.
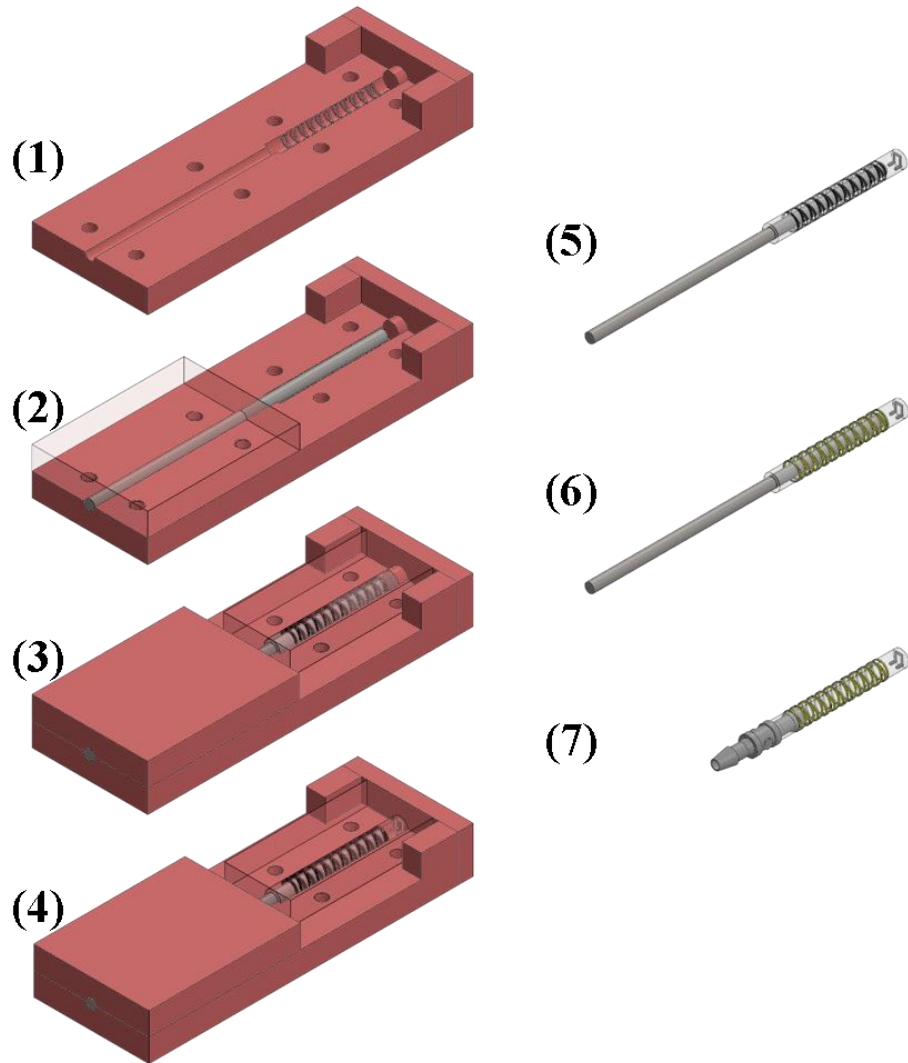
Figure 5.2: Fabrication process of fiber-reinforced functional catheter tip: (**1**) prepare bottom core mold and front cap section with extruded cylinder, (**2**) place steel rod used to make inner diameter of catheter, (**3**) fill mold with uncured material, then place on top mold section, (**4**) replace front cap with cap containing negative of microchannels, (**5**) remove cured core from mold and fill microchannels with eGaIn, (**6**) wind Kevlar thread in double helix around core, (**7**) replace rod with inlet connector to seal section and add wires to the sensor.

The actuation section has a length of L=15 mm and an internal radius of A=0.8 mm for all the prototypes. Prototypes with two external radii of B=1.3 and 1.8 mm were produced. The sensor section had a length of 2.75 mm and an external diameter of 2.6 mm or 3.6 mm, respectively for actuator prototypes with external radii of B=1.3 mm or 1.8 mm.

5.2.3 Fabrication

The soft catheter tip was fabricated in a multi-step process, as shown in Figure 5.2, using customized 3D printed molds (Objet 30, Stratasys) and liquid-cure silicone rubbers. First, the actuation section was fabricated using either Dragon Skin 30 (E_a = 0.614 MPa) or Smooth-Sil 935 (E_a = 1.173 MPa). A stainless steel rod, 1.6 mm in diameter, was aligned in the mold which contained extrusions to demarcate where the fibers should be wound. Next, the silicone rubber was poured into the mold and sealed with an endcap containing an extruded cylinder, to cordon off a section for the sensor. The material was then allowed to cure. After curing, the end cap was removed. Subsequently, Dragon Skin 10 (E_s = 0.151 MPa), a softer silicone rubber, was mixed and poured into the mold to fill the previously blocked section. Next, a second end cap, containing the negative of the microchannel layout was placed. Following this second curing process, the microchannels were sealed and filled with eGaIn. Next, fibers were wound around the completed actuator section and tied in place. 38-gauge copper magnet wire was then inserted into the reservoir section of the microchannels. Finally, tubing and the connectors were placed and bonded to the soft actuator using Dragon Skin 10 to complete the functional catheter tip. Four representative prototypes of the actuation section were fabricated with different sizes and materials, as shown in Figure 5.3.
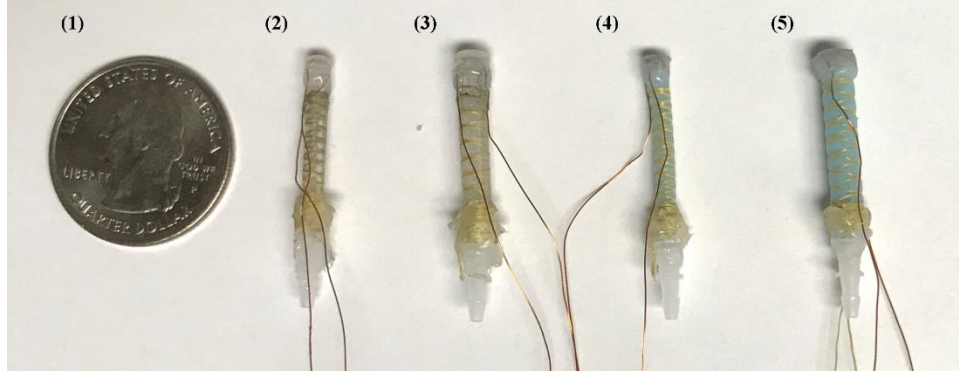
Figure 5.3: From left to right: (**1**) US quarter dollar coin, (**2**) prototype with Dragon Skin 30 E_a=0.614 MPa, with external radius of B=1.3 mm, (**3**) prototype with Dragon Skin 30 E_a= 0.614 MPa, with external radius of B= 1.8 mm, (**4**) prototype with Smooth-Sil 935 E_a=1.173 MPa, with external radius of B=1.3 mm, (**5**) prototype with Smooth-Sil 935 E_a=1.173 MPa, with external radius of B=1.8 mm.

5.3 Hyperelastic Fiber-Reinforced Thick-Walled Cylinder Model

The design concept, shown in Figure 5.1, consisted of a soft deformable fiber-reinforced thick-walled cylindrical shell, which is closed at one end and fabricated from hyperelastic materials. Upon application of fluidic pressure, the element deformed both radially and axially. The controlled axial deformation however, was the more important mode in this study. In addition, microchannels filled with eGaIn were embedded in the closed end to allow for force sensing. This section details the parametrization and theoretical these soft sensing and actuation elements.
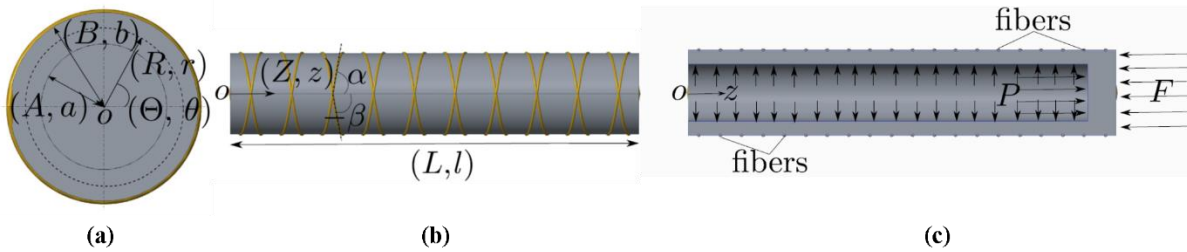
Figure 5.4: Chosen cylindrical coordinates and parametrization: (**a**) top view, (**b**) side view, (**c**) sectioned view of the actuator: equilibrium under action of external force F and internal pressure P.

In this subsection, the exact analytical model for fiber-reinforced thick-walled cylindrical actuators is developed. For thin-walled assumptions to hold, the ratio of the cylinder's radius to its thickness must be greater than 10. Due to the size requirements, practical design, and prototyping considerations associated with cardiac ablation procedures, the actuators considered in this study

fell under the category of thick walled cylindrical shells.

Figure 5.4(a),(b) shows the parametrization of these fiber-reinforced thick-walled cylindrical actuators. Given the geometry of the actuators, a cylindrical coordinate system was used. Modeling techniques utilized in [94] were adopted, so as to easily compare results. Nonetheless, for completeness a brief description is given here and the full details can be found in [94]. R, Θ, and Z are the cylindrical coordinates for the rest configuration represented by Equation (5.1a), whereas r, θ, and z are the cylindrical coordinates for the deformed configuration represented by Equation (5.1b).

$$A \leq R \leq B \qquad\qquad 0 \leq \Theta \leq 2\pi \qquad\qquad 0 \leq Z \leq L \qquad\qquad (5.1a)$$

$$a \leq r \leq b \qquad\qquad 0 \leq \theta \leq 2\pi \qquad\qquad 0 \leq z \leq l \qquad\qquad (5.1b)$$

Let λ_1, λ_2, and λ_3 be the principal stretches as defined in Equation (5.2a). The material was assumed to be an incompressible Neo-Hookean solid with the volumetric stretch ratio relationship $\lambda_1 \lambda_2 \lambda_3 = 1$ holds. Let $W \equiv W(\lambda_1, \lambda_2, \lambda_3)$ be the strain energy density function per unit volume, which can be expressed after eliminating λ_3 as $\widehat{W} \equiv \widehat{W}(\lambda_1, \lambda_2, \lambda_1^{-1}\lambda_2^{-1})$. Let σ_{11}, σ_{22}, and σ_{33} be the principal components of the Cauchy stress tensor σ as defined in Equation (2b). Also, let $\lambda_a = \frac{a}{A}$, $\lambda_b = \frac{b}{B}$ and P to be the internal inflation pressure.

$$\lambda_1 = \frac{r}{R} = \lambda \qquad\qquad \lambda_2 = \lambda_z = \lambda_l = \frac{l}{L} \qquad\qquad \lambda_3 = (\lambda_1 \lambda_2)^{-1} \qquad (5.2a)$$

$$\sigma_{11} - \sigma_{33} = \lambda \frac{\partial \widehat{W}}{\partial \lambda} \qquad\qquad\qquad \sigma_{22} - \sigma_{33} = \lambda_1 \frac{\partial \widehat{W}}{\partial \lambda_1} \qquad\qquad (5.2b)$$

The incompressibility condition can also be rewritten as a condition for the constant volume of the cylindrical shell.

$$\pi(r^2 - a^2)l = \pi(R^2 - A^2)L \qquad\qquad (5.3a)$$

$$\lambda_a^2 \lambda_l - 1 = \frac{R^2}{A^2}(\lambda^2 \lambda_l - 1) = \frac{B^2}{A^2}(\lambda_b^2 \lambda_l - 1) \tag{5.3b}$$

In [94] , the equilibrium condition for a thick-walled cylindrical shell was given as Equation (5.4a), which was used to derivate an expression for P, Equation (5.4b), using Equation (5.2)-(5.3).

$$r\frac{d\sigma_{33}}{dr} + \sigma_{33} - \sigma_{11} = 0 \tag{5.4a}$$

$$P = \int_a^b \lambda \frac{\widehat{W}}{\delta\lambda}\frac{dr}{r} \equiv \int_{\lambda_a}^{\lambda_b} \frac{\frac{\widehat{W}}{\delta\lambda}d\lambda}{\lambda^2 \lambda_l - 1} \tag{5.4b}$$

For the modeling of fiber-reinforced thick-walled cylindrical actuators, the general approach of minimizing the system's potential energy under the geometric constraints of fiber inextensibility and incompressibility of the hyper elastic material were used instead of starting from the expression for differential equilibrium. The actuator was subject to internal inflation pressure P and an external force F acting along the axis of the cylinder at the closed end, as shown in Figure 5.5(c). This external force F, which is defined as the contact force between the actuator and heart tissue during cardiac ablation procedures, must be controlled. Let E be the total energy, $E1$ be the total strain energy, $E2$ be the total work done under pressure P, and $E3$ be the total work done by external force F. The corresponding expressions were derived and presented in Equation (5.5)

$$E1 = 2\pi l \int_a^b \widehat{W}r dr = 2V_0\lambda_l(1 - \lambda_a^2\lambda_l) \int_{\lambda_a}^{\lambda_b} \frac{\widehat{W}\lambda d\lambda}{(1 - \lambda^2\lambda_l)^2} \tag{5.5a}$$

$$E2 = -V_0 P(\lambda_a^2\lambda_l - 1) \qquad\qquad E3 = FL(\lambda_l - 1) \tag{5.5b}$$

$$E(\lambda_a, \lambda_b, \lambda_l) = E1 + E2 + E3 \qquad\qquad V_0 = \pi A^2 L \tag{5.5c}$$

This shows that the total energy was a function of three stretches, λ_a, λ_b, and λ_1. Equation (5.3b) gives a relationship between λ_a and λ_b. Thus $\widehat{E}(\lambda_a, \lambda_1) = 2V_0\lambda_1(1 - \lambda_a^2\lambda_1) \int_{\lambda_a}^{\lambda_b(\lambda_a)} \frac{\widehat{W}\lambda}{(1-\lambda^2\lambda_1)^2}d\lambda -$

$V_0 P(\lambda_a^2\lambda_1 - 1) + FL(\lambda_1 - 1)$. Without fiber-reinforcements λ_a and λ_1 are independent.

Differentiating $\hat{E}(\lambda_a, \lambda_1)$ with respect to λ_a, such that $\frac{\delta \hat{E}}{\delta \lambda_a} = 0$, then gives exactly the expression

for P, Equation (5.4b), as derived in [94]. Therefore, the expressions in Equation (5.4) do not hold

when fiber-reinforcements are considered and λ_a and λ_1 are no longer independent. In order to

complete the modeling for thick walled fiber-reinforced cylindrical actuators, a geometric

constraint arising from the inextensibility of the fibers was added. Let k be the lengths of the fiber,

and let α and $-\beta$ be the helix angles for the two fiber windings. Equation (5.6) represents the

inextensibility constraint formulated for thick walled cylindrical actuators with fibers wound

externally, and gives a relationship between λ_b and λ_1. For non-bending motion, angles α and

$-\beta$ must be equal [24].

$$\alpha = -\beta; \qquad k \cos \alpha = \lambda_l L; \qquad \lambda_b^2(k^2 - L^2) = k^2 - \lambda_l^2 L^2 \qquad (5.6)$$

Thus the expression for the total energy $\hat{\hat{E}}$ is only a function of λ_1 and was obtained in Equation

(5.7). Differentiating $\hat{\hat{E}}$ with respect to λ_1 and solving $\frac{\delta \hat{\hat{E}}}{\delta \lambda_1} = 0$ gives the desired relationship

between inlet pressure P, external contact force F, and the axial stretch λ_1 as a function of the

design, material parameters for the thick walled fiber-reinforced cylindrical actuators. The radial

stretches λ_1 and λ_b can then be obtained from the Equation (5.3b) and (5.6).

$$\hat{\hat{E}}(\lambda_l) = 2V_0\lambda_l[1 - \lambda_a^2(\lambda_l)\lambda_l] \int_{\lambda_a(\lambda_l)}^{\lambda_b(\lambda_l)} \frac{\hat{W}\lambda d\lambda}{(1-\lambda^2\lambda_l)^2} - V_0P[\lambda_a^2(\lambda_l)\lambda_l - 1] + FL[\lambda_l - 1] \qquad (5.7)$$

5.4 Experimental

In order to validate the actuation and force sensing requirements laid out in Sec 5.2.1 an

active setup was developed to actuate the passive deformable element. This section describes

design and development of the experimental setup which was then used for static and dynamic

characterization of the miniaturized actuation and sensing unit.
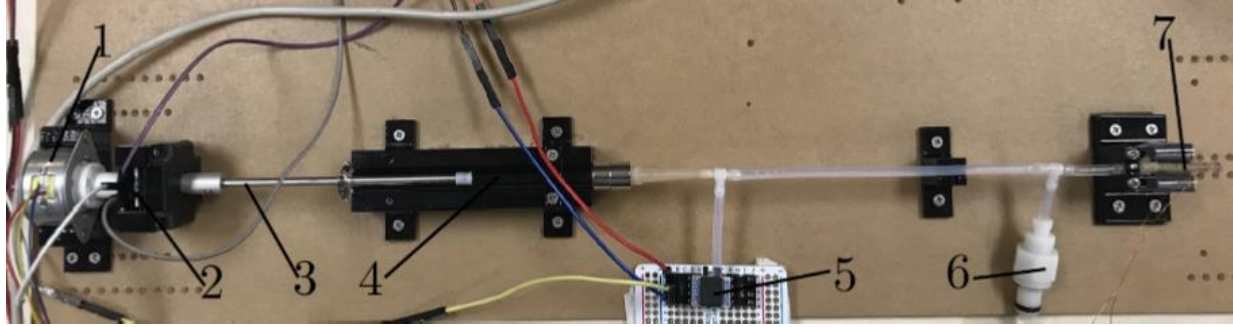
Figure 5.5: Experimental setup with active actuation and sensing components: (**1**) linear actuator, (**2**) force sensor, (**3**) glass syringe piston, (**4**) glass syringe cylinder, (**5**) pressure sensor, (**6**) shut-off valve, (**7**) miniaturized sensing and actuation unit.

5.4.1 Hydraulic Actuation

Figure 5.5 describes the active setup with actuation and sensing components. A glass syringe of internal diameter 3.26 mm (6500T55, McMaster) acted as a hydraulic cylinder, where the piston was attached to a DC linear motor (LP25-35, Nanotec) capable of applying up to 5 N. The piston was connected to the linear actuator with a force sensor (FSAGPDXX001RCAB5, Honeywell) in between, in order to measure the interaction force between them. A commercial pressure sensor (HSCDRRT100PGAA5, Honeywell), which can sense pressure from 0 to 0.6895 MPa was connected to the hydraulic circuit to measure the generated internal pressure due to actuation of the syringe. The shut-off two-way valve served the purpose of connecting and disconnecting the hydraulic circuit to another syringe, which was used to fill the hydraulic circuit with saline. Before filling the hydraulic circuit, the piston was removed completely from the syringe and then later re-inserted after the hydraulic circuit had been filled. All fixtures in the setup were fabricated using a 3D printer and a 2D laser-cutting machine.

5.4.2 Characterization Setup

Figure 5.6 shows the additional commercial sensors used for the characterization of the soft actuator and the sensor. A laser position sensor with a resolution of 0.005 mm (OADM 12I6430/S35A, Baumer) was used for measuring the displacement of the soft actuator under

various pressure inputs. During this procedure, there was no external force applied to the soft actuator. A force sensor with a resolution of 0.01N (FSG005WNPB, Honeywell) was used for soft sensor characterization, where the tip of the sensor was held fixed.


(a) **(b)**

Figure 5.6: Sensors for characterization of the miniaturized actuation and sensing unit: (**a**) (**1**) soft actuator, (**2**) red laser beam point, (**3**) laser displacement sensor; (**b**) (**1**) soft sensor, (**2**) leads out of the soft sensor, (**3**) commercial force sensor.

The soft sensor and the commercial force sensor (FSG005WNPB, Honeywell) required amplification boards (EMBSGB200, Tacuna systems) sensor outputs in a readable voltage range. The data from the force and displacement sensors in the experimental setup were sampled at 100 Hz and acquired on a microcontroller (Due, Arduino). Another microcontroller (Mega 2560, Arduino) was used solely for controlling the linear actuator in order to generate desired pressure input profiles used for the various tests performed in this study.

5.5 Results and Discussion

5.5.1 Static Characterization

For static characterization of the soft actuators, the setup in the Figure 5.6(a) was utilized. The linear actuator was run at a constant speed, producing ramp profiles for input pressure and corresponding output displacements of the soft actuators. A representative time-dependent input-output profile can be found in Figure 5.7. The final input pressure varies for each of the four

different actuator prototypes. However, for the same actuator prototype, the final input pressure and ramp profile were kept the same for different trials. The four different actuator prototypes, which varied in material and size, as shown in Figure 5.3, were tested with 10 data sets being collected for each actuator prototype. Figure 5.8 shows a single trial of the static calibration curve experiment for each of the four actuator prototypes. In addition a quadratic curve was fit to the 10 data sets for each prototype in order to be used in the dynamic characterization experiments.
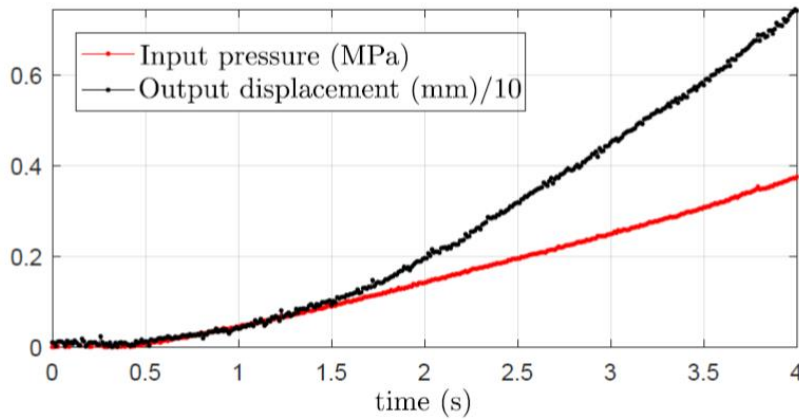

Figure 5.7: Pressure vs time input and displacement vs time output for the soft actuator static characterization.

The root mean square error (RMSE) for each of the four prototypes, Figures 5.8(a)-(d), were 0.1411 mm, 0.0929 mm, 0.0611 mm, and 0.1567 mm, respectively, while the coefficient of determination (R^2) were 0.9963, 0.9962, 0.9981 and 0.9909, respectively. The theoretical model closely approximated the performance seen in the experimental data for the Figures 5.8(c) and 5.8(d), but shows large variation when compared to experimental data found in Figures 5.8(a) 5.8(b). This indicates that the experimental modulus didn't match with the theoretical tensile modulus ($E_a = 0.614$ MPa).

As shown in Figures 5.8(a), an output displacement between 7-8 mm was achieved. For other actuator prototypes, Figures 5.8(b)-(d), the output displacement of the actuator was kept around 5 mm. However, same displacement range of 7-8 mm should be achievable for these actuators as well at higher applied input pressure levels. Hysteresis error for the soft actuators,

(E_a= 0.614 MPa & B = 1.3 mm) & (E_a = 1.173 MPa & B = 1.3 mm), was 14.92% and 9.62%,

respectively. A quadratic curve fit was applied to the forward loading and reverse loading curves

to calculate the hysteresis levels. The hysteresis was lowest at smaller maximum deformation

levels of the soft actuators.
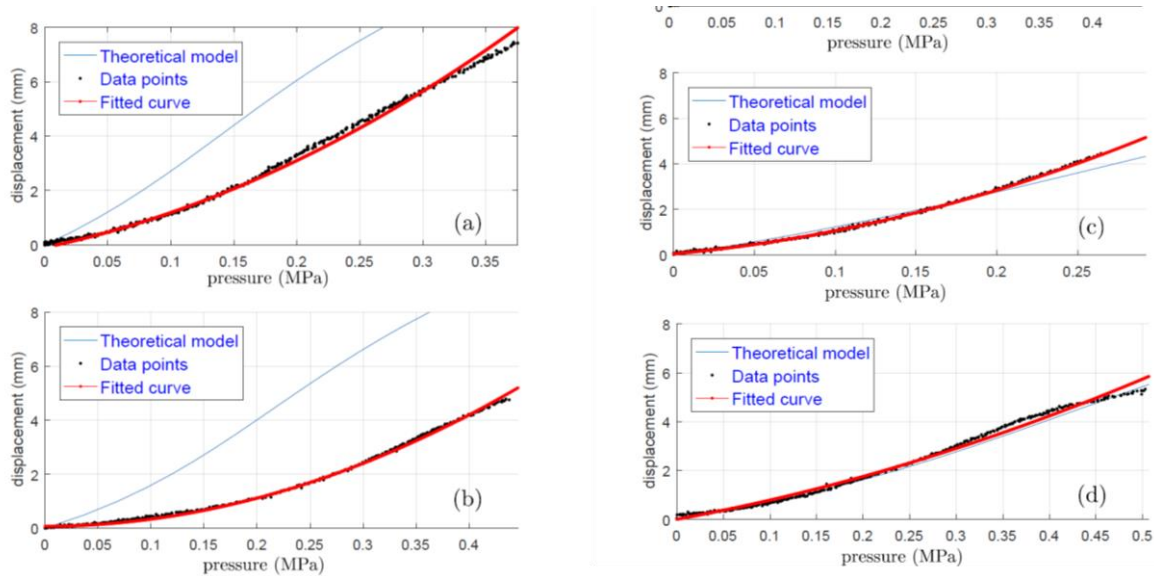
Figure 5.8: Static calibration curve for soft actuators: (**a**) E_a=0.614 MPa & B=1.3 mm, (**b**) E_a= 0.614 MPa & B=1.8 mm, (**c**) E_a=1.173 MPa & B=1.3 mm, (**d**) E_a= 1.173 MPa & B=1.8 mm.

For static characterization of the soft sensor, the setup in the Figure 5.6(b) was utilized.

The linear actuator was run at a constant speed producing ramp profiles for input pressure, as

shown in Figure 5.9. The commercial force sensor was used to measure the output force of the

soft actuator, and used to calibrate the voltage change induced on the soft embedded force sensor

as seen in Figure 5.10. The same experiment was repeated 10 times in order to collect extended
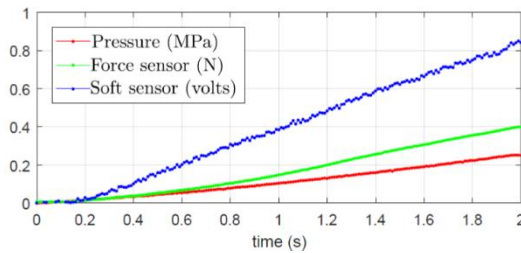
Figure 5.9: Pressure vs time input (red), corresponding actuator force output (green), and force as measured by soft sensor (blue).
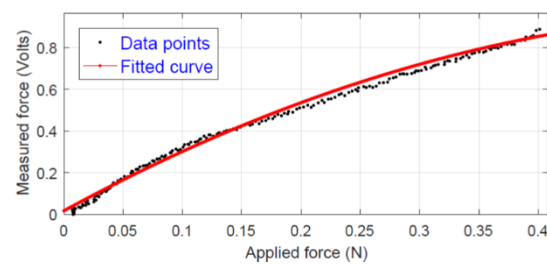
Figure 5.10: Soft sensor static calibration curve.

datasets. The soft miniaturized actuation and sensing unit was able to produce and sense a force output within the range of 0-0.4 N, as shown in Figure 5.9. Generation and sensing forces above 0.4 N are also possible if the applied pressure is increased beyond the ranges used in these experiments. In addition, constraint of the soft actuator (i.e. in a catheter sheath) will aid in transferring the forces generated linearly. Figure 5.10 shows the results of the calibration experiments. Again a quadratic curve was fit to the experimental data to be used in the execution of dynamic experiments. The RMSE and R^2 values for the fit were 0.0308 N and 0.9873, respectively. The hysteresis error for the soft sensor was 10.62%. A quadratic curve fit was applied to the forward loading and reverse loading curves to calculate the hysteresis. For determination of the resolution of the sensor, the datasets in Figure 5.10 were divided into samples of approximately 0-0.01 N with the initial value deducted. This input data set had a mean value of 0.0116 N with a standard deviation of $9.7218x10-04$ N. The corresponding output from the soft sensor had a mean value of 0.0256 V with a standard deviation of 0.0116 V.
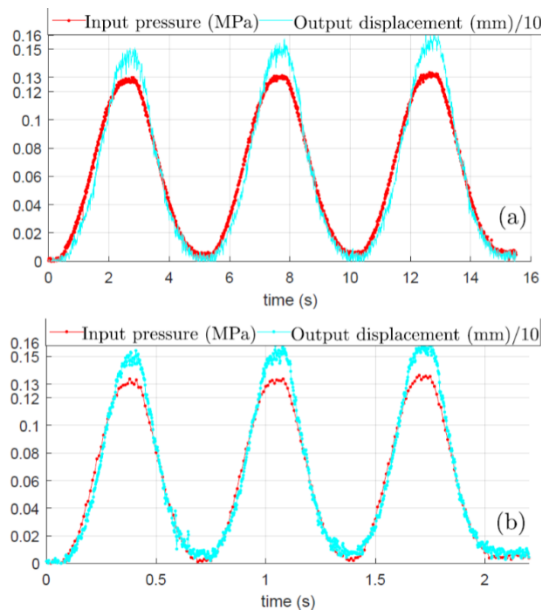
**Figure 5.11:** Soft actuator response to sinusoidal input for dynamic characterization: (**a**) at 0.2 Hz, (**b**) at 1.5 Hz.
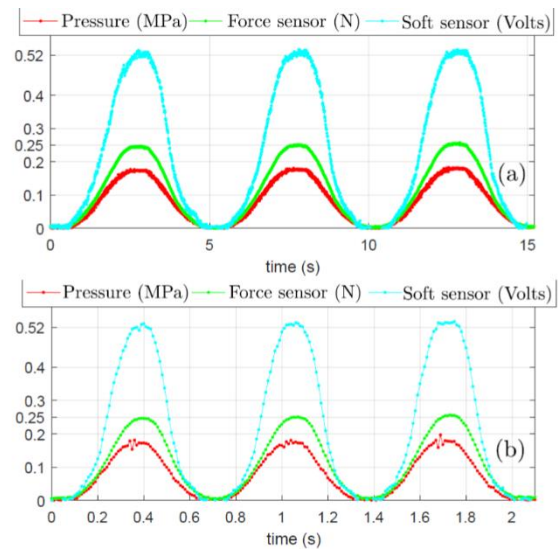
Figure 5.12: Soft sensor response to sinusoidal input for dynamic characterization: (**a**) at 0.2 Hz, (**b**) at 1.5 Hz.

5.5.2 Dynamic Characterization

A series of sinusoidal signals in the range of [0.2, 0.5, 1, 1.1, 1.2, 1.3, 1.4, and 1.5] Hz, were applied with, 0.2 Hz being established as the baseline, in order to determine if there was an appreciable decrease in the system response, both for soft sensor and soft actuator. For the soft actuator, it was important to have a system bandwidth in the range of 1-2 Hz for a displacement in the range of 1-2 mm, which corresponds to the dynamics of the heart wall. The soft actuator with E_a=0.614 MPa & B=1.3 mm was subjected to sinusoidal excitations to determine its bandwidth. Figure 5.11 shows the response to the baseline 0.2 Hz and maximum 1.5 Hz sinusoidal excitation. The peak operating pressure input was of approximately 0.13 MPa for each frequency input. The resulting system response was approximately 1.5 mm peak value for both 0.2 and 1.5 Hz indicating that the system response doesn't decrease at higher frequencies, and has at least a bandwidth of 1.5 Hz. Figure 5.13 shows the variation of the soft actuator response at different frequencies up to 1.5 Hz.
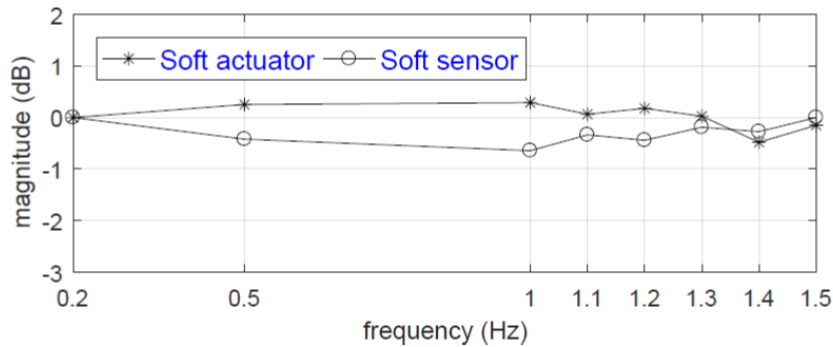
Figure 5.13: Magnitude vs frequency plot for the soft actuator and sensor for frequency range [0.2, 0.5, 1, 1.1, 1.2, 1.3, 1.4, and 1.5].

The soft sensor should have a bandwidth in the range of 1-2 Hz for a force range between 0.2-0.3 N, which is the range observed during cardiac ablation procedures. Figure 5.12 shows the response to the baseline 0.2 Hz and maximum 1.5 Hz sinusoidal excitation. The peak generated force output was about 0.25 N for each frequency input. The resulting system response was

approximately 0.52 V peak value for both 0.2 and 1.5 Hz indicating that the system response doesn't decrease at higher frequencies and has at least a bandwidth of 1.5 Hz. Figure 5.14 shows the variation of the soft sensor response at different frequencies up to 1.5 Hz.

5.6 Conclusion

In this study, a series of soft miniaturized actuation and sensing units varying in size and material, were designed, and met the challenging requirement specifications for cardiac ablation procedures with respect to compactness and integration. An experimental setup, using hydraulic actuation for safety, was specially developed for this application, used to characterize and control the prototyped units. Through experimental characterization, the soft miniaturized actuation and sensing units demonstrated the ability to meet the static and dynamic performance requirements for the cardiac ablation procedures. Furthermore, a hyperelastic theoretical model for fiber-reinforced thick-walled cylindrical actuators was developed, and can be used by researcher to conduct a predictive parametric design evaluation for the static and dynamic performance of a future prototype.

Even though these actuation and sensing units have been developed for the requirements of cardiac ablation procedures, a parametric design approach with different materials and sizes has been presented which can be tailored for other applications as well with requirement specification having similar orders of magnitude. Future work consists of developing force control strategies with these miniaturized units, and demonstrating their effectiveness under various user case scenarios and cadaver studies.

Acknowledgements

6 Conclusion

Pneumatic artificial muscles have the ability to act as useful alternatives to electromechanical actuators in the design of systems for human-centered applications. PAMs produce human scale forces and displacements when pressurized, and can be employed in a variety of applications due to their ability to produce a wide range of motions. However, these actuators are not without their challenges. Limitations in regards to their nonlinearity, which results in complicated fabrication processes, complex system design, and difficulty in developing accurate models for approximation and controllability must be addressed to improve their effectiveness in real world applications. We focused on designing a novel flat pneumatic artificial muscle capable of addressing the current challengers facing researchers employing PAMs in various applications. In particular, soft pneumatic and hydraulic actuation systems, both with and without microfluidic sensing, were developed to address existing limitations with soft actuators. The findings in this thesis have important implications for the development of pneumatic devices for human-centered applications.

6.1 Summary of Findings

A novel 2-Dimensional rectangular flat PAM was designed and manufactured through a simple layered fabrication technique which incorporated 3D printed molds. The fabrication process utilized a water-soluble mask to create a core section with a collapsed air chamber from a single cured polymer substrate as opposed to bonding two precured layers together. The introduction of the water-soluble mask eliminated the occurrence of unpredictable delamination failures, and provided a simple means of introducing a variety of air volume shapes through the ability to laser-cut desired shapes into the masks. The unique form factor, coupled with the water-

soluble mask, allowed for the design to be easily scaled and modified through alterations to the 3D printed mold designs. Furthermore, the introduction of laser-cut plastic sheets to serve as a geometric constraint during deformation, was pivotal in allowing for the creation of a bioinspired sensorized FPAM with embedded force and contraction sensing capabilities, as well as the creation of a fiber-reinforced bending actuator capable of fitting on the back of a human finger in antagonistic pairs. Subsequently, these design and fabrication techniques were employed and scaled down to develop a miniaturized hydraulic actuation and sensing unit to be used in cardiac ablation procedures.

Analytical hyperelastic deformation models were developed for the series of actuators developed. These theoretical models had not previously been presented for the developed actuators and required verification. Experimental apparatuses were developed to characterize the mechanical and electrical performance and of the various actuators, and compared favorably with the approximations made by the models. Furthermore, the feasibility of these design techniques to develop soft actuators capable of addressing real world applications was demonstrated through the development of the fiber-reinforced bending FPAM and the hydraulic fiber-reinforced thick-walled cylinder actuation and sensing unit employed in the functional catheter tip.

6.2 Implications

The results and ideas presented in this thesis have broad implications for the future development of pneumatic systems for use in human-centered applications.

Simple Fabrication

The introduction of water-soluble masks to form the collapsed air chambers, as well as the use of plastic sheets as geometric constraints during deformation, are powerful fabrication tools that provide researchers with significant control over their future designs. These materials not only

allow for the simple fabrication of FPAMs through a layered fabrication process using custom molds, but also provide versatility throughout the design process due to their ability to be cut into desired forms, shapes, or patterns. We expect that researchers will be able to quickly iterate through masks and plastic sheet designs, in order to optimize the performance of future FPAMs for their desired human centered applications.

Scalability

The designed actuators can be easily scaled up or down through the design of molds, shape of water-soluble masks and patterning of plastic sheets. The ability of these actuators to be fabricated into systems in both series (FPAM) and parallel (fiber-reinforced FPAM) have been demonstrated. In addition, the design techniques have shown the ability to incorporate embedded sensing at both external (sFPAM) and internal (functional catheter tip) human scales. We expect researchers to be able to further fine tune these techniques, and identify unique methods of scaling developed actuators to meet a variety of applications.

Improved Predictive Modeling

We expect the modeling techniques developed in this thesis to aid in the material selection process and provide future researchers and designers with the ability to optimize designs for their specific applications. Furthermore, we expect that this work will serve as a baseline for the development of additional techniques for the approximation of more complex deformation behaviors. Overall, the modeling techniques introduced, coupled with the developed fabrication process, should allow researchers to effectively analyze potential design configurations through computer simulations and quickly move into real world fabrication.

Open Areas

Although we have made significant strides in the development of soft actuators capable of being used in a variety of human-centered applications, there is still a lot left to be explored. Key questions include: What are the upper mechanical performance metrics of these soft actuators (i.e. fatigue life, robustness, etc.), and what are the limiting performance factors? How can we further translate what we learned through lab-based experimentation into real world applications? How can we automate the fabrication these soft systems to allow for rapid manufacture? Finally, how can employ the capabilities of these soft actuators to design integrated systems that are untethered to the lab, and able to improve the well-being of individuals? Continued exploration of solutions to these questions, will allow us to push the current boundaries PAM technologies and allow for the possible development of a multitude of devices aimed at improving the everyday livelihood of individuals.

7 References

[1] V. Y. Ma, L. Chan and K. J. Carruthers, "Incidence, Prevalence, Costs, and Impact on Disability of Common Conditions Requiring Rehabilitation in the United States: Stroke, Spinal Cord Injury, Traumatic Brain Injury, Multiple Sclerosis, Osteoarthritis, Rheumatoid Arthritis, Limb Loss, and Back Pa," *Archives of Physical Medicine and Rehabilitation,* vol. 95, no. 5, pp. 986-995, 2014.

[2] M. H. Fox, J. L. Rowland, K. Froehlich-Grobe, D. Vernberg, G. W. White and L. Haskett, "Determining Paralysis Prevalence In The United States," *Disability and Health Journal,* vol. 1, no. 3, pp. 172-179, 2008.

[3] B. Dellon and Y. Matsuoka, "Prosthetics, exoskeletons, and rehabilitation [Grand Challenges of Robotics]," *IEEE Robotics & Automation Magazine,* vol. 14, no. 1, pp. 30-34, 2007.

[4] D. Van Der Riet, R. Stopforth, G. Bright and O. Diegel, "An overview and comparison of upper limb prosthetics," in *IEEE AFRICON*, Pointe-Aux-Piments, Mauritius, 2013.

[5] M. D. Dickey, R. C. Chiechi, R. J. Larsen, E. A. Weiss, D. A. Weitz and G. M. Whitesides, "Eutectic Gallium-Indium (EGaIn): A Liquid Metal Alloy for the Formation of Stable Structures in Microchannels at Room Temperature," *Advanced Functinal Materials,* vol. 18, no. 7, pp. 1097-1104, 2008.

[6] R. C. Chiechi, E. A. Weiss, M. D. Dickey and G. M. Whitesides, "Eutectic Gallium–Indium (EGaIn): A Moldable Liquid Metal for Electrical Characterization of Self-Assembled Monolayers†," *Angewandte Chemie,* vol. 120, no. 1, pp. 148-150, 2007.

[7] K. Kure, T. Kanda, K. Suzumori and S. Wakimoto, "Flexible displacement sensor using injected conductive paste," *Sensors and Actuators A: Physical,* vol. 143, no. 2, pp. 272-278, 2008.

[8] Y. Bar-Cohen, Electroactive polymer (EAP) actuators as artificial muscles: reality, potential, and challenges, 2nd ed., Bellingham, Washington, USA: SPIE press Monograph, 2004.

[9] H. Wang and C. Li, "A Linear Dielectric EAP Actuator with Large Displacement Output," in *Measuring Technology and Mechatronics Automation*, Zhangjiajie, Hunan, China, 2009.

[10] A. T. Tung, B.-H. Park, A. Koolwal, B. Nelson, G. Niemeyer and D. Liang, "Design and Fabrication of Tubular Shape Memory Alloy Actuators for Active Catheters," in *IEEE/RAS-EMBS Biomedical Robotics and Biomechatronics*, Pisa, Italy , 2006.

[11] A. Villoslada, A. Flores-Caballero, D. Copaci, D. Blanco and L. Moreno, "High-Displacement fast-cooling flexible Shape Memory Alloy actuator: application to an anthropomorphic robotic hand," in *IEEE/RAS Humanoid Robots*, Madrid. Spain, 2014.

[12] C.-P. Chou and B. Hannaford, "Measurement and Modeling of McKibben Pneumatic Artificial Muscles," *Tansactions on Robotics and Automation,* vol. 12, no. 1, pp. 90-102, 1996.

[13] G. K. Klute, J. M. Czerniecki and B. Hannaford, "McKibben Artificial Muscles: Pneumatic Actuators with Biomechanical intelligence," in *IEEE/ASME Advanced Intelligent Mechatronics*, Atlanta, GA, 1999.

[14] F. Daerden and D. Lefeber, "Pneumatic Artificial Muscles: actuators for robotics and automation," *European Journal of Mechanical and Environmental Engineering,* vol. 47, pp. 10-21, 2002.

[15] Y.-L. Park, C. Majidi, R. Kramer, P. Bérard and R. J. Wood, "Hyperelastic pressure sensing with a liquid-embedded elastomer," *Journal of Micromechanics and Microengineering,* vol. 20, no. 12, pp. 1-6, 2010.

[16] Y.-L. Park, B.-R. Chen and R. J. Wood, "Design and Fabrication of Soft Artificial Skin Using Embedded Microchannels and Liquid Conductors," *IEEE Sensors Journal,* vol. 12, no. 8, pp. 2711-2718, 2012.

[17] Y. Mengüç, Y.-L. Park, H. Pei, D. Vogt, P. M. Aubin, E. Winchell, L. Fluke, L. Stirling, R. J. Wood and C. J. Walsh, "Wearable soft sensing suit for human gait measurement," *International Journal of Robotics Research,* vol. 33, no. 14, pp. 1748-1764, 2014.

[18] H.-S. Shin and Y.-L. Park, "Enhanced performance of microfluidic soft pressure sensors with embedded solid microspheres," *Journal of Micromechanics and Microengineering,* vol. 26, no. 2, pp. 1-9, 2016.

[19] J. Bishop-Moser and S. Kota, "Design and modeling of generalized fiber-reinforced pneumaitc soft actuators," *IEEE Transactions on Robotics,* vol. 31, no. 3, pp. 536-545, 2015.

[20] J. Bishop-Moser, G. Krishnan, C. Kim and S. Kota, "Design of soft robotic actuators using fluid-filled fiber-reinforced elastomeric enclosures in parallel combinations," in *IEEE/RSJ Intelligent Robots and Systems*, Vilamoura, Algarve, Portugal, 2012.

[21] P. Polygerinos, Z. Wang, J. T. B. Overvelde, K. C. Galloway, R. J. Wood, K. Bertoldi and C. J. Walsh, "Modeling of Soft Fiber-Reinforced Bending Actuators," *IEEE Transactions on Robotics,* vol. 31, no. 3, pp. 778-89, 2015.

[22] Y.-L. Park and R. J. Wood, "Smart pneumatic artificial muscle actuator with embedded microfluidic sensing," in *IEEE SENSORS*, Baltimore, MD, 2013.

[23] S. Wakimoto, K. Suzumori and T. Kanda, "Development of intelligent McKibben actuator," in *IEEE Intelligent Robots and Systems*, Edmonton, Alberta, Canada, 2005.

[24] W. Felt, K. Y. Chin and D. C. Remy, "Contraction Sensing With Smart Braid McKibben Muscles," *IEEE/ASME Transactions on Mechatronics,* vol. 21, no. 3, pp. 1201-1209, 2015.

[25] O. Erin, N. Pol and L. Valle, "Design of a bio-inspired pneumatic artificial muscle with self-contained sensing," in *IEEE Engineering in Medicine and Biology*, Orlando, FL, 2016.

[26] S. Wakimoto, K. Suzumori and T. Kanda, "Development of intelligent McKibben actuator with built-in soft conductive rubber sensor," in *IEEE TRANSDUCERS*, Seoul, Korea, 2005.

[27] F. Daerden and D. Lefeber, "The Concept and Design of Pleated Pneumatic Artificial Muscles," *International Journal of Mechanical and Environmental Engineering,* vol. 52, no. 3, pp. 41-50, 2001.

[28] H. In, B. B. Kang, M. Sin and K.-J. Cho, "Exo-Glove: A Wearable Robot for the Hand with a Soft Tendon Routing System," *IEEE Robotics & Automation Magazine,* vol. 22, no. 1, pp. 97-105, 2015.

[29] P. Polygerinos, Z. Wang, G. C. Kevin, R. J. Wood and C. J. Walsh, "Soft robotic glove for combined assistance and at-home rehabilitation," *Robotics and Autonomous Systems,* vol. 73, pp. 135-143, 2015.

[30] T. Nakamura and H. Shinohara, "Position and Force Control Based on Mathematical Models of Pneumatic Artificial Muscles Reinforced by Straight Glass Fibers," in *IEEE Robotics and Automation*, Roma, Italy, 2007.

[31] Y.-L. Park, J. Santos, K. G. Galloway, E. G. Goldfield and R. J. Wood, "A soft wearable robotic device for active knee motions using flat pneumatic artificial muscles," in *IEEE Robotics and Automation*, Hong Kong, China, 2014.

[32] S. Timoshenko and S. Woinowsky-Krieger, "Simply Supported Rectangular Plates under combined Action of Lateral Loads and of Forces in the Middle Plane of the Plate," in *Theory of Plates and Shells*, New York, McGraw-Hill, 1959, pp. 378-387.

[33] S. Timoshenko and S. Woinowsky-Krieger, "General Equations for Large Deflections of Plates," in *Theory of Plates and Shell*, New York, McGraw-Hill, 1959, pp. 416-420.

[34] T. T. Lee, Elastic-plastic analysis of simply supported rectangular plates under combined axial and lateral loading (Lehhigh University PhD Dissertation), Bethlehem, PA: Fritz Laboratory Reports, 1961.

[35] T. Mizuno, N. Tsujiuchi, T. Koizumi, Y. Nakamura and M. Sugiura, "Spring-damper model and articulation control of pneumatic artificial muscle actuators," in *IEEE Robotics and Biomimetics*, Karon Beach, Thailand, 2011.

[36] N. W. Barlett, M. T. Tolley, J. T. B. Overvelde, J. C. Weaver, B. Mosadegh, K. Bertoldi, G. M. Whitesides and R. J. Wood, "A 3D-printed, functionally graded soft robot powered by combustion," *Science,* vol. 349, no. 6244, pp. 161-165, 2015.

[37] R. F. Shepherd, A. A. Stokes, J. Freake, J. Barber, P. W. Snyder, A. D. Mazzeo, L. Cademartiri, S. A. Morin and G. M. Whitesides, "Using Explosions to Power a Soft Robot," *Angewandte Chemie International Edition,* vol. 52, no. 10, pp. 2892-2896, 2013.

[38] Y.-L. Park, B.-r. Chen, N. O. Pérez-Arancibia, D. Young, L. Stirling, R. J. Wood, E. C. Goldfield and R. Nagpal, "Design and control of a bio-inspired soft wearable robotic device for ankle–foot rehabilitation," *Bioinspiration & Biomimetics,* vol. 9, no. 1, 2014.

[39] F. C. Campbell, "Introduction to Composite Materials," in *Structural Composite Materials*, Materials Park, OH, ASM International, 2010, pp. 1-30.

[40] E. Sideridis, "The In-Plane Shear Modulus of Fibre Reinforced Composites as Defined by the Concept of Interphase," *Composites Science and Technoogy,* vol. 31, pp. 35-53, 1988.

[41] Y.-L. Park, B.-r. Chen, C. Majidi, R. J. Wood, R. Nagpal and E. Goldfield, "Active modular elastomer sleeve for soft wearable assistance robots," in *IEEE Intelligent Robots and Systems*, Vilamoura, Algarve, Portugal, 2012.

[42] G. Herrmann and C. Melhuish, "Towards Safety in Human Robot Interaction," *International Journal of Social Robotics,* vol. 2, no. 3, pp. 217-219, 2010.

[43] L. Brayda and R. Chellali, "Measuring Human-Robots Interactions," *International Journal of Social Robotics,* vol. 4, pp. 219-221, 2012.

[44] A. D. Santis, B. Siciliano, A. D. Luca and A. Bicchi, "An atlas of physical human–robot interaction," *Mechanism and Machine Theory,* vol. 43, pp. 253-270, 2008.

[45] T. B. Sheridan, "Human–Robot Interaction: Status and Challenges," *Human Factors,* vol. 58, pp. 525-532, 2016.

[46] M. Folgheraiter, M. Jordan, S. Straube, A. Seeland, S. K. Kim and E. A. Kirchner, "Measuring the Improvement of the Interaction Comfort of a Wearable Exoskeleton," *International Journal of Social Robotics,* vol. 4, pp. 285-302, 2012.

[47] D. Sasaki, T. Noritsugu, M. Takaiwa and H. Yamamoto, "Wearable Power Assist Device for Hand Grasping Using Pneumatic Artificial Rubber Muscle," in *IEEE International Workshop on Robot and Human Interactive Communication*, Kurashiki, Okayama, Japan, 2004.

[48] P. Polygerinos, S. Lyne, Z. Wang, L. F. Nicolini, B. Mosadegh, G. M. Whitesides and C. J. Walsh, "Towards a Soft Pneumatic Glove for Hand Rehabilitation," in *IEEE/RSJ Intelligent Robots and Systems*, Tokyo, Japan, 2013.

[49] E. N. Marieb and K. Hoehn, in *Human Anatomy & Physiology*, 8th ed., Pearson, 2010, pp. 484-490.

[50] E. N. Marieb and K. Hoehn, in *Human Anatomy & Physiology*, Pearson, 2010, pp. 514-521.

[51] J. Wirekoh and Y.-L. Park, "Design of flat pneumatic artificial muscles," *Smart Materials and Structures,* vol. 26, no. 3, pp. 1-10, 2017.

[52] B. K. MacDonald, O. C. Cockerell, J. W. A. S. Sander, S. Shorvon, S. D. Shorvon and S. D. Shorvon, "The incidence and lifetime prevalence of neurological disorders in a prospective community-based study in the UK," *Brain,* vol. 123, no. 4, pp. 665-676, 2000.

[53] E. D. Louis and J. J. Ferreira, "How common is the most common adult movement disorder? Update on the worldwide prevalence of essential tremor," *Movement Disorders,* vol. 25, no. 5, pp. 543-541, 2010.

[54] M. A. Thenganatt and E. D. Louis, "Distinguishing essential tremor from Parkinson's disease: bedside tests and laboratory evaluations," *Expert Review of Neurotherapeutics,* vol. 12, no. 6, pp. 687-696, 2012.

[55] J. Parkinson, "An essay on the shaking palsy," *The Journal of Neuropsychiatry and Clinical Neurosciences,* vol. 14, no. 2, pp. 223-236, 2002.

[56] J.-F. Daneault, B. Carignan and C. Duval, "Finger tremor can be voluntarily reduced during a tracking task," *Brain Research,* vol. 1370, pp. 164-174, 2011.

[57] R. J. Elble, "What is essential tremor?," *Current Neurology and Neuroscience Reports,* vol. 13, no. 6, pp. 353-360, 2013.

[58] I. Cathers, N. O'Dwyer and P. Neilson, "Entrainment to extinction of physiological tremor by spindle afferent input," *Experimental Brain Research,* vol. 171, no. 2, pp. 194-203, 2006.

[59] J. Rozman, A. Bartolić and S. Ribarič, "A new method for selective measurement of joint movement in hand tremor in Parkinson's disease patients," *Journal of Medical Engineering & Technology,* vol. 31, no. 4, pp. 305-311, 2007.

[60] R. J. Elble and G. Deuschl, "An update on essential tremor," *Current Neurology and Neuroscience Reports,* vol. 9, no. 4, pp. 273-277, 2009.

[61] E. D. Louis, "Essential tremor," *Lancet Neurology,* vol. 4, no. 2, pp. 100-110, 2005.

[62] J. Jankovic, K. S. Schwartz and W. Ondo, "Re-emergent tremor of Parkinson's disease," *Journal of Neurology Neurosurgery and Psychiatry,* vol. 67, no. 5, pp. 646-650, 1999.

[63] C. Riviere and N. Thakor, "Modeling and canceling tremor in human-machine interfaces," *IEEE Engineering in Medicine and Biology Magazine ,* vol. 15, no. 3, pp. 29-36, 1996.

[64] K. Madere, "Readi-Steadi Orthotic Glove System," Readi-Steadi, 2016. [Online]. Available: https://www.readi-steadi.com/. [Accessed March 2017].

[65] "GyroGear," GyroGear Ltd, 2016. [Online]. Available: http://gyrogear.co/gyroglove. [Accessed Mar 2017].

[66] J. Kotovsky and M. J. Rosen, "A wearable tremor-suppression orthosis," *Journal of Rehabilitation Research and Development,* vol. 35, no. 4, pp. 373-387, 1998.

[67] A. Trotman, "Microsoft," Microsoft, 2017. [Online]. Available: https://news.microsoft.com/en-gb/features/how-a-watch-helped-emma-write-again/. [Accessed March 2017].

[68] M. Manto, E. Rocon, J. Pons, J. M. Belda and S. Camut, "Evaluation of a wearable orthosis and an associated algorithm for tremor suppression," *Physiological Measurement,* vol. 28, no. 4, pp. 415-425, 2007.

[69] E. Rocon and J. L. Pons, "Wearable upper limb robots," in *Wearable Robots: Biomechatronic Exoskeletons*, John Wiley & Sons, Ltd), 2008, pp. 235-241.

[70] "LiftWare," 2014. [Online]. Available: https://www.liftware.com/. [Accessed Mar 2014].

[71] J. Wirekoh, L. Valle, N. Pol and Y.-L. Park, "Design of a biologically inspired sensorized flat pneumatic artificial muscle," *(unpublished).*

[72] E. Strickland, "Medical robots go soft," *IEEE Spectrum,* vol. 54, no. 4, pp. 11-12, 2017.

[73] M. Manti, A. Pratesi, E. Falotico, M. Cianchetti and C. Laschi, "Soft assistive robot for personal care of elderly people," in *IEEE Biomedical Engineering and Biomechatronics*, UTown, Singapore, 2016.

[74] H. K. Yap, J. H. Lim, F. Nasrallah, F.-Z. Low, J. C. H. Goh and R. C. H. Yeow, "MRC-glove: A fMRI compatible soft robotic glove for hand rehabilitation application," in *Rehabilitation Robotics*, Singapore, 2015.

[75] V. Oguntosin, W. S. Harwin, S. Kawamura, S. J. Nasuto and Y. Hayashi, "Development of a wearable assistive soft robotic device for elbow rehabilitation," in *Rehabilitation Robotics*, Singapore, 2015.

[76] R. F. Natividad and C.-H. Yeow, "Development of a soft robotic shoulder assistive device for shoulder abduction," in *Biomedical Robotics and Biomechatronics*, UTown, Singapore, 2016.

[77] S. Russo, T. Ranzani, J. Gafford, C. J. Walsh and R. J. Wood, "Soft pop-up mechanisms for micro surgical tools: Design and characterization of compliant millimeter-scale articulated structures," in *IEEE Robotics and Automation*, Stockholm, Sweden, 2016.

[78] T. Ranzani, M. Cianchetti, G. Gerboni, I. D. Falco and A. Menciassi, "A soft modular manipulator for minimally invasive surgery: design and characterization of a single module," *IEEE Transcations on Robotics,* vol. 32, no. 1, pp. 187-200, 2016.

[79] Q. Hao, Z. Li, H. Yan, G. Li and B. Su, "A natural orifice soft robot with novel driven method for minimally invasive surgery (MIS)," in *Asia-Pacific Conference on Intelligent Robot Systems*, Wuhan, China, 2017.

[80] S. Yim, G. Kartik and S. Metin, "Magnetically actuated soft capsule with the multimodal drug release function," *IEEE/ASME Transactions on Mechatronics,* vol. 18, no. 4, pp. 1413-1418, 2013.

[81] A. Pazouki, "Minimally invasive surgical sciences: a new scientific opportunity for all scientists," *Journal of Minimally Invasive Surgical Sciences,* vol. 1, no. 1, pp. 9-10, 2012.

[82] J. C. Hu, X. Gu, S. R. Lipsitz, M. J. Barry, A. V. D'Amico, A. C. Weinberg and L. N. Keating, "Comparative effectiveness of minimally invasive vs open radical prostatectomy," *Journal of the American Medical Association,* vol. 302, no. 14, pp. 1557-1564, 2009.

[83] A. Dooley and G. Asimakopoulos, "Does a minimally invasive approach result in better pulmonary function postoperatively when compared with median sternotomy for coronary artery bypass graft?," *Interactive Cardiovascular and Thoracic Surgery,* vol. 16, no. 6, pp. 880-885, 2013.

[84] K. Yoshida and K. Aonuma, "Catheter ablation of atrial fibrillation: Past, present, and future direction," *Journal of Arrhytmia,* vol. 28, no. 2, pp. 83-90, 2012.

[85] D. E. Haines, "Determinants of lesion size during radiofrequency catheter ablation: the role of electrode-tissue contact pressure and duration of energy delivery," *Journal of Cardiovascular Electrophysiology,* vol. 2, no. 6, pp. 509-515, 1991.

[86] D. C. Shah, G. Leo , N. Aeiby, P. Gentil-Baron, H. Burri and H. Sunthorn, "AB36-6 Evaluation of a new catherer sensor for real-time measurment of tissue contact," *Heart Rhythm,* vol. 3, no. 5, pp. S75-S76, 2006.

[87] K. Yokoyama, H. Nakagawa, D. C. Shah, H. Lambert, G. Leo, N. Aeby, A. Ikeda, J. V. Pitha, T. Sharma, R. Lazzara and W. M. Jackman, "Novel contact force sensor incorporated in irrigated radiofrequency ablation catheter predicts lesion size and incidence of steam pop and thrombus," *Circulation: Arrhythmia and Electrophysiology,* vol. 1, no. 5, pp. 354-362, 2008.

[88] R. Cappato, H. Calkins, S.-A. Chen, W. Davies, Y. Iesaka, J. Kalman, Y.-H. Kim, G. Klein, D. Packer and A. Skanes, "Worldwide survey on the methods, efficacy, and safety of catheter ablation for human atrial fibrillation," *Circulation,* vol. 111, no. 9, pp. 1100-1105, 2005.

[89] P. Polygerinos, L. D. Seneviratne, R. Razavi, T. Schaeffter and K. Althoefer, "Triaxial catheter-tip force sensor for MRI-guided cardiac procedures," *IEEE/ASME Transactions on Mechatronics,* vol. 18, no. 1, pp. 386-396, 2013.

[90] P. Puangmali, K. Althoefer, L. D. Seneviratne, D. Murphy and P. Dasgupta, "State-of-the-art in force and tactile sensing for minimally invasive surgery," *IEEE Sensors Journal,* vol. 8, no. 4, pp. 371-381, 2008.

[91] S. B. Kesner and R. D. Howe, "Force control of flexible catheter robots for beating heart surgery," in *IEEE Robotics and Automation*, Shanghai, China, 2011.

[92] D. Gelman, A. C. Skanes, M. A. Tavallaei and M. Drangova, "Design and evaluation of a catheter contact-force controller for cardiac ablation therapy," *IEEE Transactions on Biomedical Engineering,* vol. 63, no. 11, pp. 2301-2307, 2016.

[93] D. Haughton and R. Ogden, "Bifurcation of inflated circular cylinders of elastic material under axial loading—I. Membrane theory for thin-walled tubes," *Journal of the Mechanics and Physics of Solids,* vol. 27, no. 3, pp. 197-212, 1979.

[94] D. Haughton and R. Ogden, "Bifurcation of inflated circular cylinders of elastic material under axial loading—II. Exact theory for thick-walled tubes," *Journal of the Mechanics and Physics of Solids,* vol. 27, no. 5, pp. 489-512, 1979.

[95] Y. Zhu, X. Luo and R. W. Ogden, "Asymmetric bifurcations of thickwalled circular cylindrical elastic tubes under axial loading and external pressure," *International Journal of Solids and Structures,* vol. 45, no. 11, pp. 3410-3429, 2008.

[96] I. Edler and C. H. Hertz, "The use of ultrasonic reflectoscope for the continuous recording of the movements of heart walls. 1954," *Clinical Physiology and Functional Imaging,* vol. 24, no. 3, pp. 118-136, 2004.